Characterization and Optimization of RF power absorption in composite plasma

THESIS

submitted in partial fulfillment of the
requirements for the degree of

BACHELOR OF SCIENCE
in
PHYSICS

Author :	Berend Steentjes
Student ID :	1691325
Supervisor :	Felix Smits
Second corrector :	Wolfgang Löffler

Leiden, The Netherlands, July 8, 2021

Characterization and Optimization of RF power absorption in composite plasma

Berend Steentjes

Huygens-Kamerlingh Onnes Laboratory, Leiden University
P.O. Box 9500, 2300 RA Leiden, The Netherlands

July 8, 2021

Abstract

This paper addresses the optimization of RF power absorption into a Laser-Induced plasma, naturally consisting of some highly conductive plasma torus and a surrounding cloud of less conductive plasma. By reproducing experimentally determined values in simulations, a characterization of the two plasma-components is made. Using CCD-images, the dimensions of the plasma-components are determined, and an Ansatz is made for the electron density distribution and decay of the conductive component. Using 2.45 GHz power reflection- and 57 GHz voltage transmission measurement data, the dielectric properties of both plasma-components are determined by parametric sweeps in COMSOL^{TM}. Finally, the most accurate characterization of the LI-plasma is implemented in simulations on magnetic induction heating within a TE-102 rectangular and a TE-011 cylindrical cavity, and the resulting power absorption ratios are compared to that of capacitive heating in a TE-101 rectangular cavity.

Contents

1 Theory **7**
- 1.1 Resonant cavity matching 7
  - 1.1.1 Transmission lines 7
  - 1.1.2 Circuit theory 11
  - 1.1.3 Matching 13
- 1.2 Cavity perturbation theory 20
  - 1.2.1 Frequency shift and quality factor from sample below cutoff 21
  - 1.2.2 Frequency shift from insertion of dielectrics 24
  - 1.2.3 Frequency tuning for cavity with dielectric slabs 25
  - 1.2.4 Frequency shift from sample beyond cutoff 27
- 1.3 Drude model 28
- 1.4 Electromagnetic power absorption 31
  - 1.4.1 Electric power absorption: capacitive heating 32
  - 1.4.2 Magnetic power absorption: inductive heating 35
  - 1.4.3 CPT-effects from absorbing plasma 39
- 1.5 Thermodynamics 43
  - 1.5.1 Boltzmann-normalized Saha equation 43
  - 1.5.2 Heat conduction power loss of the plasma 45

2 Experimental setup and measurements on setup **47**
- 2.1 System overview 47
- 2.2 Measurements on plasma 50
- 2.3 Simulation models of measurement setups 53
  - 2.3.1 Introduction to Comsol's RF-module 53
  - 2.3.2 Simulation model of empty TE-101 cavity 57
- 2.4 Preliminary simulations on torus-shape in TE-101 cavity 60
- 2.5 Transmission line calculations on empty TE-101 cavity 62

3 CCD image interpretation **65**
3.1 LP-geometry: major and minor radius 67
3.1.1 Determination of major radius $r(t)$ 67
3.1.2 Determination of minor radius $a(t)$ 69
3.1.3 Determination of luminous volume $V(t)$, area $A(t)$, and decay length $R(t)$ 71
3.2 Dynamic electron density $\eta(t)$, power loss $P_l(t)$, and temperature $T(t)$ 74
3.3 LP radial electron density distribution $\eta(\rho)$ 77
3.4 EC-geometry 81
3.5 Total intensity of LP and EC under RF-heating 87

4 Characterization of capacitive plasma heating **89**
4.1 Characterization of the homogeneous composite plasma 90
4.1.1 Characterization of the LP 90
4.1.2 Characterization of the EC 92
4.1.3 Dynamic characterization of homogeneous plasma 94
4.2 Characterization of the non-homogeneous composite plasma 97
4.2.1 Ansatz- and data comparison for 2.45 GHz 98
4.2.2 Ansatz- and data comparison for 57 GHz 100
4.2.3 Hybrid model- and data-comparison for 2.45 GHz 101
4.3 Characterization of capacitive power absorption efficiency 104
4.3.1 Simulated capacitive power absorption ratio 105

5 Characterization of inductive plasma heating **109**
5.1 Characterization of inductive power absorption 109
5.1.1 Induced current density 111
5.1.2 Power absorption ratio 114
5.2 Characterization of rectangular TE-102 cavity 116
5.2.1 Tuning-relation $(w,d)|\delta$ for the rectangular TE-102 cavity containing FQ slabs 116
5.2.2 Properties of the TE-102 cavity setup 119
5.3 Characterization of inductive power absorption efficiency 120
5.3.1 Simulated inductive power absorption ratio 120
5.3.2 Plasma power loss at stability under inductive heating 123
5.4 Characterization of cylindrical TE-011 cavity 124

6 Discussion of results **129**

7 Conclusions **133**

8 Appendices **141**

Introduction

Motivation for area of research

In its aim to decelerate climate change and the possible future depletion of raw materials, the world is already starting to switch to sources of renewable energy in order to limit the emission of carbon dioxide. During periods of low demand (such as nighttime), the excess energy needs to be invested immediately. A popular investment is conversion of the electrical energy to molecular energy. One example is the current production of hydrogen gas in offshore windmill parks, where hydrogen and oxygen gas are produced from water by electrolysis. Another example, which is the process that this paper aims to employ, is the dissociation of waste gases by microwave heating. In general, the central premise of these processes is a reverse exothermic reaction, in which a molecule is dissociated into components by investment of energy required for its dissociation. The energy invested in dissociation of the molecule can be released upon combustion of the components into the original molecule ($H_2 + \frac{1}{2}O_2$), or be used to catalyze reactions (O_2) and synthesize fuel (CO). As for carbon dioxide CO_2, its dissociation can happen along two possible reactions, consecutively resulting in a net dissociation reaction:

$$1\ CO_2 + \Delta H \rightarrow 1\ CO + \frac{1}{2}\ O_2, \quad \Delta H = 2.9\ \text{eV}$$

The decomposition of waste gases relies on adding energy to the waste gas molecules in order to dissociate them. Conventionally, this energy is added by excitation with magnetron radiation in a microwave cavity containing the gas. The gas molecules can only absorb the radiation if they contain charges or dipoles that respond to the RF-field (RF: radio frequency). In domestic purposes, microwave heating relies on a sample's high water content: the molecular dipoles oscillate along with the electric

Version of July 8, 2021– Created July 8, 2021 - 13:14

field, where their vibration is equivalent to a rise in temperature. In dissociation purposes of CO_2, heating relies on increasing the susceptibility to the RF-radiation by creating charges through ionization. The process of ionization, where electrons gain enough energy to leave the corresponding ions, turns a charge-less molecule into a positive- (ion) and negative (electron) charge. This gas is susceptible to the electric field, because the ions and electrons are displaced, and no longer shield each other. If the gas is ionized beyond some significant degree (along with other properties), it is classified as a plasma. Because the temperature of a CO_2-plasma falls within the regime of dissociation, sustaining it through microwave heating leads to dissociation. This method is called *plasmolysis*.

Established research on plasmolysis

Established research on plasmolysis revolves around injecting pure CO_2-gas into a microwave cavity sustaining a plasma, and extracting the gas. The best research group to mention here is DIFFER [1]. Their setup employs a 2.45 GHz magnetron matched to a shorted WR-340 cavity by an automatic matching circuit half a guide wavelength from the short, forming a TE-101 mode. A fused quartz (FQ) tube runs down the center of the TE-101 cavity, axisymmetric with the electric field. The plasma is created and maintained by the oscillating electric field at the tube. On one end of the tube, CO_2-gas is injected with a volumetric flow rate of roughly $\dot{V} \approx 10$ [slm], and the cavity is excited with an input power of roughly $P_{in} \approx 1$ [kW]. On the other end of the tube, the (imperfect) reactor product gas-mixture is extracted. From spectrometry measurements on the extracted gas, the fractional conversion α could be determined by the amount of dissociated CO_2 molecules upon injection of some amount of injected CO_2 molecules. In terms molecular flow rate of CO_2-molecules in the injected gas $\dot{N}_{in}$ and for molecular flow rate of CO_2-molecules in extracted gas $\dot{N}_{out}$, the fractional conversion α equals:

$$\alpha \equiv 1 - \frac{\dot{N}_{out}(CO_2)}{\dot{N}_{in}(CO_2)}$$

Assuming RF-energy to be distributed equally to each molecule within the reactor and approximating the two-step dissociation process as singular-stepped, all CO_2-molecules will dissociate if the energy per molecule (SEI) equals the net dissociation reaction enthalpy ΔH; in which case $\alpha(SEI \geq \Delta H) = 1$ and $\alpha(SEI < \Delta H) = 0$. Under energy homogeneity, the specific energy input (per molecule) - SEI - is simply the input RF-energy absorbed

Version of July 8, 2021– Created July 8, 2021 - 13:14

by molecules ($U_{in} \cdot \eta_{RF}$) divided by the amount of absorbing molecules (N), where η_{RF} is the RF-efficiency accounting for parasitic losses of RF-power such as power loss to the cavity walls. Dividing the terms in both the numerator and the denominator by time, $SEI = P_{in} \cdot \eta_{RF}/\dot{N} \approx P_{in} \cdot \eta_{RF}/(\dot{V} \cdot n_0)$, with P_{in} the RF input power, ($\dot{N}$) the (injected) CO_2-molecular flow rate, and $n_0 \approx 3 \cdot 10^{25}$ [m^{-3}] the Loschmidt constant. We may obtain the total reactor energy efficiency η_{tot} in equation (1), representing the ratio of energy invested in dissociation over the total invested energy.

$$\eta_{tot} = \alpha \frac{\Delta H}{SEI} = \alpha \cdot \Delta H \frac{P_{in}}{\dot{V} \cdot n} \cdot \eta_{RF} \tag{1}$$

In reality, the molecular energy distribution is unequal: intrinsically due to Maxwell-Boltzmann statistics, and extrinsically due to non-homogeneous field strength as well as "gas-slippage" (injected gas slipping past the hot plasma). This makes the fractional conversion α a function to be experimentally determined from parameters applied to the reactor setup; the volumetric injection flow rate ($\dot{V}$) and input power (P_{in}).

Our ultimate aim is to achieve full reactor efficiency $\eta_{tot} = 1$. Experimentally, this can be approached by ensuring $SEI = \Delta H$ corresponding to a variation of the setup-parameters near the values $P_{in} = 3$ [kW] and $\dot{V}_{in} = 10$ [slm]. If $SEI < \Delta H$, then $\alpha < 1$ because (some) molecules do not attain the energy required for dissociation. If $SEI \geq \Delta H$, then even if $\alpha = 1$, $\eta_{tot} < 1$ because we have invested more energy per CO_2-molecule than should have been required for CO_2-dissociation. There is an endemic trade-off between conversion α and η_{tot}; increasing one decreases the other.

Moreover, we aim to achieve a full conversion rate $\alpha = 1$, because the extraction of pure CO_2 gas has cost energy investment. In order to ensure that all injected molecules have undergone dissociation, we want all injected molecules to pass through the plasma and remain within the plasma for a significant residence time. The term "gas-slippage" refers to injected gas that does not pass through the plasma, and this issue is what the introduction of a pre-formed laser-induced plasma intends to resolve.

Research description

This project provides a setup before the microwave heating of the cavity by creating a plasma within the cavity, shortly after which the RF heating is applied. A plasma is created by a 16 nanosecond-pulse of a 20 MegaWatt-power laser beam focused at the center of the cavity by a 50 millimetre-lens. The laser radiation is absorbed by the gas molecules at the focus,

leading to a rise in temperature and subsequent ionization. The plasma thus created at the focus undergoes a geometric evolution from the focal point's double cone shape; by thermal expansion and subsequent collapse, a vortex ring is formed beyond 20 [us], which has the topology of a torus. The vortex ring has a high degree of ionization, classifying as a plasma. Following similar research, the plasma's response to RF-heating has been studied when the plasma is placed at the location of the cavity with the highest electric field amplitude.

The microwave cavity contains a TE-101 mode, and it is placed inside a vacuum chamber filled with helium-gas (rather than the CO_2-gas to be ultimately used in applications). The choice for helium is motivated by the aim to study the RF-properties of the LI-plasma proper; the chemical inertness of this noble gas ensures that absorbed power is converted only to the sustenance of the plasma through ionization and heating. No gas is injected or extracted. All research is focused on the RF-efficiency η_{RF}, which is the ratio of power absorbed in the toroidal laser-induced plasma P_a over the input power P_{in}.

Goals

The response of the LI-plasma to the 2.45 [GHz] magnetron frequency was studied during the first 100 microseconds after the laser-pulse and in two forms: power reflection measurements near 2.45 [GHz] for $P_{in} = 1$ [mW], and CCD-images of the LI-plasma's radiant intensity with or without magnetron heating at $P_{in} = 3$ [kW]. These preliminary experiments indicated that capacitive heating of a LI-plasma were unsuccessful in sustaining it, with both measurements providing evidence that RF-power is absorbed in a cloud around the toroidal vortex ring instead of the torus itself.

By comparing CCD-images of the LI-plasma with and without magnetron heating, the (relative) excess plasma radiant intensity indicates localized power absorption. The first excess radiant intensity appears beyond $t = 30$ [us] after the laser pulse, and is situated exclusively within a cloud, 1 [mm] around the toroidal plasma. Excess radiant intensity within the toroidal plasma itself is identified only beyond a "cutoff time" $t_c \approx 50$ [us], in which case the toroidal plasma would have decayed well below its initial ionization grade.

Frequency-swept mW-power-reflection measurements on the plasma-filled cavity provided the dynamic development of the resonance frequency shift Δf and the quality factor Q. With respect to the empty cavity ($Q_\emptyset$, $f_\emptyset \sim \Delta f = 0$), a reduced quality factor indicates the presence of an absorbing

Version of July 8, 2021– Created July 8, 2021 - 13:14

sample, and a high (negative) frequency shift indicates the presence of a beyond-cutoff sample. Around the cutoff time $t_c = 50$ [us], the previously-stable frequency shift $\Delta f \approx -6$ [MHz] decreases to zero within the next 20 microseconds. Simultaneously, the previously-increasing quality factor decreases during the next 20 microseconds after cutoff time, after which it steadily increases again to the empty cavity quality factor. This provides additional evidence for a composite plasma, with one component absorbing all RF-radiation up to t_c, and with the other component remaining beyond cutoff up to t_c.

Our hypothesis is that **during the laser pulse, the heavy ions remain in place around close to the focal point of the laser beam, while the electrons are scattered around this focus due to their lower mass, resulting in respectively in a dense and a diffuse component.** The dense, toroidal component is coined the *Laser-Plasma* (LP), consisting of ions and slightly fewer electrons. The diffuse component is coined the *Electron-Cloud* (EC), consisting of electrons scattered from the laser focus.

Since we only want to supply energy to the dissociation reactions of the ions inside the LP, the energy absorbed by the EC or cavity walls is regarded as lost, and lastly any magnetron energy leaked by the cavity is lost as well; $\eta_{RF} \equiv \frac{P_a(LP)}{P_{in}}$. The focus in this project will be entirely on maximizing the power absorption into the LP with respect to the EC or the cavity walls. Our main research question in this Bachelor Research Project being: **"How do we maximize the RF-power absorption into the Laser-Plasma, and minimize the power absorption into Electron-Cloud and cavity?"**

General plan of attack

A full characterization of the plasma is made by a dynamic formulation of the dielectric- and geometric properties of the two components separately. The plasma geometry and its decay constant will be derived from CCD images. The plasma dielectric properties will be derived by a parametric sweep of the electron density (and to a lesser degree the temperature) within simulations of the measurement setup. A characterization is concluded accurate if the $|S_{11}|^2$ and $|S_{21}|$ analysis on the 2.45 GHz resp. 57 GHz simulation setups with the same plasma reproduces both measurements. The plasma with such properties is then subjected to heating under magnetic induction, and the RF-efficiency under this new system is compared to the efficiency under the old capacitive heating system.

Chapter 1

Theory

1.1 Resonant cavity matching

The goal of this section is to describe how the EM-waves radiated by the magnetron are channeled through a waveguide, and thereafter completely contained by the cavity. This will therefore require a description of a cavity resonator. A cavity resonator can be built in three steps: the waveguide, a short at the waveguide's end, and finally an iris - at some distance from this short - forming a matched cavity. Analogously with this order, we will cover the modes in a guide, along with the associated solutions for equivalent voltage and current. Then we will combine these solutions to come with a formula for the impedance, leading to an equivalent circuit description. Finally, we will cover the matching and tuning of this circuit through the equivalent circuit theory equations for a series circuit.

1.1.1 Transmission lines

We will begin transmission line theory from the structure of the modes propagating through it. Transmission line theory describes the transmission of EM-waves along a waveguide. From the boundary conditions of the E- and B-field for conductors, one can deduce the distribution of the field within this guide. Whereas unrestricted EM waves originating from a point source would emanate into all directions of $3D$ space attenuating quadratically with the distance from the source, placing the source within a waveguide constricts the waves to radiate along the $1D$ depth of the waveguide, conserving all EM-energy within it. A waveguide is a hollow conductive pipe that is of constant shape along its depth, the wave propagation direction $+\hat{\mathbf{z}}$. This periodicity of the waves in the z-direction can be

represented as $\mathbf{E}(x,y,z) = \mathbf{E}(x,y) \cdot e^{-i\beta z}, \mathbf{H}(x,y,z) = \mathbf{H}(x,y) \cdot e^{-i\beta z}$. The waves must satisfy the curl equations $\nabla \times \mathbf{E} = -i\omega\mu_0\mathbf{H}$ and $\nabla \times \mathbf{H} = i\omega\epsilon_0\mathbf{E}$. This gives for the curl of the Electric field:

$$\partial_y E_z + i\beta E_y = -i\omega\mu_0 H_x \tag{1.1a}$$

$$\partial_x E_z + i\beta E_x = i\omega\mu_0 H_y \tag{1.1b}$$

$$\partial_x E_y - \partial_y E_x = -i\omega\mu_0 H_z \tag{1.1c}$$

and for the curl of the Magnetic field:

$$\partial_y H_z + i\beta H_y = i\omega\epsilon_0 E_x \tag{1.2a}$$

$$\partial_x H_z + i\beta H_x = -i\omega\epsilon_0 E_y \tag{1.2b}$$

$$\partial_x H_y - \partial_y H_x = i\omega\epsilon_0 E_z \tag{1.2c}$$

Additionally, from Maxwell's equations, we should get:

$$\partial_x H_x + \partial_y H_y = i\beta H_z \tag{1.3a}$$

$$\partial_x E_x + \partial_y E_y = i\beta E_z \tag{1.3b}$$

And lastly, we will need the boundary conditions of the electric and magnetic field:

$$E_{\parallel} = 0 \tag{1.4a}$$

$$H_{\perp} = 0 \tag{1.4b}$$

We will merely be considering the case of a rectangular waveguide, with a and b the lengths in the x- and y-direction respectively. The requirements on the propagation of the EM-wave naturally leads to formulae describing the wave.

Suppose that the waveguide is irradiated at one end by EM-waves with the electric field polarized in the y-direction. An electric plane wave propagating in the $+z$-direction alone cannot propagate through the waveguide, because the wave has no restriction such that $E_y(x = 0) = E_y(x = a) = 0$ in order to satisfy equation (1.4)a. However, this restriction can be implemented when considering two plane waves superimposed, with:

$$\mathbf{E}_1 = E_0 e^{ik_x x} e^{ik_z z} \hat{y}$$

$$\mathbf{E}_2 = -E_0 e^{-ik_x x} e^{ik_z z} \hat{y}$$

The superposition of these plane waves equals

$$\mathbf{E}_{tot} = \mathbf{E}_1 + \mathbf{E}_2 = 2iE_0 \sin(k_x x) e^{ik_z z} \hat{y}$$

Version of July 8, 2021– Created July 8, 2021 - 13:14

Such a superimposed wave is called a mode of the waveguide. The mode that will propagate through our waveguide is represented as being a TE_{10} mode. For the general TE_{mnl} form, the subscript $s \in \{m, n, l\}$ indicates a corresponding periodicity of $s \cdot \frac{\lambda_s}{2}$. Therefore, the TE_{10} mode E-field distribution follows a period π over $\hat{\mathbf{x}}$ and is homogeneous over $\hat{\mathbf{y}}$. In order to satisfy (1.4), we must have $\mathbf{E}_{tot}(x = 0) = \mathbf{E}_{tot}(x = a) = 0$. Combined with the minimal periodicity $m = 1$, we therefore need $k_x = \frac{2\pi}{\lambda_x} = \frac{\pi}{a}$. This relation, combined with $k_x^2 + k_z^2 = k_0^2$ and $k_z = \beta$, we obtain:

$$\lambda_g = \frac{2\pi}{\beta} = \left(\frac{1}{\lambda_0^2} - \frac{1}{\lambda_c^2}\right)^{-\frac{1}{2}} \text{ [m]} \tag{1.5a}$$

$$\lambda_c = 2 \cdot a \text{ [m]} \tag{1.5b}$$

$$\lambda_0 = \frac{c}{f_0} \text{ [m]} \tag{1.5c}$$

Here c is denotes the light speed constant $c \approx 3 \cdot 10^8$ [m/s], and the third geometric parameter of the waveguide is its depth d which conventionally means the distance from the waveguide's short. Combining the equations in (1.5), we can derive the resonant frequency for a "boxed" cavity with dimension $a \times b \times d$ sustaining a TE_{mnl} mode:

$$f_0 = \frac{c}{2}\sqrt{\left(\frac{m}{a}\right)^2 + \left(\frac{n}{b}\right)^2 + \left(\frac{l}{d}\right)^2} \text{ [Hz]} \tag{1.6}$$

The first expression, λ_g, is called the guide wavelength. It is the length along the z-direction for which the travelling TE-mode wave has completed one period. The second expression, λ_c, is the cutoff wavelength and for a TE_{1nl} mode, this is equal to twice the waveguide width. Lastly, λ_0 is the free space wavelength of the signal.

The propagation of the waves along the waveguide can be described by a periodicity and an attenuation. The waves are able to propagate because of currents induced along the walls of the waveguide, in order to cancel the field where required by (1.4). Since the waveguide is constructed from a lossy conductor, we also need to account for these losses in the amplitude of the propagating fields. The periodicity along $\hat{\mathbf{z}}$ is given by the wavevector β. The loss of amplitude along this depth of the waveguide is given by the attenuation constant α, computed for the TE_{10} mode in [2, (14a)]. They are encapsulated under a complex propagation constant γ:

$$\gamma = \alpha + i\beta \text{ [m}^{-1}\text{]} \tag{1.7a}$$

$$\alpha = \sqrt{\frac{\epsilon_0 \omega}{2\sigma}} \frac{1 + (2b/a)(\lambda_0/(2a))^2}{b\sqrt{1 - (\lambda_0/(2a))^2}} \ [\mathrm{m}^{-1}] \tag{1.7b}$$

$$\beta = \frac{2\pi}{\lambda_g} \ [\mathrm{m}^{-1}] \tag{1.7c}$$

We have established that the individual Electric waves forming the TE_{10} mode propagate in the x- and z-direction, and are polarized in the y-direction. Therefore,

$$E_x = 0, E_y \neq 0, E_z = 0$$

Using, (1.1) a to c, we get:

$$H_x \neq 0, H_y = 0, H_z \neq 0$$

From (1.2) a and c, and (1.3) b, we get:

$$\partial_y H_x = 0, \partial_y E_y = 0, \partial_y H_z = 0$$

We can now deduce the expressions for H_x and H_z from the expression for E_y with (1.1) a and c, and write the coefficients in terms of $Z_h = \frac{\omega\mu_0}{\beta}$, $k_c = \frac{\pi}{a}$, and arbitrary amplitude A to deduce (1.8).

$$H_z(x,z) = A\cos(k_c x)e^{\gamma z} \tag{1.8a}$$

$$H_x(x,z) = \frac{i\beta}{k_c} A\sin(k_c x)e^{\gamma z} \tag{1.8b}$$

$$E_y(x,z) = -iAZ_h \frac{\beta}{k_c}\sin(k_c x)e^{\gamma z} \tag{1.8c}$$

When a waveguide is terminated at a conductive plane covering the waveguide's cross-section at depth $z = 0$ within the waveguide, a short-circuit is formed at this plane. The incident TE_{mn} travelling wave of the waveguide (1.8) is reflected at the short, and the superposition of the incident $(+)$ and reflected $(-)$ travelling wave results in a TE_{mnl} standing wave. The shorted waveguide corresponds to a closed circuit in which equivalent voltage and current are proportional to the transverse electric field resp. -magnetic field, as per [2, equation (10)]; with voltage- and current phase shift equal to $\phi_V = \pi$ resp $\phi_I = 0$ upon reflection at the short by [3]. Consequent expressions for the total voltage and current are provided in (1.9), and are the superposition of the incident- ($\propto \exp(+\gamma z)$) and reflected ($\propto \exp(-\gamma z + \phi)$) travelling waves. The expressions (1.9) result in zero-valued E-field at the short $E(z=0) \propto V(z=0) \propto \sinh(z=0) = 0$,

Version of July 8, 2021– Created July 8, 2021 - 13:14

satisfying boundary condition (1.4a). Moreover, ignoring losses such that $\gamma z = i\beta z$, the B-field is evidently $\pi/2$ out of phase with the E-field by $B(z) \propto \cosh(i\beta z) = \cos(\beta z) = \sin(\beta z + \pi/2) \propto E(\beta z + \pi/2)$.

$$V = V^+ + V^- = V_0 e^{\gamma z} + V_0 e^{-\gamma z + \pi} = V_0 \cdot \sinh \gamma z \tag{1.9a}$$

$$I = I^+ + I^- = I_0 e^{\gamma z} + I_0 e^{-\gamma z + 0} = I_0 \cdot \cosh \gamma z \tag{1.9b}$$

1.1.2 Circuit theory

Shorted waveguide

Now that we have found solutions for the equivalent voltage and current, we can combine these under Ohm's law to get the impedance associated with some depth of waveguide from the short. The impedance can then be used to construct the corresponding equivalent RLC-circuit. A shorted waveguide can be seen as a one port network. The impedance $Z_{11} = Z$ associated with a shorted waveguide can be determined with Ohm's law: $Z = V/I$, with V and I the total voltage resp. current, which are the superposition of incident and reflected. From (1.9):

$$Z = \frac{V^+ + V^-}{I^+ + I^-} = \frac{V_0}{I_0} \frac{e^{\gamma z} - e^{-\gamma z}}{e^{\gamma z} + e^{-\gamma z}} = Z_{wg} \tanh(\gamma z)$$

$Z_{wg} = \frac{V_0}{I_0}$ is the characteristic impedance of the waveguide. It can be computed from [2, (11a)] for TE-modes, the value $Z_0 = 377\Omega$, and the relations (1.5):

$$Z_{wg} = Z_0 \frac{\lambda_g}{\lambda_0} \tag{1.10}$$

Substituting the identity for the propagation constant and defining the terminal plane as the distance d from the short, we can make a few approximations. Firstly, we can use the trigonometric identities: $\tanh(x+y) = \frac{\tanh x + \tanh y}{1 + \tanh x \tanh y}$, and $\tanh(i \cdot x) = i \tan x$, giving:

$$Z = Z_{wg} \tanh[(\alpha + j\beta)d] = Z_{wg} \frac{\tanh(\alpha d) + j \tan(\beta d)}{1 + \tanh(\alpha d) \tanh(\beta d)}$$

For low losses $\alpha d << 1$. Moreover, near resonance $\beta d \approx \pi$. Therefore, we can approximate:

$$Z \approx Z_{wg}(\alpha d + j \tan(\beta d))$$

Version of July 8, 2021– Created July 8, 2021 - 13:14

Instead of the tan function, the imaginary term is more suitably written as a product of constants. In the next section, we will see matching the cavity with an iris or stub will alter the resonant frequency of the cavity. Near resonance, the deviating angular frequency ω can be implemented by taking $\beta(\omega)$ close to the value for which the "boxed" cavity is resonant. By "boxed" cavity will henceforth mean the case of box-shaped domain of dimensions $a \times b \times d$ completely encapsulated by conductors, as opposed to being completely open at a $a \times b$ surface (shorted waveguide) or having a circular aperture at that plane (iris-matched cavity). In order to get the properties of the TE_{101} cavity, we need to set the depth d of the cavity along $\hat{z}$ to $d = \frac{\lambda_g}{2}$, where λ_g is the guide wavelength associated with the resonant frequency by (1.5a) of the cavity with resonant frequency (1.6) for dimensions $a \times b \times d$. Suppose $\beta_0 \equiv \beta(\omega = \omega_0)$ is the guide wave vector for angular resonant frequency ω_0 of the boxed cavity. Then a deviating angular frequency $\omega \approx \omega_0$ near the resonant angular frequency would produce a new wave vector β along $\hat{z}$ according to Taylor's theorem:

$$\beta(\omega)|_{\omega \approx \omega_0} = \beta_0 + \frac{\partial \beta(\omega_0)}{\partial \omega} \cdot (\omega - \omega_0)$$

We then use the chain rule:

$$\frac{\partial \beta(\omega_0)}{\partial \omega} = 2\pi \frac{\partial (\lambda_g)^{-1}}{\partial \lambda_0} \frac{\partial \lambda_0}{\partial \omega} \delta = \frac{2\pi}{\lambda_g} \frac{\lambda_g^2}{\lambda_0^2} \frac{\delta(\omega)}{\omega_0}, \ \delta(\omega) = \omega - \omega_0$$

This can be substituted to give:

$$\tan(\beta d) = \tan\left[\pi \cdot \left(1 + \left(\frac{\lambda_g}{\lambda_0}\right)^2 \frac{\delta}{\omega_0}\right)\right] \approx \frac{\lambda_g^2}{\lambda_0^2} \frac{\pi}{\omega_0} \delta$$

The impedance of a shorted waveguide, a distance l from the short is thus:

$$Z \approx Z_{wg}\left(\alpha d + j \frac{\lambda_g^2}{\lambda_0^2} \frac{\pi}{\omega_0} \delta\right)$$

For the impedance of a series RLC circuit, where $\omega_0^2 = \frac{1}{LC}$, we have:

$$Z = R + jX = R + j\left(\omega L - \frac{1}{\omega C}\right) = R + j2L\delta$$

Combining the last two equations, we get the formulae for the (longitudinal) resistance and inductance of a short-circuited length of waveguide:*

*The resistance of the short-circuited length of waveguide is not represented properly by R_l alone, which leads to it being given the subscript l. The resistance including the transverse walls, R, is given in the section on matching.

Version of July 8, 2021– Created July 8, 2021 - 13:14

$$R_l = Z_{wg}\alpha d \tag{1.11a}$$

$$L = \frac{Z_{wg}}{2}\frac{\lambda_g^2}{\lambda_0^2}\frac{\pi}{\omega_0} \tag{1.11b}$$

For a series RLC circuit, the formulae for the angular resonance frequency ω_0 and the quality factor Q are generally known to be:

$$\omega_0 = \frac{1}{\sqrt{LC}} \tag{1.12}$$

$$Q = \frac{\omega_0 L}{R} \tag{1.13}$$

Iris-coupled shorted waveguide

We can view our setup as a resonant series R,L,C circuit. Resonance is achieved by the insertion of an iris at $d \approx n \cdot \lambda_g/2$ from the short. The depth d of the cavity has circuit parameters R, L, C, and a circular aperture in transverse direction has inductance $\mathcal{L}$ which can be inserted in parallel with the cavity parameters R, L, C. This is represented in figure 1.1a.

More suitably, we would like to write the entire circuit of lumped nodes that are all in series, meaning that the iris inductance is brought from parallel to series relation to the cavity parameters. We can do this by making an approximation for the impedance in front of the terminal plane, with $Z_a = Z_{wg}$, $Z_b = i\omega\mathcal{L}$, and the formula $\frac{1}{Z_{tot}} = \frac{1}{Z_a} + \frac{1}{Z_b}$ for two parallel impedances Z_a and Z_b. Rewriting the parallel source impedance in Figure 1.1a to a series impedance, we get:

$$Z = \frac{i\omega\mathcal{L}Z_{wg}}{Z_{wg} + i\omega\mathcal{L}} \cdot \frac{Z_{wg} - i\omega\mathcal{L}}{Z_{wg} - i\omega\mathcal{L}} \approx i\omega\mathcal{L} + \frac{\omega^2\mathcal{L}^2}{Z_{wg}}$$

for $\omega\mathcal{L} << Z_{wg}$, which is the case of high Q systems.

1.1.3 Matching

The matching of the cavity will prove to involve the most tedious mathematics. Therefore, we will be referring to the derivation of formulae in literature [4] rather than explain these in order to keep this section concise. Our plan of attack will be very structured. Firstly, the Q of a boxed cavity (no iris) will be determined. Then from this Q of the cavity and its known inductance L, we will determine its resistance R. Thereafter, we

Version of July 8, 2021– Created July 8, 2021 - 13:14

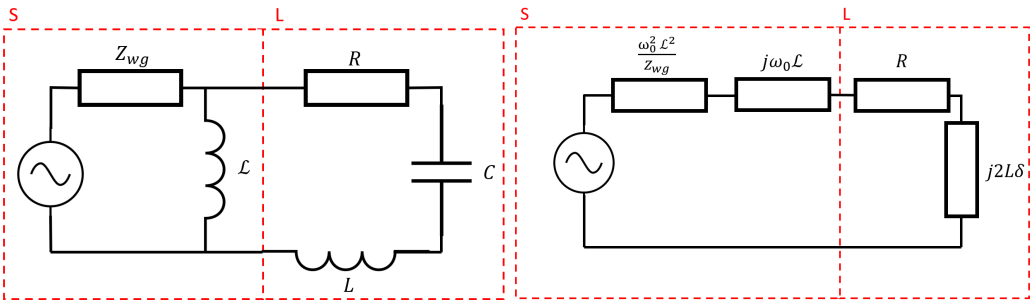

(a) *Parallel* ***(b)*** *Series*

Figure 1.1: *Equivalent circuit for 1cav, parallel and series expressions. The terminal plane of the iris is represented by the vertical dotted line in between S and L.*

will introduce matching by setting up an analogy between the shorted cavity with iris and an L-section. Matching criteria will be determined for an L-section, and these will then be projected on the normalized impedance values of a cavity resonator in order to determine the required iris inductance $\mathcal{L}$ as mentioned in the previous section. Finally, a formula is advanced for the iris radius r_0 in terms of cavity dimensions and the value of $\mathcal{L}$. Simulations and the experimentally used iris radius will later be found to equal the calculated iris radius for matching.

When a guide is short-circuited at a load, the superposition of the incoming wave and the reflected wave creates a standing wave. The power absorbed at the load is maximized if the reflected voltage $\Gamma \equiv |S_{11}|$ is zero, so if $Z_S = Z_L^*$ by (1.14).

$$|S_{11}| = \frac{Z_S - Z_L^*}{Z_S + Z_L}, \quad |S_{11}|^2 = \frac{|Z_S - Z_L^*|^2}{|Z_S + Z_L|^2} \tag{1.14}$$

In this case, the cavity (load) is said to be 'matched' to the waveguide (source). This is also formulated as 'critical coupling' by the iris. The characteristic impedance of the waveguide is $Z_S = \frac{V_0}{I_0} = Z_{wg}$. In most literature on RF, to circumvent involving Z_{wg} coefficients in our calculations, calculations are made in terms of normalized impedance defined as $\bar{Z} \equiv \frac{Z}{Z_{wg}}$. Interpreting the load as the cavity ($Z_L = R + iX$) and the source as the waveguide ($Z_S = Z_{wg} + iX_{wg}$), we thus arrive at two criteria by which we will determine the condition for critical coupling (read: matching) for $\omega = \omega_0$: (1.15) and (1.16). Here, $\kappa = R/R_l$ is the normalization factor raising the waveguide resistance R_l to the cavity resistance R.

$$Z_{wg} = R_L \rightarrow \frac{\omega_0^2 \mathcal{L}^2}{Z_{wg}} = R = \frac{\omega_0 L}{Q_0} = \kappa Z_{wg} \alpha l \tag{1.15}$$

$$X_{wg} = -X \rightarrow \omega_0 \mathcal{L} = -2L\delta = -(-\omega_0 \mathcal{L}) \tag{1.16}$$

First of all, it is worth pointing out that the second matching criterion (1.16) is automatically satisfied. As we will see in our calculations of the lumped element parameters later on, the inductance L of the cavity is in order 100 [nH] whereas the inductance $\mathcal{L}$ of the iris is in the order 1 [nH]. The influence of the iris can be equated to an increase in the total system inductance $L \rightarrow L' = L + \mathcal{L}$, and therefore as a decrease in the system resonant frequency $\omega_0 \rightarrow \omega_0'$. By (1.12) and $\mathcal{L} << L$:

$$\omega_0' = \frac{1}{\sqrt{L' \cdot C}} = \frac{1}{\sqrt{(L+\mathcal{L}) \cdot C}} = \frac{1}{\sqrt{L \cdot C}} \cdot \frac{1}{\sqrt{1 + \frac{\mathcal{L}}{L}}} \approx \omega_0 \cdot \left(1 - \frac{1}{2}\frac{\mathcal{L}}{L}\right)$$

The shifted angular resonance frequency ω_0' due to insertion of the iris therefore causes a default cavity reactance X_L equal to the complex conjugate of the source reactance X_S associated with its insertion. In other words, the iris slightly decreases the cavity resonance frequency in order to compensate for its reactance so as to ensure that matching depends only on the real impedance.

$$X_L = -j2L\delta = -j2L \cdot (\omega_0' - \omega_0) = -j2L \cdot \frac{1}{2}\frac{\mathcal{L}}{L}\omega_0 = -j\mathcal{L}\omega_0 = -X_S$$

Therefore, we may conclude that (1.16) is automatically satisfied and that only (1.15) is of concern when determining the iris radius to match the cavity to the waveguide. Before continuing to the issue of matching the real impedances, it is worth pointing out that the iris reactance X_{ir} changes the resonant frequency of the cavity. For a TE_{101}-mode, this iris reactance is compensated by (slightly) decreasing the cavity depth by an amount $\Delta d = \omega_0 L/(Z_{wg} \cdot \beta)$.

Determination of cavity resistance R

We aim to satisfy criterion (1.15) by computing the resistance of the iris-coupled waveguide R which needs to be equal to the cavity resistance R_L. In order to find what radius r is required for matching, the waveguide resistance is already known from (1.10), leaving us to determine two aspects: the resistance of the cavity and the coupling associated with the iris radius.

Version of July 8, 2021– Created July 8, 2021 - 13:14

As for the resistance of the cavity, (1.11a) provides a resistance that is lower than the actual cavity resistance: it yields the resistance over some depth of waveguide d. As for the cavity, however, this "longitudinal" resistance does not take into account losses at the cavity's two transverse planes; at the short and at the aperture plate. This discrepancy can be exposed by use of the "boxed cavity" quality factor, "boxed" indicating a TE_{101} cavity completely encapsulated by walls. This boxed quality factor Q_0 can be determined from cavity volume and -surface integration over the squared magnitude of the magnetic field equations [4, (7.48)], corresponding to the rectangular TE_{101} mode formalized in (1.27b) by derivation from (1.8). Substitution yields (1.17a).

$$Q_0 = \frac{\omega W}{P_l} = \frac{(k_0 a d)^3 b Z_0}{2\pi^2 R_m (2a^3 b + 2d^3 b + a^3 b + d^3 a)} \tag{1.17a}$$

$$W = 2 \cdot W_m = \frac{\mu_0}{4} \iiint_{V_s} |H|^2 d\tau \ , \quad P_l = \frac{R_m}{2} \oiint_S |H|^2 dS \tag{1.17b}$$

$$R_m = \frac{1}{\sigma \delta_s} = \frac{1}{\sigma} \left(\sqrt{\frac{2}{\omega \mu_0 \sigma}} \right)^{-1} = \sqrt{\frac{\omega \mu_0}{2\sigma}}$$

By (1.15), the iris-matched cavity quality factor equals half the boxed quality factor Q_0 in (1.22b). In combination with (1.13), one can verify that $R > R_l$, and the actual cavity resistance should actually be higher.

It is important to now make a distinction between the resistance associated only power loss along the cavity depth - being the longitudinal resistance R_l -, and the power loss along the surface of the transverse cavity walls on either end of the cavity - being the transverse resistance R_t. The mode contained in the cavity induces currents along the six planes encasing the cavity, four of which are placed along its longitudinal direction $\hat{z} \times (\hat{x} \vee \hat{y})$, and two of which are placed along its transverse direction $\hat{x} \times \hat{y}$. The resistance of the cavity is previously given as R_l given in (1.11a). However, - for arbitrary a, b, c, σ - substituting R_l and (1.11b) into (1.13) gives a value for the quality factor that is much higher than when computed from (1.17a). Relying on the validity of (1.11b) this indicates that the resistance of the cavity is supposed to be higher than R_l alone. This leads us to the formula for the total cavity resistance R, which for a TE_{101} mode is:

$$R = R_l + R_t = (\frac{R_t}{R_l} + 1) \cdot R_l = \kappa \cdot R_l$$

This factor κ can be computed by comparison of the integral of power loss P for the TE_{101} to only the longitudinal boundaries S_l with respect to the

Version of July 8, 2021– Created July 8, 2021 - 13:14

integral of power loss over all boundaries (transverse and longitudinal) $S_t \cup S_l$. The integral expression [4, (7.46)] is applied to the mode field equations in (1.27). Expressing the power loss over planes S_t and S_l as P_t resp. P_l yields the equation (1.18), accounting for the resistance at the cavity's transverse planes. Per illustration, the case of a cubic cavity with $a = b = c$ yields $\kappa = 3/2$, exposing the necessity of accounting for the losses at the cavity's transverse planes.

$$\kappa = \frac{P_l + P_t}{P_l} = \frac{\oiint_{S_l \cup S_t} |H|^2 dA}{\iint_{S_l} |H|^2 dA} = \frac{2a^3b + 2d^3b + ad^3 + da^3}{2d^3b + ad^3 + da^3} \tag{1.18}$$

Determination of matching iris radius r

Making a circular aperture at either of these transverse planes causes a reduction in the quality factor due to the radiation of power through the aperture. Equation (1.15) gives the aperture inductance required for critical coupling.

From the geometry and conductivity of the cavity, we have thus deduced R_0, and from this we can determine the required iris inductance $\mathcal{L}_0$ needed to achieve matching. The only step left is to determine the iris radius r_0 for matching the waveguide with resistance Z_{wg} to a cavity with resistance R_0. In literature, the iris radius is expressed in terms of the iris reactance. The iris normalized reactance is:

$$\hat{X}_{L1} = \frac{\omega_0 \mathcal{L}}{Z_{wg}}$$

From [4, (5.41)], the normalized reactance of the matching iris radius r_0 for an infinitely thin iris-plate ($t = 0$) is given as (1.19).

$$\hat{X}_{L1} = \frac{1}{\hat{B}_{L1}} = \frac{8\beta r_0^3}{3ab} \tag{1.19}$$

We can thus write the iris inductance $\mathcal{L}$ in terms of the iris radius:

$$\mathcal{L} = \frac{8 Z_{wg} \beta}{3\omega_0 ab} \cdot r^3$$

However, ignoring the thickness of the iris-plate containing the aperture gives only an approximation of its inductance, because a circular mode with admittance Y_1 and guide wavelength λ_{g1} is briefly held along its thickness t. In practice, this slight cutoff by the iris-hole decreases the

Version of July 8, 2021– Created July 8, 2021 - 13:14

iris reactance $\mathcal{L}$ significantly, thus requiring larger r than in the case $t = 0$. In order to illustrate by orders of magnitude involved: the iris radius on $t = 1$ mm that matches a WR-340 waveguide to a TE-101 cavity is raised from about 9 to 10 mm. This is a significant difference, forcing us to expand the theory on matching slightly more with the perturbed values of iris reactance for some thickness t. A thick iris is modelled by the circuit as depicted in 1.1a, but with the iris inductance X_{ir} substituted by a Π-section. Two parallel reactances X_a with double the initial reactance as well as a thickness perturbation. In between these is a series reactance X_b only depending on the iris thickness, but this is usually so small that we will ignore it. The reactances can be computed from formulae that have are directly taken from [2, paragraph 5.4]:

$$\frac{1}{X_a} = \frac{B}{2} + Y_1 \cdot \tanh\left(\frac{\pi t}{\lambda_{g1}}\right) \tag{1.20a}$$

$$Y_1 = \frac{1}{Z_{wg}} \cdot \frac{0.446ab\lambda_g}{d^3} \cdot \sqrt{1 - \left(\frac{p \cdot d}{\lambda_0}\right)^2} \tag{1.20b}$$

$$\lambda_{g1}(r) = \frac{p \cdot d}{\sqrt{1 - (\frac{p \cdot d}{\lambda_0})^2}},\ p = 1.706 \tag{1.20c}$$

Because of the complexity of calculations involved with iris thickness, it is hard to solve the required matching radius r with the thickness correction directly incorporated in calculations. Therefore, it is best to introduce some approximate correction $\psi(r_0)$ to the matching iris radius for zero thickness $r_0 = r(t = 0)$, easily found from (1.19). Because $\psi(r_0)$ is a small correction, we may approximate it as locally constant such that the required iris reactance $X(r_t)$ such that r_t gives matching for thickness t is about equal to the iris reactance $X(r_0)$ such that r_0 gives matching for zero thickness $t = 0$ multiplied by a correction factor $\psi(r_0)$:

$$X_t(r) = \psi|_t(r) X_{t=0}(r) \approx \psi(r_0) \cdot X(r_0)$$

, where

$$\psi(r)|_t = \frac{X_{t=0}(r)}{X_t(r)} = \frac{X_a(r)|_{t=0}}{X_a(r)|_t} = (1 + \frac{4\pi t Y_1(r)}{\lambda_{g1}(r) \cdot B(r)})^{-1}$$

Inserting the functions (1.20) in the above equation yields:

$$\psi(r)|_t = \frac{1}{1 + 3.44 \cdot \frac{t}{r}(1 + (\frac{2pr}{\lambda_0})^2)} \tag{1.21}$$

Version of July 8, 2021– Created July 8, 2021 - 13:14

This factor ψ can then be implemented as a correction into the factor a relating the iris inductance to the iris radius. The correction factor has an influence on the quality factor and mismatch, but not on the resonant frequency.

The covered theory can be encapsulated in equations (1.22), with formulae for the corrections κ and ψ given in (1.18) resp. (1.21). The equation for the mismatch (1.22c) assumes the iris-coupled cavity resonance frequency (1.22a), meaning that the mismatch is dependent on resistance only, independent of the reactance. Additional power reflection is caused by non-zero reactance brought on by deviation of the input frequency from the iris-coupled cavity's resonance frequency; this leads to the Lorentzian curve.

$$f_0 = \frac{1}{2\pi}\frac{1}{\sqrt{(L+\mathcal{L})\cdot C}} = \frac{\omega_0}{2\pi} \tag{1.22a}$$

$$Q = \omega_0 \frac{L+\mathcal{L}}{R_0 + \frac{\omega_0^2\mathcal{L}^2}{Z_{wg}}} \tag{1.22b}$$

$$\Delta M = |\Gamma|^2 = \left|\frac{R_S - R_L}{R_S + R_L}\right|^2 = \frac{\frac{\omega_0^2\mathcal{L}^2}{Z_{wg}} - R_0}{\frac{\omega_0^2\mathcal{L}^2}{Z_{wg}} + R_0} \tag{1.22c}$$

$$\mathcal{L}(r)|_t = a_0 \cdot \psi(r)|_t \cdot r^3, \;\; a_0 = \frac{Z_{wg}}{\omega_0}\frac{8\beta}{3ab} \tag{1.22d}$$

$$R_0 = \frac{\omega_0 L}{Q_0} = \kappa \cdot Z_{wg} \cdot \alpha \cdot d \tag{1.22e}$$

The Lorentzian curve

The RF-parameters f_0, Q, and ΔM are three parameters defining the frequency-dependent power reflection curve $|S_{11}|^2(f)$ of the (plasma-filled) cavity system for an incoming RF-signal with a certain frequency f. The power reflection at signal frequency f is determined by its deviation from the resonance frequency $\Delta f \equiv f - f_0$ (which we will henceforth call the *mistune*), by the base power reflection $\Delta M = |S_{11}|^2(f = f_0)$, and lastly by the quality factor, which determines the frequency-dependent power reflection attenuation from the magnitude of the frequency shift $|f - f_0|$ over the FWHM (full-width-half-max). The FWHM $\Delta f_{1/2}$ is defined such that within the range $f \in [f_0 - \Delta f_{1/2}, f_0 + \Delta f_{1/2}]$, power reflection is at most twice the minimum power reflection: $|S_{11}|^2(f_0 \pm \Delta f_{1/2}/2) = (1/2)\cdot(1 + \Delta M)$.

The signal frequency deviation Δf from cavity resonance frequency f_0 yields a surplus load inductance $X = i \cdot 4\pi \cdot L \cdot \Delta f$ by (1.11b), which in turn causes a surplus power reflection by (1.14). Evaluating the power reflection (1.14) over a range f around f_0 yields the power reflection curve in (1.23b), which is known as a Lorentzian curve [5, (2.15)]. Its shape is visualized in Figure 2.5b.

$$Q \equiv \frac{f_0}{\Delta f_{1/2}} \tag{1.23a}$$

$$|S_{11}|^2(f) = 1 - \frac{1 - \Delta M}{\left(\frac{2Q \cdot (f - f_0)}{f_0}\right)^2 + 1} \tag{1.23b}$$

Matching using stub

Even having used such expansive theory on the matching with a circular iris, in practice there will always be corrections or errors not taken into account in calculations, thus leading to some small mismatch under r_0. The iris aperture radius is usually a pre-built component, making "fine-matching" difficult. In order to match the cavity reliably, it is customary to decrease the iris coupling by taking the iris radius a few tenths millimetre larger than r_0, and to insert a cylinder axisymmetric with the E-field at the E-field anti-node $\lambda_g/4$ in front of the iris with which coupling can be perfected. This is called stub-matching, which can easily be implemented by screwing or unscrewing a bolt protruding through the waveguide wall. For theory on this, refer to the literature of the capacitive post addressed in [2, paragraph 5.14].

1.2 Cavity perturbation theory

Cavity perturbation theory (CPT) can be used to derive characteristics of the plasma from the associated resonant frequency and quality factor shift. The frequency shift, in turn, can be computed for both a perfectly conducting volume and for a resistive volume. Moreover, we can predict the compensated dimensions for a cavity containing a large amount of dielectric.

General CPT equation

CPT can be encapsulated into the general formula:

Version of July 8, 2021– Created July 8, 2021 - 13:14

$$\frac{\tilde{f}_s - \tilde{f}_0}{\tilde{f}_0} = -\frac{\iiint_{V_s}(\Delta\mu|H|^2 + \Delta\epsilon|E|^2)d\tau}{\iiint_{V_0}(\mu_0|H|^2 + \epsilon_0|E|^2)d\tau} \tag{1.24}$$

Here, $\tilde{f}_s \equiv Re(\tilde{f}_s) + i \cdot Im(\tilde{f}_s)$ and $\tilde{f}_0 \equiv Re(\tilde{f}_0) + i \cdot Im(\tilde{f}_0)$ are the complex frequencies of the perturbed and unperturbed cavity respectively. V_s and V_0 are the volume of the sample and the cavity respectively. The permittivity and permeability of the sample are given by ϵ_s resp. μ_s. This makes the difference in sample- permittivity and -permeability the values $\Delta\epsilon \equiv \epsilon_s - \epsilon_0$ and $\Delta\mu \equiv \mu_s - \mu_0$, representing their difference for the perturbed and unperturbed case respectively. It is convenient to normalize both by division by their respective free-space values. This gives the relative permittivity:

$$\epsilon_r \equiv \frac{\epsilon}{\epsilon_0}$$

1.2.1 Frequency shift and quality factor from sample below cutoff

It is convenient to simplify the expression on the right hand side. Firstly, the expression in the denominator equals the total energy W stored in the cavity. The energy stored in the cavity is the sum of equal electric- and magnetic field energy by [4, top of p. 503]. Therefore, the integral over the two integrands equals twice the integral over the second integrand. Secondly, for the numerator we set $\Delta\mu = 0$, because for the purposes of this paper only the perturbation from the difference in complex permittivity $\Delta\epsilon$ will be considered. This leaves us with the fraction of volume integrals of the electric field energy density. For simplification, we convert the volume integrals over position-dependent energy density to a product of volume times average energy density. For a small sample placed at the E-field antinode of the rectangular TE_{101}-cavity, we will later determine the fraction of energy densities to be $\chi_E = 4$.

From power reflection measurements on the cavity, we will determine the relative permittivity of the sample by the complex resonance frequency shift. As we will determine from (1.24)[†], the real part $\Delta\epsilon_r'$ perturbs the real-valued resonant frequency shift and the imaginary part $\Delta\epsilon_r''$ perturbs the imaginary-valued resonant frequency shift, the latter embedded in the

[†]For objects well below cutoff, meaning that the surrounding field fully penetrates the sample.

quality factor. By [6], the quality factor of a system α with complex resonant frequency $\tilde{f_\alpha} \equiv Re(f_\alpha) + Im(f_\alpha) \cdot i$ is defined as:

$$Q \equiv \frac{Re(\tilde{f_\alpha})}{2 \cdot Im(\tilde{f_\alpha})} = \frac{f_\alpha}{\Delta f_{\alpha,1/2}} \tag{1.25}$$

The imaginary part of the resonant frequency can be determined experimentally from a frequency sweep f near the resonant frequency as the Full-Width-Half-Max of the power reflection curve $|S_{11}|^2(f)$. This yields $|S_{11}|^2(f_\alpha \pm \Delta f_{\alpha,1/2}/2) = (1/2) \cdot (1 + \Delta M)$, where $\Delta M = |S_{11}|^2(f_\alpha)$ is the minimum power reflection, which is attained at the (real) resonant frequency. These properties produce a Lorentz curve, used for data analysis given by [5, (2.15)].

For a small sample well below cutoff, placed at the E-field antinode of the rectangular TE_{101}-cavity, the value of the constant χ_E equals four. The meaning of this constant is the ratio of field energy density at the sample with respect to the average over the cavity volume, and the determination of its value will be explained soon. We can relate the frequency shift and quality factor to the sample's relative permittivity with (1.26) where we assume empty cavity as free space such that $\Delta\epsilon_r = \epsilon_r - 1$.

$$\Delta f \equiv f_s - f_0 = -\frac{\chi_E}{2} \cdot \frac{V_s}{V_0} \cdot \Delta\epsilon_r' \cdot f_0 \tag{1.26a}$$

$$\frac{1}{Q_s} - \frac{1}{Q_0} = \chi_E \cdot \frac{V_s}{V_0} \cdot \Delta\epsilon_r'' \tag{1.26b}$$

As we will see from Drude theory, the difference in real relative permittivity of a plasma $\Delta\epsilon_r'$ is always negative. Therefore, the corresponding frequency shift is always positive. In measurements on the plasma, however, a downward frequency shift is measured (see Figure 2.2a). This cannot be the result of the sample dielectric, and we will see that this is the result of cutoff, where the field energy within the sample is reduced with respect to its surroundings.

Field equations in rectangular and cylindrical cavity

As will be identified from the central CPT equation (1.24), it will come in handy to know the field equations of the electric and magnetic field in the rectangular and cylindrical modes to be investigated. Relevant here is to determine the field magnitude near the plasma E_0 / B_0 relative to the average field magnitude across the cavity $< E >$ / $< B >$.

The field equations of the rectangular TE_{101}-mode can be determined from (1.8) in combination with (1.9) to give equations (1.27).

$$\mathbf{E}(x,y,z) = E_0 \cdot \sin(k_c x) \cdot \sin(\beta z) \cdot \hat{y} \tag{1.27a}$$

$$\mathbf{B}(x,y,z) = B_0 \cdot \sin(k_c x) \cdot \cos(\beta z) \cdot \hat{x} + B_0 \cdot \cos(k_c x) \cdot \sin(\beta z) \cdot \hat{z} \tag{1.27b}$$

The field equations of the cylindrical TE_{011}-mode (subscript denoting $2\pi, \pi, \pi$ periodicity respectively in ϕ, r, z) for a cylindrical cavity with radius a are useful later on, but will not be derived here. In [7, paragraph 2.19], field equations for the travelling cylindrical TE_{01}-mode over r are derived in terms of the zeroth order Bessel function of the first kind J_0, and its derivative $J_0' \equiv \partial J_0 / \partial r$. These equations reconcile condition (1.4a) with $E \propto J_0'(\nu \cdot r/a) \cdot \hat{\phi}, \nu \in \mathbb{R}$, and satisfy half-periodicity in r by requiring: $\nu = X_{01}'$ equals the first root of J_0' [2, table 2.2]. In combination with the superposition relation in (1.9), the travelling wave TE_{01}-mode equations produce the standing wave TE_{011}-mode equations in (1.28).

$$\mathbf{E}(r,\phi,z) = E_0 \cdot \frac{\lambda_c}{\lambda_g} \cdot Z_0 \cdot J_0'\left(\frac{X_{01}' \cdot r}{a}\right) \cdot \sin\frac{2\pi \cdot z}{\lambda_g} \cdot \hat{\phi} \tag{1.28a}$$

$$\mathbf{B}(r,\phi,z) = B_0 \cdot \frac{\lambda_c}{\lambda_g} \cdot J_0'\left(\frac{X_{01}' \cdot r}{a}\right) \cdot \cos\left(\frac{2\pi \cdot z}{\lambda_g}\right) \cdot \hat{r} + \tag{1.28b}$$

$$B_0 \cdot J_0\left(\frac{X_{01}' \cdot r}{a}\right) \sin\left(\frac{2\pi \cdot z}{\lambda_g}\right) \cdot \hat{z} \tag{1.28c}$$

$$\lambda_c = \frac{2\pi \cdot a}{X_{01}'}, \quad X_{01}' = 3.832$$

For CPT purposes, we will extract the essential information about the field energy density w_Y distributions, being the absolute square of these field distributions. For the purposes of heating, the plasma is placed at a field antinode, where the field magnitude $|Y|^2$ attains its maximum magnitude Y_0^2 with the other field at zero density. For resulting perturbations Δf and ΔQ^{-1} by the plasma on the empty cavity RF-properties f_0 resp. Q_0, we require the ratio of the field energy density near the plasma over the average field energy density across the cavity volume. We will call this ratio χ_Y, which for the field type $Y \in \{E, B\}$ with a small sample ($V_s \ll V_0$) at the field antinode, equals:

$$\chi_Y \equiv \frac{\iiint_{V_s} |Y(x_1,x_2,x_3)|^2 d\tau}{\iiint_{V_0} |Y(x_1,x_2,x_3)|^2 d\tau} \frac{V_0}{V_s} \approx Y_0^2 \cdot \frac{V_0}{\iiint_{V_0} |Y(x_1,x_2,x_3)|^2 d\tau} \tag{1.29}$$

The values of χ for both fields, and both modes (1.27) resp. (1.28) are computed for future reference. Values for the rectangular cavity modes are determined analytically. Values for the cylindrical mode are determined numerically for radius $a = 82$ mm and height $h = 150$ mm, and might therefore vary for different (a, h).

	rectangular: TE_{101}, TE_{102}	cylindrical: TE_{011}
χ_E	4	4.18
χ_B	2	10.24

Table 1.1

1.2.2 Frequency shift from insertion of dielectrics

When addressing the frequency shift due to the presence of a dielectric, it will be useful to refer to the values of their characteristic real relative permittivity $Re(\epsilon_r) = \epsilon_r'$ to deduce order of magnitudes. The materials we will be working with are air, helium, and fused quartz. Their relative permittivities are as follows by [8] and [9] the values in Table 1.2.

	Air	He_2	Quartz, fused Si O_2
ϵ_r'	1.00059	1.000065	3.78
$\Delta\epsilon'_{r,Air\to x}$	0	-5.25e-4	2.78
ϵ_r''	≈ 0	≈ 0	-4e-4

Table 1.2

The resonance frequency shift due to a non-absorbing dielectric in the cavity can be described by a real frequency shift. This particular subsection will not pertain to the characterization of plasma. Rather, it will address the shift in resonance frequency of the cavity due to substituting large parts or the entirety of the cavity volume with a different dielectric, and the re-tuning of the cavity when this shift is large. The dielectric is non-resistive, meaning that the imaginary parts of $\tilde{f}_s$ and $\tilde{f}_0$ on the left hand side of (1.24) cancel.

Insertion of dielectric in entire cavity volume

The resonance frequency due to the insertion of a different dielectric within the entire cavity domain can be evaluated by simplifying (1.24) under the

assumption of total field energy $W = \iiint_{V_0}(\mu_0|H|^2 + \epsilon_0|E|^2)d\tau = 2\iiint_{V_0}(\epsilon_0|E|^2)d\tau = 2 \cdot W_E$ equal to twice the E-field energy, and with the substitution $V_s = V_0$ in the numerator; yielding (1.30).

$$\Delta f = \frac{-f_0 \cdot W_E}{W}\frac{\Delta\epsilon}{\epsilon_0} = \frac{-1}{2} \cdot \Delta\epsilon_r' \cdot f_0 \tag{1.30}$$

The validity of this formula can be tested by considering the effect of filling the cavity with gases of two different relative permittivities, and measuring the shift in resonance frequency. For substitution of air with helium, for example, $\Delta\epsilon_r' \approx -5e-4$. The resulting frequency shift is only very small; in the order of $\Delta f \approx +7$ MHz $\ll f_0$. We see that for the dielectric and cavity volumes in the same order of magnitude $V_s \approx V_0$, the frequency shift is in the order $\Delta f \approx -\Delta\epsilon_r' \cdot f_0$. If, however, we were to have a large difference in permittivity over a significant part of the cavity, the frequency shift will be very large. In the case of substituting parts of the air-filled cavity with fused quartz, such that $\Delta\epsilon_r' = 2.78$, the frequency shift will be in the order of magnitude of the old cavity resonant frequency, such that the cavity needs to be 'retuned' to the magnetron frequency. Per illustration, disregarding any frequency shift due to $\Delta\mu$ of the fused quartz cavity: if we fill an air-filled cavity previously resonant at 2.45 GHz with fused quartz, then $\Delta f_{Air\to FQ} = (1/2) \cdot f_0 \cdot \Delta\epsilon_r' = 3.43$ GHz. This issue of retuning will now be addressed.

1.2.3 Frequency tuning for cavity with dielectric slabs

In our case, two 10 mm thick slabs of FQ will be placed in the cavity, placed some distance apart. We will derive the total length of the cavity for a given window distance in order to satisfy tuning at some frequency. We do this by substituting the formula for the resonant frequency for given cavity dimensions into the left hand side (LHS) of (1.24), and solve the equation for the occupation of the electric field energy density and relative permittivity shift at the right hand side (RHS).

As will eventually be discussed, we need to find the required cavity depth d containing a TE_{102} mode in case of two windows with thickness δ placed symmetrically to the half-depth $z = d/2$ of the cavity. The windows are placed a distance w apart, and have a real relative permittivity ϵ_r that is $\Delta\epsilon_r \approx \epsilon_r - 1$ higher than the surroundings. From (1.8), we see that the electric field is distributed as a sine. The electric energy is therefore distributed as a sine squared, and the total electric energy is half the total cavity energy. Implementation in (1.24) yields:

Version of July 8, 2021– Created July 8, 2021 - 13:14

$$\frac{f_0' - f_0}{f_0} = -\frac{\Delta\epsilon_r}{2}\left[\int_{(d-w-\delta)/2}^{(d-w+\delta)/2} \sin^2\left(\frac{2\pi z}{d}\right)dz + \int_{(d+w-\delta)/2}^{(d+w+\delta)/2} \sin^2\left(\frac{2\pi z}{d}\right)dz\right]$$

We will denote the left hand side and right hand side of this equation by LHS and RHS respectively. The windows are placed symmetrically in the half-plane. The electric field is symmetric in the half-plane as well. This symmetry leads to an equal value of the integrals. Therefore, we can rewrite RHS to:

$$-\Delta\epsilon_r \int_{(d-w-\delta)/2}^{(d-w+\delta)/2} \sin^2\left(\frac{2\pi z}{d}\right)dz =$$
$$-\frac{2}{d}\Delta\epsilon_r\left\{\frac{d}{8\pi}\left[\sin\left(\frac{2\pi}{d}(-d+w+\delta)\right) - \sin\left(\frac{2\pi}{d}(-d+w-\delta)\right)\right] + \frac{\delta}{2}\right\}$$

As for the LHS, we can use the formula for the resonance frequency of a cavity as (1.6):

$$f_0 = \frac{c}{2}\sqrt{(\frac{m}{a})^2 + (\frac{n}{b})^2 + (\frac{l}{d})^2}$$

We have $m = 1, n = 0, l = 2$ with $d = \lambda_g$. To tune the lower resonant frequency resulting from the dielectric, we need a shorter cavity depth $d < \lambda_g$ to be implemented into this same term. We thus get

$$\frac{f_0' - f_0}{f_0} = \frac{\frac{c}{2}\sqrt{(\frac{1}{a})^2 + (\frac{2}{d})^2} - \frac{c}{2}\sqrt{(\frac{1}{a})^2 + (\frac{2}{\lambda_g})^2}}{\frac{c}{2}\sqrt{(\frac{1}{a})^2 + (\frac{2}{\lambda_g})^2}}$$

Which can be simplified to:

$$\frac{f_0' - f_0}{f_0} = \sqrt{\frac{a^{-2} + 4d'^{-2}}{a^{-2} + 4\lambda_g^{-2}}} - 1 \tag{1.31}$$

For our total equation, we arrive at:

$$1 - \sqrt{\frac{a^{-2} + 4d'^{-2}}{a^{-2} + 4\lambda_g^{-2}}} = \Delta\epsilon_r \int_{(d-w-\delta)/2}^{(d-w+\delta)/2} \sin^2(\frac{2\pi z}{d})\, dz \tag{1.32}$$

Solving this equation for d gives the required cavity depth for tuning at f_0 in case of a window distance of w and window thickness δ.

Version of July 8, 2021– Created July 8, 2021 - 13:14

1.2.4 Frequency shift from sample beyond cutoff

When studying the frequency shift by a sample beyond cutoff, we ought to study the electric field inside the sample. This issue is addressed in [10], and equations derived there are mentioned in this subsection, though with a minor correction $1/x$. The paper states that the frequency shift is proportional to the sample volume V_s. The paper only addresses thin films, and therefore, amendments need to be made for 'thick' samples. To account for the structure shape, we determine its shape factor x, inspired by [5, p. 16]. The shape factor x is the share of sample surface area that is orthogonal to the E-field-direction y. In the case of a torus, this shape factor is $x = 1/2$, and for a very flat disk with $a \gg h$ the shape factor is $x = 1$. Through simulations on different shapes, the author has found that the frequency shift is inversely proportional to the shape factor.‡ This means that for a flat disk axisymmetric to the electric field, an axisymmetric torus of the same volume causes twice the frequency shift. The equation for the frequency shift for the sample beyond cutoff is (1.33a). It is analogous to [10, (12)] multiplied by the inverse of the shape factor as in x^{-1}.

$$\frac{\Delta f}{f_0} = \frac{-1}{2} \cdot \frac{\chi_Y}{x} \cdot \frac{V_s}{V_0} \tag{1.33a}$$

$$x \equiv \frac{1}{\frac{A_\parallel}{A_\perp} + 1}$$

Note that the frequency shift for a sample well beyond cutoff is independent of the permittivity. The reason for this is that in a sample well beyond cutoff, neither the electric field nor magnetic field permeate far into the sample because of (primarily) the skin effect. Small perturbations in the permittivity properties of the sample do not influence the frequency shift, because there is no field to respond to these changes.

By [10, (7)], the frequency shift due to the presence of a conductive torus ($x = 1/2$) at the magnetic field antinode is equal to the opposite sign of (1.33a), with χ_B instead of χ_E. For the TE_{10n} rectangular modes, therefore, the frequency shift of a cavity with an object at the magnetic field antinode is about $-1/2$ times the frequency shift of the same object at the electric field antinode within that cavity. However, simulations on such a configuration will expose that the frequency shift for the plasma at the magnetic field antinode is more tedious than for electric field antinode,

‡The author was unable to verify equation (1.33a) through analytical deduction. This proportionality can be easily tested in simulations by the analysis of frequency shift of different geometries with different shape factor but equal volume.

Version of July 8, 2021– Created July 8, 2021 - 13:14

because the full proportionality of V_s and Δf no longer holds. This issue is discussed in appendix **C**, where a function is fitted to simulation data. Nevertheless, by these same simulations the formula (1.33a) with substitution $\chi_E \rightarrow -\chi_B$ already provides an order of magnitude estimate of Δf for magnetic induction.

Although this paragraph marks the end of the section on CPT, CPT will be used for the formalization of additional equations in the section on electrodynamics at the end of this chapter. We have thus far only formalized equations for samples with two extremes of their material properties: well below cutoff and well beyond cutoff. In the section on electrodynamics, equations will be introduced for objects "around" cutoff.

1.3 Drude model

Having addressed CPT, the measurable quantities Q_s and f_s of the plasma-filled cavity can be converted to relative permittivity of the plasma sample. The next step is to convert the relative permittivity to properties of the plasma itself: charge density and temperature. This is done using a Drude model of plasma, which models the behaviour of the plasma - consisting of electrons and ions - as a "pinball" machine where these act as balls resp. bumpers. The RF-field accelerates only the electrons, and these subsequently lose their momentum to collisions with the ions. The fundamental equation for the Drude model is (1.34) [11, page 21, first equation].

$$\left(\frac{d}{dt} + \frac{1}{\tau}\right) < \mathbf{p}(\mathbf{t}) >= q \cdot \left(\mathbf{E} + \frac{< \mathbf{p}(\mathbf{t}) > \times \mathbf{B}}{m}\right) \tag{1.34}$$

The relaxation time of collisions is τ (not to be confused with the decay constant), which is the average time between collisions. The average momentum of the charges is $< \mathbf{p}(\mathbf{t}) >$, with their charge and mass given by q resp. m. Converting to plasma parameters, the charges are the electrons such that $q = e$ and $m = m_e$, and the relaxation time is equal to one over the electron-neutral collision frequency such that $\tau = \nu_{en}^{-1}$. In conventional (capacitive) heating systems, the charges are accelerated by the electric field, which oscillates at a frequency ω. Therefore, the time derivative of the momentum gives $d/dt < \mathbf{p}(\mathbf{t}) >= i\omega < \mathbf{p}(\mathbf{t}) >$. The electron momentum term can be eliminated by converting to its current density $\mathbf{J} \equiv e \cdot n_e < \mathbf{p}(\mathbf{t}) >$, which in turn can be related to the E-field with

Version of July 8, 2021– Created July 8, 2021 - 13:14

Ohm's law: $\mathbf{J} = \sigma\mathbf{E}$. Making these substitutions for the LHS and RHS independently we obtain the equation:

$$(\nu_{en} + i\omega)\frac{m_e}{e \cdot n_e}\mathbf{J} = \frac{e}{\sigma}\mathbf{J} \tag{1.35}$$

Complex conductivity

In equation (1.35), three degrees of freedom ν_{en} n_e and σ are related, with former two being "real" properties of the plasma and the latter being the single property describing RF-behaviour; the conductivity σ must therefore contain two degrees of freedom, making it a complex parameter. Its complex value will become clear under elimination of σ in (1.35), and in order to prevent confusion over its usual real value, it will be denoted with a Tilde, $\tilde{\sigma}$. We will now determine the expression for this complex conductivity.

In order to shorten the formalization of our equations, we will normalize the two parameters n_e and ν_{en} with the "normalized electron density" η and "normalized collision frequency" γ respectively [12]. This is done through division by n_c resp. ω:

$$\eta \equiv \frac{n_e}{n_c}, \quad n_c = \frac{m_e\omega^2\epsilon_0}{e^2} \tag{1.36a}$$

$$\gamma \equiv \frac{\nu_{en}}{\omega} \tag{1.36b}$$

The cutoff density n_c is a meaningful parameter derived under a different context in [13, (1.32)], and represents the approximate value of the electron density n_e beyond which the transmitted field undergoes significant attenuation. By (1.36), both η and γ depend on the field frequency ω; it is important to keep in mind that normalization of the same *real* parameters n_e and ν_{en} yield unique values of η and γ for different frequencies. Solving (1.35) for σ, we obtain the equation for the complex-valued conductivity $\tilde{\sigma}$:

$$\tilde{\sigma} = \omega\epsilon_0\eta\frac{\gamma - i}{1 + \gamma^2} \tag{1.37}$$

It is worth mentioning how to interpret the real and imaginary parts of the complex permittivity. We know from our pinball-model that if $\nu_{en} = 0 = \gamma \cdot \omega$ no losses occur. Therefore, the real part of the conductivity represents losses to power absorption in the plasma, as well as field

attenuation. Logically, the imaginary part of the conductivity might determine the propagation of waves through the sample. However, future use of the conductivity will only cover the real part, with the imaginary part of the conductivity being incorporated in the real value of the relative permittivity.

Complex permittivity

In order to relate to parameters required in CPT, we require a conversion of complex conductivity to complex permittivity, which is formalized in [13, (1.26)]:

$$\epsilon_r = \epsilon_r' - i\epsilon_r'' = 1 - i \cdot \frac{\sigma}{\epsilon_0 \omega} \tag{1.38}$$

Substitution of (1.37) in (1.38) yields:

$$\epsilon_r' = 1 - \frac{\eta}{1+\gamma^2} \tag{1.39a}$$

$$\epsilon_r'' = \frac{\eta\gamma}{1+\gamma^2} \tag{1.39b}$$

The (electron-neutral) collision frequency ν_{en} is dependent on the temperature of the plasma, in terms of $T_0 = 300$ [K]:[13, (4.24)]

$$\nu_{en} \approx n_a v_{th,el} < \sigma_a > \approx n_0 \frac{T_0}{T} \cdot v_0 \sqrt{\frac{T}{T_0}} < \sigma_a > \propto \sqrt{\frac{1}{T}} \tag{1.40}$$

The temperature-dependent molecular density n_a is equal to the Loschmidt number $n_0 \approx 2.67 \cdot 10^{25}$ [m^{-3}] for room temperature, and is inversely proportional to the temperature by the ideal gas law. The thermal velocity of electrons is conventionally equal to $v_{th,el} = \sqrt{(8k_BT)/(\pi m_e)}$ [11, (3.4)] with electron mass m_e and Boltzmann constant k_B, but it is approximated to $v_{th,el} = \sqrt{k_BT/m_e}$ yielding $v_0 = v_{th,el}(300\text{ K}) \approx 6.74 \cdot 10^4$ [m/s]. [§] The cross-sectional area of a helium molecule equals $< \sigma_a > \approx 6 \cdot 10^{-20}$ [m^2], and is averaged over the relevant range of temperatures.

It is convenient to calculate values of γ (rounded as 0.5 resp. 0.05 multiple), from (1.40) for half order of magnitude temperatures, and for the two

[§]The implemented thermal velocity is reduced by a factor $\sqrt{\frac{1}{2}}$ and $\sqrt{\frac{\pi}{8}}$ with respect to [13, (4.24)] resp. [11, (3.4)]. This might be an error, and it might explain why the future characterization of the plasma alludes to the requirement of higher γ. This possible error was identified too late to amend.

measurement frequencies $f = 2.45$ GHz and $\tilde{f} = 57$ GHz. These values are given in Table 1.3.

T	300 K	1000 K	3000 K
γ	6.5	4.0	2.5
$\tilde{\gamma}$	0.3	0.2	0.1

Table 1.3

Opacity

When covering magnetic induction, the real-valued conductivity of the plasma will be a more useful parameter to describe the plasma. In order to incorporate its imaginary part, this is converted to real relative permittivity. This is gives the two degrees of freedom in terms of two real-valued parameters, and is useful when implementing conductivity in simulations.

$$\epsilon_r' = 1 - \frac{\eta}{1+\gamma^2} \tag{1.41a}$$

$$\sigma = \omega\epsilon_0 \frac{\eta\gamma}{1+\gamma^2} = \omega\epsilon_0\epsilon_r'' \tag{1.41b}$$

1.4 Electromagnetic power absorption

This section gives the theory needed to explain why heating the LI-plasma sample at the microwave E-field does not work, and why heating it at the B-field is more successful. Parts of the paper will later refer to the theory introduced here. However, in order to provide simplified equations, order of magnitude estimates for the properties of the LI-plasma (to be found independently later on) are used. Using these order of magnitude properties, we can simplify the equations. The properties apply for time $t \in [30, 60]$ us. As for the geometry of the LI-torus, $a \approx \frac{r}{3}$, and for the inner cylinder we thus have $R < \frac{1}{2} \cdot \mathcal{R}$, with both r and a in the millimeter range.[¶] As for the material properties of the LI-torus, the conductivity of components lies within the range $\sigma \in [0.01, 100]$ S/m.

The fundamental equation for the total power absorption of a sample with volume V_s, conductivity σ and induced current J is given in (1.42).

[¶]Please refer to the appendix on toroidal coordinates for the meaning of the parameters.

$$P(\sigma) = \iiint_{V_s} \frac{J^2}{\sigma} d\tau = 2\pi \int_{\theta=0}^{2\pi} \int_{\rho=0}^{a} \frac{(J(\rho, \phi, \sigma))^2}{\sigma} \cdot (r + \rho \cdot \cos\phi)\, d\rho\, d\phi \tag{1.42}$$

The specific form of the equation for the plasma heating in our setups is also given in (1.42). Both the LP and EC can be described by the topology of a torus or a ring. The symmetric axis of the geometry is always chosen parallel to the field, such that it's parallel to E in the rectangular TE-101 cavity, and parallel to B in the rectangular TE-102- and cylindrical TE-011 cavity. This implies that the induced current density is constant over $\hat{\theta}$, which can thus be resolved as a factor 2π in front of the integral.

1.4.1 Electric power absorption: capacitive heating

The previous heating setup used **capacitive heating**, where a conducting sample (LI-plasma) is placed **at the location of the cavity with an oscillating electric field**. The electric field at some point of the conductor exerts a force on the (opposite and negative) charges, displacing them. This induced current density J aims to cancel the external field strength E_0 entering the region. Upon entry, the (transmitted) electric field strength will attenuate as it propagates further into the sample entry-boundary of the sample. This field attenuation is zero in the absence of charges ($\eta \to 0 \sim \sigma \to 0$), but becomes very steep for $\sigma \to \infty$. The field attenuation goes exponentially over distance from the boundary, with the field dying down a factor e^{-1} each skin depth δ into the sample. This skin depth follows the formula (1.43), where σ can be determined from the plasma properties η and γ by substitution of (1.41b) into [13, (1.30) and (1.33)].

$$\delta(\sigma) = \sqrt{\frac{2}{\omega\mu_0\sigma}} \cdot \sqrt{\sqrt{1 + \frac{\omega\epsilon_0}{\sigma}} + \frac{\omega\epsilon_0}{\sigma}} \tag{1.43}$$

In order for calculations of the total RF power absorption into the plasma by an oscillating electric field, it is convenient to introduce the distance z from the outer boundary of the plasma. By the fact that the LP-torus is axisymmetric with the electric field and the E-field boundary condition (1.4), the induced current density is concentrated at parts of the boundary that are parallel to the electric field. The induced current density is thus mostly situated at the surfaces closest to the axis ($R \approx r - a$), and farthest away from it ($R \approx r + a$). Integrating both boundaries over θ yields that the latter part accounts for most of the torus volume by its larger axial

radius. Moreover, assuming homogeneous conductivity, the total induced current at the inner section is proportional to that in the outer section, such that accounting for the outer section alone will provide the correct order of magnitude of the total induced current. We will therefore only account for induced current density near $z = (r + a) - R \approx 0$, and we simplify the integration over the torus cross-section by (very roughly) approximating the circular toroidal cross-section of radius a as a square cross-section of a ring of side-lengths $2 \cdot a$ and cross-sectional center radius r. This conversion from torus to ring shape is justified as follows. Imagining the torus semi-circular cross-section with $R > r$ and with effective volume power absorption at $r + a - \frac{\delta}{2} \leq R \leq r + a$. At each ϕ, multiplying the effective thickness $\frac{\delta}{2} \cdot \frac{1}{\sin\phi}$ by the share of parallel boundary-components $\sin\phi$, gives constant effective power absorption over $\hat{z}$ into a thickness $\frac{\delta}{2}$, with $R \in [r, r + a]$. Since for $\phi \in [0, \pi]$, the effective radius of the absorbing components lies mostly around $R \approx r + a \cdot \sin\frac{1}{2}\pi = r + a$. Therefore for small skin depth δ, the effective volume along the torus-boundary with $\phi \in [0, \pi]$ is thus approximately equal to the effective volume of a ring-shape with $R \approx r + a$.

By Ohm's law, $J(z) = \frac{E(z)}{\sigma}$. Therefore, for the power absorption integral over the (transmitted) Electric field inside a good conductor, where $\delta(\sigma) << a$, yields:

$$P_{tot}(\sigma) \propto \int_{z=0}^{z=2\cdot a} \exp\left(\frac{-2z}{\delta(\sigma)}\right) \approx \frac{\delta(\sigma)}{2}$$

This means that, for a good conductor $\sigma >> \epsilon_0\omega$, the integral over thickness z for an electric field decaying e^{-2} each δ, is equivalent to the non-decaying electric field times the thickness $\delta/2$. This in turn implies that the (transmitted) field is limited to an effective fractional volume henceforth called $G(\sigma)$, where $G = 1$ for full field penetration and $G = 5 \cdot \delta/2$ for the high conductivity limit.

$$G(\sigma, r, a) \equiv \frac{\iiint_{V_s} \exp -2z/\delta(\sigma) d\tau}{\iiint_{V_s} 1 d\tau} \tag{1.44}$$

The author leaves it to the reader to verify that for a ring as described above with $(r, a) \approx (3.75, 1.58)$ [mm,mm], the effective fractional volume G for σ (under $\gamma \approx 6.5$) over the range ${}^{10}\log\eta \in [-2, 3]$ yields (1.46b).

Aside from being a good approximation in the good-conductor limit, this expression also illustrates that the skin depth alone does not explain

reduced power absorption in good conductors. Namely, for good conductors $\sigma \approx \sqrt{\frac{2}{\omega\mu_0\sigma}}$, such that power absorption diverges under increasing conductivity.

$$P_{tot}(\sigma) \approx 2\pi(r+a)\cdot(2a)\frac{1}{2}\cdot\sqrt{\frac{2}{\omega\mu_0\sigma}}\cdot\sigma \propto \sqrt{\sigma}$$

Accounting for the skin depth field reduction only, power absorption would diverge for infinite conductivity; the reduced RF-power absorption for good conductors under capacitive heating is thus not fully described by the skin depth. In reality, the external field is attenuated upon transmission across the boundary interface of the homogeneous plasma. According to boundary conditions given in [4, 2.9], the complex transmission ratio T, equal to transmitted field E_t over external field E_0 is given by:

$$T \equiv \frac{2Z_m}{Z_m + Z_0},\ Z_m \equiv Z_0 \cdot \left(\epsilon_r'(\sigma,\gamma) - i\cdot\frac{\sigma}{\epsilon_0\cdot\omega}\right)^{-1} \tag{1.45}$$

The transmitted power is therefore the absolute value squared of this transmission coefficient. In terms of the plasma parameters η and γ one can substitute with (1.41b) and (1.39a) to obtain the approximate equation (1.46c).[||]

The approximate total capacitive power absorption P_c into the toroidal plasma can be computed from the volume V_s, minor radius a, material properties (η,γ), with corresponding conductivity σ by (1.41b). By Ohm's law, the integrand becomes $\sigma\cdot|E(z)|^2$, where the depth-dependent squared field magnitude $|E(z)|^2$ can be postulated in terms of the above approximations for G and $|T|^2$. The volume integral over $|E(z)|^2$ can be substituted as a product of effective field and effective volume: (i) the transmitted "un-decayed" squared field amplitude $(E_0^2\cdot T^2)$, and (ii) the sample volume times the effective fractional volume $(V_s\cdot G)$. The full product yields the equation (1.46a), which is given in terms of the simplified torus-/ring-shape approximations (1.46c) and (1.46b).

***Capacitive* total power absorption P_c for a toroidal sample with minor radius a and volume V_s, normalized electron density η, normalized collision frequency γ, corresponding conductivity σ by** (1.41b)**,**

[||] This means that for $\eta \approx \gamma \approx 1$, the transmission can be greater than one, which seems erroneous. Usually, the issue is masked by the exponential nature involved, but became an issue that at the cutoff transition around these same values, Δf exceeded (1.26a).

Version of July 8, 2021– Created July 8, 2021 - 13:14

at an electric field strength E_0 with angular oscillation frequency ω.

$$P_c(\eta,\gamma) = \sigma \cdot (E_0^2 \cdot |T|^2(\eta,\gamma)) \cdot (V_s \cdot G(\sigma)) \tag{1.46a}$$

$$G(\sigma) = \frac{1}{8\pi r a^2} \int_{z=0}^{2a} 4\pi a(r+a-z) \exp\frac{-2z}{\delta} dz \approx \frac{1}{1+\frac{2.5a}{\delta(\sigma)}} \tag{1.46b}$$

$$|T|^2(\eta,\gamma) \approx \frac{4}{4+\frac{\eta^2-4\cdot\eta}{1+\gamma^2}} \tag{1.46c}$$

$$\sigma(\eta,\gamma) = \epsilon_0 \omega \eta \gamma / (1+\gamma^2)$$

The volumetric approximation used to obtain equation (1.46a) means that it will only apply to the sample if it is toroidally- / ring-shaped. As we will see from analysis of IAT-CCD images of the two components, both LP and EC identify as such shapes. There are limits to the accuracy of the equation, however. Firstly, its derivation relied on the assumption that they are material properties are homogeneous, which will be refuted by CCD-image analysis of the LP cross-section. Secondly, the equation for the EC is different from (1.46a) when the nearby LP is beyond cutoff, thus altering the field strength within the EC-volume. The field amplitude E_0 near the EC may be negated or be amplified by up to a factor two: $E_0^{(EC)} = 2 \cdot E_0$, making the EC-power absorption $P_c^{(EC)}$ some coefficient times (1.46a). Evidence for field amplification will be addressed near Figure 2.5a later on, along with an estimate of the amplification value.

1.4.2 Magnetic power absorption: inductive heating

Whereas capacitive heating favours the resistive EC over the conductive LP, magnetic induction will reverse these roles. The theory in this section will be focused on magnetic induction heating of the plasma (a.k.a inductive heating), where the symmetric axis is parallel to the magnetic field. By Faraday's law of induction, a loop shaped conductor catching flux of an oscillating magnetic field will have current induced within it. From the conductivity of a material and the known field near it, we can predict the amount of induced current. This can then be used to deduce the power absorption into the loop.

There are two limits to the power absorption of a loop in a time-varying magnetic field over sigma. For the limit sigma to zero, the loop acts like free space, because there won't be any charges present in the loop to respond to the magnetic field oscillation. For the limit sigma to infinity, the

Version of July 8, 2021– Created July 8, 2021 - 13:14

loop acts like a superconductor, meaning that the induced currents do not feel any resistance and therefore no power can be absorbed. We know, however, from real life experience that power is absorbed for conductivities in between these limits. Therefore, by Roll's theorem there must be some optimal conductivity σ_{opt} for which this absorbed power is maximized, which we will aim to determine.

The induced current within the loop induces an eddy field $\mathbf{B_e}$ that cancels the external field $\mathbf{B_0}$.

Induced current density in sample, from sample conductivity, field strength, and oscillation frequency

To deduce the induced current density within a torus placed in an oscillating magnetic field, we use the formulae for excitation of an infinitely long cylinder, as found by [14]. There are two formulae based on the two possible orientations of a cylinder with respect to the magnetic field direction. If the symmetric axis of the cylinder is parallel to the magnetic field, we speak of longitudinal excitation. If its symmetric axis is perpendicular to the field lines, we speak of transverse excitation.

$$\mathbf{J_l}(R,\sigma) = \frac{k(\sigma)B_0}{\mu_0} \cdot \frac{J_1(k(\sigma) * R)}{J_0(k(\sigma)\cdot\mathcal{R})}\hat{\theta},\ (0 \le R < \mathcal{R}) \tag{1.47a}$$

$$\mathbf{J_t}(\rho,\sigma) = \frac{-2i\omega\sigma B_0 a}{k(\sigma)aJ_1'(k(\sigma)\cdot a) + J_1(k(\sigma)\cdot a)} \cdot J_1(k(\sigma)\cdot\rho)\cdot\sin\phi\cdot\hat{\theta} \tag{1.47b}$$

$$(0 \le \rho < a),\ (0 \le \phi < 2\pi)$$

Where $J_1' \equiv \frac{dJ_1}{d\rho}$. Here, $k(\sigma) = \sqrt{(\frac{1}{2})}(1-i)\sqrt{(\omega_0\sigma\mu_0)}$ with ω_0 the angular resonant frequency. The constants involved are B_0 the magnetic field strength near the torus in cases of empty cavity resonance, μ_0 the vacuum permeability, and r and a the major respectively the minor radius of the torus. J_0 and J_1 are the zeroth respectively first order Bessel functions of the first kind. The induced current density is given for the longitudinal and transverse orientations, represented by subscripts l and t respectively. Under longitudinal excitation, the cylinder's symmetric axis is parallel to the $\mathbf{B}$, while under transverse excitation the symmetric axis is perpendicular to $\mathbf{B}$.

The formulae for the two types of induction for a cylinder can be combined to compute the total magnetic induction for a torus. For the ultimate purpose of the determining the total absorbed power under an oscillating

magnetic field, we will argue that the absorbed power into our LI-torus (r, a, σ) can be approximated as a volume integral of the longitudinal induced current density J_l over a toroidal sub-domain of the infinite cylinder. If the torus is axisymmetric with the magnetic field lines, then the induced current density within the torus is roughly the summation of longitudinal and transverse excitation for an infinite cylinder, as will now be justified. We will do so by making two topological adjustments to an infinite cylinder of radius $\mathcal{R} = r + a$ (axisymmetric to the magnetic field) that turn it into a torus with major/minor radius (r, a). **Starting with the initial state of an infinitely long cylinder axisymmetric with B**, this has only longitudinal excitation. With each topological adjustment, we argue why the solution for the longitudinal induced current density is retained.

Step 1: we cut away the inner cylindrical sub-domain with $R < r - a$, leaving a tube-shape with $r - a \leq R < r + a$. We will find the LI-torus to have roughly $a \approx \frac{r}{3}$, and for the inner cylinder we thus have $R < \frac{1}{2} \cdot \mathcal{R}$, with both r and a in the millimeter range.

Firstly, the perturbation of the induced current density at $R = r - a$ can be ignored. Considering the much smaller induced current density towards the center in (1.47a), $J_l(R) << J_l(\mathcal{R})$.

Secondly, the (see appendix on torus cross-section) total volume power absorption is also much lower. Namely, integration yields that the inner cylinder volume $0 < R < \frac{1}{2}\mathcal{R}$ is much smaller than the outer tube-like volume $\frac{1}{2}\mathcal{R} < R < \mathcal{R}$.

The solution for the total power absorption into an infinitely long tube is thus similar to the solution for the infinitely long cylinder.

Step 2: we cut out and retain a circular cross-section of this infinitely long tube that is perpendicular to $\hat{\theta}$ and has cross-sectional radius a concentric with the point $R = r$ away from the tube axis. We are now left with a torus-shape with major/minor radius (r, a). We will now formalize the influence on the original induced current density solution $J_l(R) = J_l(\rho \cdot \phi)$ in terms of the toroidal coordinates defined in the appendix. Consider any point on the boundary of the toroidal cross-section: this has perpendicular unitary normal vector $\hat{n}$ in terms of cylindrical coordinates: $\hat{n} = x \cdot \hat{R} + \sqrt{1 - x^2} \cdot \hat{h}$, with $x \in [0, 1]$. At local coordinates $\hat{n} \approx \hat{R} \rightarrow x \approx 1$, the torus geometry is locally equivalent to the tube-geometry, and the induced current density remains unchanged.

At local coordinates $\hat{n} = \hat{h} \rightarrow x \approx 0$, however, the solution changes. By the boundary condition for the magnetic field given in (1.4), the magnetic

field should locally be cancelled, requiring the introduction of a transverse induced current density at $x \approx 0$. The solutions for the transverse induced current density of a torus with minor radius a is equal to the solution for the transverse excitation of an infinite cylinder with radius a. [**] This distribution is given in (1.47b). We will later find the LI-torus to have conductivity $\sigma \in [0.01, 100]$ S/m.

Firstly, the range of conductivities gives the transverse excitation J_t to have a much smaller order of magnitude than J_l within the toroidal slice. By Ampere's law for eddy currents, $\nabla \times \mathbf{B_e} = \mu_0 \mathbf{J} \rightarrow \frac{\partial B_e}{\partial h} = \mu_0 J$, both currents simultaneously cancel the incoming field B_0 through induction currents. Taking the ratio of coefficients for both solutions (1.47a) and (1.47b) therefore reflects the dominant induced current density field solutions. It provides us with the familiar skin depth δ over the torus minor radius a:

$$\frac{|J_l|}{|J_t|} = \frac{\sqrt{\omega\mu_0}B_0}{\sqrt{\mu_0}} \cdot \frac{1}{\omega\sigma a B_0} = \frac{1}{\sqrt{2}}\frac{\delta}{a}$$

The skin depth under the range of conductivities takes the values $\delta \in [1, 100]$ [mm]. Under $a \approx 1$ [mm], this indicates that the ratio of the longitudinal induced current density coefficient is mostly of a higher order of magnitude than the transverse induced current density over the range of conductivities. We will

Therefore, theoretical computation of the induced current density from magnetic induction for $\sigma < 100$ S/m into a torus with (r, a) will be approximated as equal to the absolute longitudinal induced current density J_l for radius $\mathcal{R} = r + a$. We substitute axial radius in terms of toroidal cross-sectional coordinates $R = \rho \cdot \sin\phi + r$ with $(0 \leq \rho \leq a)$, $(0 \leq \phi \leq 2\pi)$, and we take the absolute value $J = |\mathbf{J}|$ to determine (1.48a). The total inductive power absorption P_i corresponding to the induced current density in (1.48a) can be found by substitution of J in (1.42). Integrating of the cross-sectional distribution over the torus volume yields (1.48b).

***Inductive* induced current density magnitude J_i and corresponding total power absorption P_i for a toroidal sample with major/minor radius (r, a) and conductivity σ, at a magnetic field strength B_0 with angular oscillation frequency ω.**

$$J_i(\rho, \phi, \sigma) = B_0\sqrt{\frac{\omega\sigma}{\mu_0}} \cdot \frac{J_1(k(\sigma)(\rho\sin\phi + r))}{J_0(k(\sigma)(\rho\sin\phi + r))} \tag{1.48a}$$

[**] By the argument that the torus is a cylinder that bites itself in the tail.

Version of July 8, 2021– Created July 8, 2021 - 13:14

$$P_i(\sigma) = \iiint_V \frac{J_i^2}{\sigma} d\tau = 2\pi \int_{\phi=0}^{2\pi} \int_{\rho=0}^{a} \frac{(J_i(\rho,\phi,\sigma))^2}{\sigma} \cdot (r + \rho \cdot \cos\phi)\ d\rho\ d\phi \tag{1.48b}$$

Where the cross-section of the torus follows a circle with radius a, concentric with a distance r from the symmetric axis. No further approximations will be made here, and future evaluations of the integration will be implemented numerically in *Python*.

1.4.3 CPT-effects from absorbing plasma

In this subsection, we give additional miscellaneous theory. Firstly, formulae are deduced for the **empty cavity-**field amplitudes E_0 and B_0 needed to determine the (non-renormalized) capacitive resp. inductive power absorption. Afterwards, we will give a strategy for the determination of the cavity characteristics - the quality factor Q and the resonant frequency shift Δf - in order to test the validity of the power absorption theory to experimental data and simulation data. Here, the quality factor Q is computed on the basis of a required renormalization of the cavity field amplitude under absorption by the plasma. Also, the resonance frequency shift Δf from the plasma with complex permittivity $\epsilon' + \epsilon''$ is determined from the sum of upward- (ϵ') and downward ($G(\sigma) \cdot T^2(\sigma)$) frequency shift.

Magnetic field strength B_0

We will determine the approximate electric- and magnetic field strengths E_0 and B_0 inside a cavity. Field strength within the cavity can be determined from the cavity's RF-properties Q and f_0, the energy density distribution of the field, and lastly the input power of the RF-signal P_{in}. By definition, at resonance, the quality factor equals the frequency times the cavity energy divided by the power loss [15]:

$$Q \equiv \omega_0 \frac{U_0}{P_l} \tag{1.49}$$

For the case of the matched and tuned empty cavity, all input power ends up in the cavity walls. Therefore, the power loss equals the power input and we can state for the total empty cavity field energy:

$$U_0 = \frac{P_{in} \cdot Q}{\omega_0}$$

Since the total energy contained in the cavity U_0 is half magnetic and half electric by [4, p. 503], the value for the total magnetic energy density is $U_m = U_0/2$. [††]

By integration of the magnetic field distribution given in (1.27), we deduce that:

$$\iiint_{V_0} |B|^2 d\tau = \frac{1}{\chi_B} \cdot B_0^2 \cdot V_0 = \frac{B_0^2 \cdot V_0}{2}$$

The magnetic field energy density u_m is given by [16]:

$$u_m = \frac{1}{2}\frac{B_0^2}{\mu_0}$$

Integration over the total cavity volume in combination with the field equations in (1.27b):

$$U_m = \frac{1}{2 \cdot \mu_0} \iiint_{V_0} |B|^2 d\tau = \frac{1}{4 \cdot \mu_0} B_0^2 \cdot V_0$$

Finally, we can thus determine the equations for the non-time-averaged magnetic field amplitude B_0 and the associated electric field amplitude E_0 by [17, (32.4)] in (1.50).

$$B_0 = \sqrt{\frac{\chi_B \mu_0}{\omega_0}} \cdot \sqrt{\frac{P_{in} \cdot Q}{V_0}},\ E_0 \approx c \cdot B_0 \tag{1.50}$$

Renormalization of field amplitude under absorption

The field amplitudes B_0 and E_0 given by (1.50) determine the power absorption in the plasma computed through (1.46a) and (1.48b). As we will see for properties V_s, η, and γ of the LI-plasma, the power absorption determined under the empty cavity field amplitudes may exceed the input power. This is obviously impossible, and we therefore require a correction that lowers the field amplitude based on the power absorption into plasma such that the sum of power loss, both into cavity walls P_{cav} and into plasma P_{pl}, equals the input power.*

[††]Moreover, the magnetic mode within the cavity is an oscillating field, which implies that the associated energy must have deviant time averaged value. However, this required time-average correction will not be explored, because the author found too much ambiguity in the literature providing the equations.

*This inherently implies that we ignore CPT-tuning and -matching effects from the plasma.

Version of July 8, 2021– Created July 8, 2021 - 13:14

Requirement: $P_{in} = P_{cav} + P_{pl} = P_l$

To keep our calculations on power absorption straightforward, we will not alter the equations (1.48b) and (1.46a) for the new field, because there is a danger of introducing a recursiveness. Rather, the power absorption is computed under the empty-cavity magnetic field strength and calibrated a posteriori to determine power absorption under constant P_{in} into the cavity. This calibration can be intuitively determined from the new total quality factor Q' of the cavity containing the absorbing plasma, which is decreased w.r.t. Q_0. For the empty-cavity field amplitudes B_0 with respect to decreased field B', the corresponding plasma power losses are $P_{pl}^{(0)}$ resp. P'_{pl}. By the proportionality of field energy density and quality factor $B^2 \propto Q$:

$$P'_{pl} = \frac{Q'}{Q_0} \cdot P_{pl}^{(0)}$$

By the proportionality of total power loss and quality factor:

$$Q' = \frac{Q_0 \cdot P_{in}}{P_{in} + P_{pl}^{(0)}}$$

Renormalizing the uncalibrated power absorption $P_{pl}^{(0)}$ to the calibrated power absorption P'_{pl} is done simply by the following multiplication:

$$P'_{pl} = P_{in} \frac{1}{1 + \frac{P_{in}}{P_{pl}^{(0)}}} \tag{1.51}$$

Theoretical determination of total cavity quality factor and resonance frequency shift from composite plasma properties

The theory expansions of effective fractional volume and the amplitude transmission into a homogeneous plasma will allow us to rough estimates of the properties of both LP and EC from measurement data of f_0 and Q. Formulae thus far given only apply to plasma well below cutoff (1.26a) and (1.26b) or plasma well beyond cutoff (1.33a). Measurement data on the plasma (to be given in Figure 2.2a) will be over a time domain where the plasma decays from being well beyond cutoff to well below cutoff. In order to determine the properties of the plasma over the entire time range,

it is paramount that we determine formulae for Δf and Q that reliably describe the transition in order to cover the full time range.

If a sample is well beyond cutoff, this means that field energy density is severely reduced within the sample domain. If a sample is well below cutoff, this means that the field energy density is equal to the empty cavity field energy density. In terms of CPT, these two extremes correspond to the two extremes of the numerator expression in (1.24). The volume integral over a sample beyond cutoff equals zero, whereas the integral for a sample well below cutoff equals the local squared electric field amplitude times the sample volume. Upon transmission through the sample volume boundary, the field is attenuated a factor $|T|^2$ and on average such amplitude is occupied over an effective sample volume of $G \cdot V_s$. This yields the transition equation:

$$\iiint_{V_s} |E|^2 d\tau \approx V_s \cdot G(\sigma) \cdot |T|^2 \cdot E_0^2$$

This integral has already been reduced to the effective fractional volume $G(\sigma)$ in (1.46b) and the energy transmission coefficient $|T|^2$ in the section on capacitive power absorption, and the product of these two parameters provide a convenient function by which to provide a simple model of CPT around the cutoff transition ($G(\sigma) \cdot |T|^2 \approx 1/2$). The product of the effective fractional volume and field energy transmission coefficient are always found in unison, and together form the *effective fractional energy* H within the sample with respect to the case of its absence, the equation of which is given in (1.52d). Here, $H = 0$ represents a sample well beyond cutoff, with $H = 1$ well below cutoff.

We can now postulate full formulae for the quality factor and resonant frequency shift of the total cavity under the presence of plasma at the E-field antinode.

The resonance frequency is the sum of the upward frequency shift from $\Delta\epsilon_r' < 0$ in (1.26a) and the downward frequency shift from field negation across V_s in (1.33a). Adding the two shifts together, we reach the expression for the total frequency shift due to a sample, as given in (1.52a).

The LI-plasma consists of two sample components, both with (very) roughly homogeneous properties of η and γ and separate sample volumes V_s. The total frequency shift measured in Figure 2.2a is the sum of the total frequency shift from the two samples LP and EC simultaneously. This sum rule does not hold for the quality factor. Therefore, we involve the two sample components simultaneously when addressing the quality factor.

Version of July 8, 2021– Created July 8, 2021 - 13:14

The total quality factor under the presence of two samples *(1)* and *(2)* at the E-field antinode results from the rule for the total quality factor Q_{tot} $\frac{1}{Q_{tot}} = \frac{1}{Q_0} + \frac{1}{Q_1} + \frac{1}{Q_2}$, implying that the quality factor of the total system in terms of respective sample power absorption P_1 and P_2 is as given in (1.52b).

The power absorption is given by a simplified version of (1.46a) that also allows for a field-amplitude amplification due to presence of nearby objects beyond cutoff, accounted for if $\alpha = 2$ and not if $\alpha = 1$, with $\alpha \in \{1,2\}$. This expression is nearly equivalent to only $\alpha \in \{1\}$, but is repeated along with the quality factor for good measure in (1.52c). This model thus assumes sample *(1)* to be beyond cutoff if sample *(2)* gives significant power absorption.†

Total frequency shift and quality factor of a TE_{101} cavity containing samples $\alpha \in \{1,2\}$ (read: LP resp EC) with normalized electron density η_α, normalized collision frequency γ_α, corresponding conductivity σ in (1.41b)**, and sample volume V_α.**

$$\Delta f_{tot} = \sum_{\alpha=1}^{2} -\frac{\chi_E}{2} \cdot \frac{V_\alpha}{V_0} \cdot f_0 \cdot \left(-H(\eta_\alpha, \gamma_\alpha) \cdot \frac{\eta_\alpha}{1+\gamma_\alpha^2} + \frac{1 - H(\eta_\alpha, \gamma_\alpha)}{x} \right) \tag{1.52a}$$

$$Q_{tot} = P_{in} \cdot \frac{Q_0}{P_{in} + \sum_{\alpha=1}^{2} P(\eta_\alpha, \gamma_\alpha, V_\alpha)_\alpha} \tag{1.52b}$$

$$P(\eta, \gamma, V_s)_\alpha = |E_0|^2 \cdot V_s \cdot \sigma(\eta, \gamma) \cdot 2^{\alpha-1} \cdot H(\eta, \gamma) \tag{1.52c}$$

$$H(\eta, \gamma) \equiv \frac{\iiint_{V_s} |E|^2 d\tau}{V_s \cdot |E_0|^2} = G(\sigma(\eta, \gamma)) \cdot |T|^2(\eta, \gamma) \tag{1.52d}$$

1.5 Thermodynamics

1.5.1 Boltzmann-normalized Saha equation

The electron density associated with the plasma's gas temperature can be determined with the Saha-equation (1.53a), where n_i, g_i, and ϵ_i are respectively the particle density, degeneracy, and energy potential of the

†The relevance of this relation will become evident from Figure 2.5a, where this relation of samples *(1)* and *(2)* is equivalent to how LP and EC relate under simultaneous decay.

Version of July 8, 2021– Created July 8, 2021 - 13:14

i-th ionization level, and λ_e is the electronic de Broglie wavelength as expressed in (1.53b). Assuming the helium plasma to be singly-ionized, we need only consider the case $i = 0$, with associated values $g_1 = 2$, $g_0 = 1$, $\epsilon_1 = U_{ioniz}$, $\epsilon_0 = 0$. Additionally, assumption of quasi-neutrality yields ion density equal to electron density $n_i = n_e$, and assumption of low ionization grade ($n_e \ll n_0$) yields $n_{i=0} = n_0 - n_e \approx n_0$ the number density $n_{i=0}$ of ground state particles roughly equals that of neutral particles n_0. Lastly, the reduction in the number density of gas particles due to increased temperature is accounted for using the ideal gas law: $n_0(T) = n_0(T = 300[\text{K}]) \cdot (300[\text{K}])/T$. The combination of the above assumptions and correction yields the terms after the arrow in (1.53a), with n_e isolated at LHS.

Evidently, the electronic De Broglie wavelength depends on the electron temperature T_e, whereas the gas density (n) and ionization grade ($\chi \propto \exp \frac{-U_{ioniz}}{k_B T}$) depend on the gas temperature T_g. The electron temperature is usually higher than the gas temperature, because the RF-absorption accelerates the light electrons ($m_e = 9.11 \cdot 10^{-31}$ [kg]) to greater magnitude than the heavier gas atoms ($m_i = 1.34 \cdot 10^{-26}$ [kg]), where the electrons in turn raise the gas temperature through collisions with rate ν_{en}. However, the electron- and gas temperatures are assumed to be equal due to the more dominant temperature-dependence of remaining terms in the equation with respect to the factor $(T_e/T_g)^{3/4}$.

Naively evaluating (1.53a) for $\eta = 1 \sim n_e = n_c$ yields the plot in [18, Figure 5.5]; a higher-than expected gas temperature $T_g \approx 6500$ [K], which is much larger than measured- [19, Figure 5.9] and simulated [18, Figure 4.9] gas temperatures.

The resolution to this overestimate of the gas temperature is to acknowledge the unequal temperature distribution of gas particles. The distribution of the amount of particles with some particular temperature T near the global system temperature T_0 follows the Maxwell-Boltzmann distribution, the probability density function $P(T')_T$ of which is formalized in (1.53c). Consequently, the actual value of the electron density associated with the average temperature T is an integral over all temperatures with the integrand the product of (1.53a) and (1.53c). This normalized electron density by (1.53d) yields for **plasma-stability** with $n_e \approx n_c$ a **corresponding gas temperature $\mathbf{T_g} \approx$ 1000 [K]**.

$$\frac{n_{i+1}^2}{n_i} = \frac{2}{\lambda_e^3}\frac{g_{i+1}}{g_i}\exp\left(-\frac{\epsilon_{i+1}-\epsilon_i}{k_B T}\right) \rightarrow n_e(T_g) = 2 \cdot \sqrt{\frac{n_0}{\lambda_e(T_g)^3} \cdot \frac{300[\text{K}]}{T_g} \cdot \exp\left(\frac{-U_{ioniz}}{k_B T_g}\right)} \tag{1.53a}$$

$$\lambda_e(T) = \sqrt{\frac{h^2}{2\pi m_e k_B T}} \tag{1.53b}$$

$$f_T(T, T_0) = 4\pi \cdot (\frac{m_i}{2\pi k_B T_0})^(3/2) \cdot v(T)^2 \cdot \exp{(\frac{-m_i \cdot v(T)^2}{2k_B T_0})}, v(T) = \sqrt{\frac{2k_B T}{m_i}} \tag{1.53c}$$

$$\eta(T) = \int_{T=0}^{\infty} f_T(T, T_0) dT \frac{dv}{dT} \frac{n_e(T)}{n_c} \tag{1.53d}$$

$$^{10}\log{(\eta(T))} = p_0 - \exp{(p_1 + p_2 \cdot T)} + p_3 \cdot \sin(\frac{T}{p_4})$$

$$p_{i\in[0,5]} = \{3.49, 2.33, -1.01e-3, -3.44, -7.25e3\}$$

1.5.2 Heat conduction power loss of the plasma

The heat transfer coefficient of Helium is $k \approx 1$ [W $\cdot$ m^{-1} $\cdot$ K^{-1}] with corresponding conduction power loss given in (1.54).

$$P_l^{(c)} = \dot{Q} = k \cdot A \cdot \nabla T \tag{1.54}$$

Chapter 2

Experimental setup and measurements on setup

2.1 System overview

This subsection will provide a full walk-through of the 2.45 GHz capacitive heating setup, which also facilitates measurements on the LI-plasma through **CCD images** and **frequency-dependent power reflection** measurements. Independently, another setup has been used for measurements at 57 GHz frequency, and these have yielded **transmission** measurements. The heating setup will be walked through from front to back in 3 sections. Then the laser creating the plasma is addressed. Finally, the setup facilitating 57 GHz measurements is outlined. This subsection's categorization of the system overview is illustrated in Figure 2.1 below.

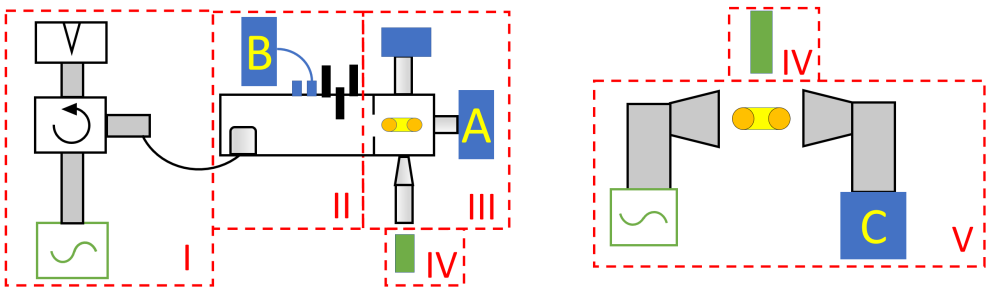

(a) *2.45 GHz setup idealized* ***(b)*** *57 GHz setup idealized*

Figure 2.1: *Measurement setups, conducting components in black, active components in green, measurement components in blue. Created using Powerpoint*

I: Heating source

The setup is being heated by a magnetron operating at a frequency of $f_{mag} = 2.46895$ GHz ≈ 2.469 GHz. The goal for cavity tuning is therefore to make sure that the cavity resonance frequency f_0 equals the magnetron frequency f_{mag}. The signal exits the magnetron through a WR-340 waveguide.

Apart from the requirement of tuning, the cavity also needs to be matched to the waveguide. If this is not the case, some power is reflected by the cavity, back into the waveguide and thereafter possibly the heating system. Any signal leaking back into the source can be damaging. In order to deviate this reflected power away from the magnetron, a circulator is placed between the magnetron and the waveguide. A circulator is a three port network that 'circularly' transmits power among the three ports, that is: power from port 1 to port 2, from port 2 to port 3, and from port 3 to port 1. In analogy with our setup, the power originating from the magnetron is transmitted to the waveguide, and power reflected by the waveguide is transmitted to the third port of the circulator.

Once the signal has gone from the magnetron, through the circulator, to the first waveguide, the signal is converted from a rectangular mode to a coaxial mode.

II: Waveguide components

The plasma is supposed to be contained and heated in cavity at the back end of a custom 90×40 mm^2 waveguide. This waveguide has been encased in a vacuum chamber, which will be repeatedly drained of air and filled with helium gas to ensure adequate purification. The magnetron signal enters this final waveguide as a coaxial mode at its front end. This coaxial mode is converted by a mushroom-shaped antenna at $\lambda_g/4$ distance from the front waveguide end into a rectangular mode of the waveguide, with geometry given in [5, par. 4.2.1]. Along the waveguide walls, the forward and backward signals within the waveguide are measured by the forward and backward couplers respectively, [5, par. 4.2.2]. A coupler is implemented as a table-shaped conductor encased by a cylinder, that is placed along the depth of the waveguide, at the height of the waveguide walls. On either side along $\hat{z}$ of the table-shape, rods extend into the core and sheath of the coaxial cable connected to it. The RF signal induces a current in the table, which is then transferred to the coaxial cable with some attenuation with respect to the waveguide signal amplitude. Typically, such a coupler transmits -60 dB of the RF signal amplitude travelling

through the waveguide. Measurements on the forward coupler have been used to make 2.45 GHz measurements.

III: Cavity

Just before reaching the iris, the signal encounters an M14 stub ($r = 7$ mm, $h = 13.5$ mm) at $\lambda_g/4$ in front of the iris. This is the first of the two matching elements along with the iris. The signal then travels through a circular aperture called the iris, which has a radius $r = 10.5$ mm. The iris is placed at a distance $d \approx \lambda_g/2$ from the waveguide short at the back end, thus forming a rectangular TE_{101} mode. Tuning is accomplished by translating the position of the iris-plate within the waveguide, thus changing the cavity depth d respect to the short.

The cavity furthermore has three openings, all followed by tubes with similar inner radius, elongated axisymmetrically with the cavity holes. The tubes have a height of about ten times the radius of the hole, resulting in only -60 dB cavity power leakage from the outer end of the tubes. Two tubes are placed along the y-axis, at the centers of the upper and lower planes of the cavity (x=a/2, z=d/2). One tube contains a lens with a focal length of 50 mm, thus placed at 30 from the opening, creating a focus at the cavity center. At its outer end, this tube has a high-power laser to be discussed in the next subsection. The two remaining tubes contain a CCD camera at their outer end, one opposite the first tube, the other at the center of the short.

IV: Laser

The plasma is created by a laser-pulse originating from a type Nd:YAG laser, operating at a power of $P_{laser} = 20$ MW and a frequency of $f_{laser} =$ 1064 nm. For a full description of the setup of the laser, as well as the CCD-cameras please refer to [19]. The laser beam is focused into the center of the cavity by a lens with a focal length of $l = 50$ mm. The pulse duration is $\Delta t_{laser} = 16$ ns. The emitted power over time follows a Gaussian development, such that the effective time at which full power is emitted is only around 10 ns. The total pulse energy deposited by the laser was set to $U_0 = 275$mJ, which is an upper limit to the energy absorbed at the focus. Flow simulations [18] of the first 30 microseconds after laser-pulse reproduce the torus-formation measured through CCD images for an initial deposited energy of roughly $U_{init} = 42$ [mJ]. Because the deposition time $\Delta t \approx 16$ [ns] is much shorter than that of subsequent expansion $\Delta t = 10$ [us] (see Figure 3.5a), atmospheric, room-temperature

particle density may be assumed. CCD images of the plasma during at $t = 100$ [ns] after the laser-pulse [18, Figure 3.1] indicate deposition into a roughly cylindrical volume $V(t = 0) = 6.8$ [mm^3]. Substitution of $V(t = 0)$ and $U(t = 0)$ into the ideal gas law yields an initial temperature $T(t = 0) = \frac{2U(t=0)}{3n_0V(t=0)k_B} \approx 10^4$ [K], to be used later on.

V: 57 GHz measurement setup

Transmission measurements are made on the plasma midway in between two trapezoidal-shaped horns facing each other.[12] One horn is excited by a Gunn-oscillator operating at 57 GHz. At the end of the opposite horn, the transmitted signal is measured. Measurements on the plasma are then made by aligning the laser focus at the center of the domain between the horns. These measurements yield a phase shift and an attenuation of the transmitted signal with respect to the input signal. In simulations, these two degrees of freedom were then used to convert to the two degrees of freedom of the plasma: electron density and collision frequency. A parametric sweep was made of these properties to the plasma domain and the combination of properties that reproduced experimentally measured values would thus characterize the plasma. However, this method heavily relies on the right shape (r, a) and volume V_s of the plasma. For the remainder of this paper, 57 GHz will only be involved in simulations to fact check the final solutions for the characterization of the plasma.

2.2 Measurements on plasma

Previous experiments on the plasma have aimed to characterize the geometry, electron density, and collision frequency of its components. CCD measurement on the plasma have aimed to deduce the geometry of the plasma's components. As for the characterization of the plasma's material properties, two different measurements of the plasma have been made with different frequencies and setups. Both experiments study the same laser-induced plasma over a period of about 100 us since its inception. Both experiments approach such a measurement by creating a setup that is excited by some RF signal (input), measuring the reflected/transmitted signal (output calibration) in absence of plasma, and measuring this reflected/transmitted signal in the presence of plasma (uncalibrated output). Output signals in the presence of plasma are then calibrated by comparison with output signals in absence, to get the effects of the plasma proper. Finally, the plasma is characterized in terms of electron density

and collision frequency by either converting measurement values to plasma properties under theory, or by reproduction of measurement values under simulations.

A: CCD images

The next chapter will devote itself to an analysis of the plasma geometry and material properties of the plasma. This will be done by studying CCD images of the plasma. There are two types data sets of these images. One of the unperturbed evolution of the plasma - that is without RF - and one with RF heating on. As for the images, the raw images can be studied to give a raw side view of the plasma, and the Inverse Abel Transform (IAT) of said raw images which give the cross-section of the plasma by its axisymmetric property. Equivalently, multiplying the pixels in each row of the (IAT) by the distance from central row, reproduces the raw image. The downside to the IAT is that it creates a numerical instability at the symmetric axis - visible as unexpectedly high luminosity around the symmetric axis. * For this reason, the IAT is used only when the raw image would not give an accurate representation for the parameter to be deduced. This will be relevant when studying the LP major radius and the EC electron density distribution.

The iris-coupled heating setup used is sketched in Figure 2.1a with (near-constant) input power $P_{in} = 3$ [kW] active over time $t \in [20, 100]$ [us]. The (reduced) transmitted power (due to mismatch or mistune) is unknown, because of the inability to apply diagnostics under high input power. The plasma-filled cavity is matched with iris radius $r = 10.5$ [mm] and tuned to air-filled empty-cavity resonance frequency $f_{empty,Air} = f_{mag} - 5$ [MHz] in order to compensate for the deviant Helium-permittivity and the LI-plasma's downward frequency shift.

B: 2.45 GHz measurements

The LI-plasma is created by depositing the laser energy into a focus at the center of the cavity sustaining the TE_{101} mode at a frequency of 2.45 GHz, illustrated in figure 2.1a. The measurement method may be fully characterized as *Reflection coefficient spectrum measurements* and is explained in [5]. For multiple frequencies, each in a spectrum of frequencies around the empty cavity resonant frequency, the power reflection coefficient $|S_{11}|^2(f)$

*This is most likely due to the abel inverse working "outside-in" meaning that any leftover intensity upon reaching the axis (due to noise) is attributed to the pixels around there.

Version of July 8, 2021– Created July 8, 2021 - 13:14

is measured at said frequency over a time span $t \in [-3, 270]$ us relative to the laser pulse instant $t = 0$ us. The empty cavity is matched and tuned to a frequency of $f \approx 2.448$GHz. The measurements consist of a multitude of separate measurements over a range of frequencies near $f \in [2.4, 2.46]$ GHz, with an input power of $P_{in} = 1$ mW is connected to the input. For each frequency, the reflected power with respect to the input power $|S_{11}|^2$ is determined over the time span, using a spectrum analyzer. Afterwards, these data sets are unified to form a dynamic frequency spectrum measurement. At each instant, the Lorentz curve is interpolated to deduce the resonant frequency f_0, quality factor Q, and mismatch ΔM at said instant, which gives the dynamic data as visualized in Figure 2.2a. The geometry of the setup is provided in Figure 2.1a.

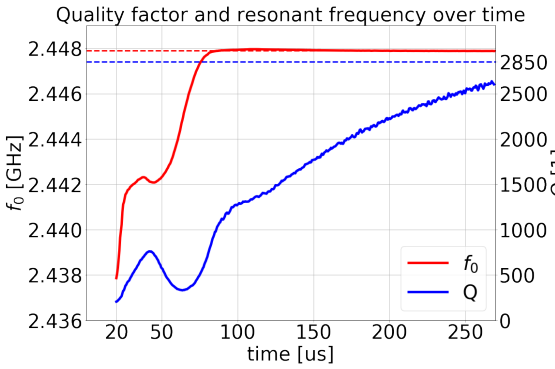

(a) *Resonant frequency f_0 and quality factor Q over time. Obtained from data obtained by [5].*

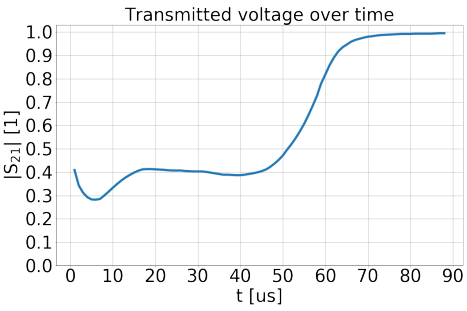

(b) *Normalized voltage transmission $|S_{21}|$ at time t after laser pulse for the 57 GHz setup. Obtained by a direct copy of Figure 5.5 in [12].*

Figure 2.2

C: 57 GHz measurements

Higher frequency measurements are made on the frequency of $f = 57$ GHz, where the plasma is created in between two identical horns with trapezoidal prism shape, and transmitting a signal created by a Gunn-oscillator. At the $f = 57$ GHz excitation frequency, the transmitted voltage of the signal is measured over a time span similar to that of the 2.45 GHz measurements. This method of which is fully explained in [12], and provides a dynamic attenuation of the transmitted voltage by the plasma. Setting the plasma's absence as $|S_{21}| = 1$, the attenuation $|S_{21}|$ by the plasma provides additional information over the 2.45 GHz measurements. Foremost, this higher frequency causes the field to permeate further into an

identical sample, with respect to 2.45 GHz. The author assumes that beyond 30 us at least, this allows us to ignore effects of the EC, such that the $|S_{21}|$ plasma response is fully determined by the LP. The measurement results involve the phase shift as well, but the utilization of this data has not been pursued by the author. The transmission measurements consist of data measured in [12], and are plotted in Figure 2.2b. The geometry of the setup is given in Figure 2.1b

2.3 Simulation models of measurement setups

Now that we have introduced the setup properties for 2.45 and 57 GHz, it is logical to already come with a detailed description of the modelling in simulations. Simulations will make up the majority of the data that this paper will supply and analyze. Moreover, having explained the simulation models allows us to focus on the characterization of the plasma in future chapters.

Our ultimate goal in this paper is to characterize the composite plasma. However, as for the 2.45 GHz measurements, this requires first characterizing the empty cavity. RF measurements on the plasma have been made in a microwave cavity, changing the cavity's mismatch ΔM, quality factor Q, and resonance frequency f_0. Before we can study the perturbations on these parameters by the plasma, we first need to accurately characterize the setup by the empty-cavity parameter values.

2.3.1 Introduction to Comsol's RF-module

Comsol's RF-module simulates electro-magnetic waves travelling through (domain-wise) and being trapped (boundary-wise) in some object. In order for RF-simulations to be run on said object, three aspects must be defined on the object:

1. The geometry
2. The material properties
3. The electro-magnetic properties: wave equations within domains and conditions on the set of boundaries that encapsulates these domains

In addition, the author has found functions for parameters R and ρ in terms of arbitrary Cartesian coordinate (x, y, z) within the simulation

model. Using these, one can assign distributions of material properties within the domain of the LI-plasma.

Complete description of model-building

Firstly, the geometry of the model is must be defined by some combination of common topological shapes (block, cylinder, torus, etc), each centered at some coordinate (x, y, z), and with its dimensions defined ($a \times b \times d$, (R, h), (r, a)). Additionally, topological relations (such as union, intersection, difference) can be defined as relations on two or more different shapes to create the desired final geometry. This final geometry - on which simulations are made - is henceforth called the 'object'. If consisting of multiple topological shapes, the object will be a union of these (non-overlapping) shapes which are designated as unique *domains*. Each domain allows the designation of unique material- and meshing-properties in pre-simulation, or analysis of electro-magnetic properties in post-simulation.

Secondly, material properties must be assigned to the different domains within the object, and to the boundaries encapsulating the object.

As for domains, the material properties needed to fully define a domain under RF is a set of three values that depend on the wave equation chosen under electro-magnetic properties. The two different wave equations are *"relative permittivity"* and *"dielectric loss"* corresponding to the set of material properties $(\mu_r, \epsilon_r, \sigma)$ respectively (μ_r, ϵ_r', ϵ_r''). In both approaches to the wave equation, the propagation of waves (between two mesh elements) is determined by all three material properties. The losses within a mesh element are defined by a single material property: under "Relative permittivity" depending on σ, and under "dielectric loss" depending on ϵ_r''.

As for the boundaries, the only boundary type requiring material properties is the *"Impedance boundary condition"*. If a boundary-element of a mesh-element is assigned an IBC, then the field-element of the wave-vector perpendicular to the boundary element is reflected with some loss depending on the material property σ assigned to this boundary.

Lastly, electro-magnetic waves are computed within the object. By default, the initial conditions within the object are such that there is no field.

The simulation computes the resulting field within the object under the excitation by some *"Port"* boundary. The Port condition is assigned some input power, and a port mode. This mode type causes its corresponding

Version of July 8, 2021– Created July 8, 2021 - 13:14

travelling wave to emanate perpendicular to the port boundary, and into the object. The input power determines the amplitude of the resulting field.

The propagation of waves through the object is determined: by the general wave-equation and the material properties of the domains (as discussed); and by the boundary type and material property of the remaining boundaries encapsulating the object. Aside from the *Port*-condition and *IB*-condition already mentioned, there are two other boundary conditions to be used in future. Firstly, the *"Perfect electric conductor"-condition* (*PEC*), is equivalent to IBC but with $\sigma \to \infty$. Secondly, the *scattering boundary condition* (*SBC*) acts like a plane into free space, similar to a perfectly matched layer, in that all of the field incident on the plane disappears.

Domain-based material properties will always fall into the category of helium, air, quartz, EC plasma, and LP plasma. Boundary-based material properties will always be those of aluminum. The input port will be placed at just before the iris, and will introduce a rectangular mode (representing the preceding length of rectangular waveguide excited by a coax to waveguide transition) with an input power of $P_{in} = 3$ kW.

There are two types of *study* for the RF-simulations. The *Eigenfrequency* study determines a list of complex eigenfrequencies of the model, around a user-delivered real-valued frequency, but does this for arbitrary *port 1* input power. The *Frequency domain* study determines the response of the model to a single user-delivered real-valued frequency and pre-determined *port 1* input power.

Extraction of useful data after running simulations

The following parameters can be evaluated after running the model in order to derive useful data from the simulation run:

As for global evaluations:

- *emw.freq* : Used in Eigenfrequency study. Gives the resonant frequency of the entire system
- *emw.Qfactor*: Used in Eigenfrequency study. Gives the quality factor of the entire system
- *emw.S11*: Used in Frequency domain study. Gives the complex reflection coefficient of the entire system for a given frequency.

As for local evaluations:

- *emw.Qe* : Used in Frequency domain study. Gives the RF- power absorption density in [W/m^3] at some coordinate. Its slice representation is given in the right-most column of Figure 3.1. In data extraction, the *volume integration* of this parameter is made over either the LP or EC domain in order to derive the power absorption ratio
- *emw.normE* : Used in either study. Gives the time-averaged electric field magnitude $|E_0|$ in [A/m^2] at some coordinate. Its slice representation is given in Figure 5.4c and in Figure 5.6b
- *emw.normB* : Used in either study. Gives the time-averaged magnetic field magnitude $|B_0|$ in [T] at some coordinate. Its slice representation is given in Figure 5.4d and in Figure 5.6c

Useful coordinate transformations in terms of Cartesian coordinates

As will become clear later, we require the definition of coordinates near the plasma in order to implement distributions within the plasma. The origin of the coordinate systems we used is the coordinate of the laser focus, or equivalently the center of mass coordinate of the LI-plasma. There are two coordinates over which material properties of the plasma will be assigned distributions: the radial distance from the laser axis R, and the radial distance from center of the torus cross-section ρ. The latter coordinate ρ is most intuitively explained as the closest distance to a torus with major radius $r(t)$ and minor radius $1/\infty$.

We can fully characterize the geometry of the domain and the distribution of material properties assigned within it with parameters in the following units:

- time t in [us]
- major radius r, minor radius a, axial radius R, and torus-cross-sectional radius ρ in [mm]
- volume V in [mm^3]

In terms of some point with Cartesian coordinates (x, y, z) within the plasma domain, we can express the parameters R and ρ with the following equations, where we take the torus axisymmetric with $\hat{y}$:

$$R(x,z) = \sqrt{x^2 + z^2} \tag{2.1a}$$

$$x_0(x,z,t) = \frac{x \cdot r(t)}{R(x,z)} \tag{2.1b}$$

Version of July 8, 2021– Created July 8, 2021 - 13:14

$$z_0(x,z,t) = \frac{z \cdot r(t)}{R(x,z)} \tag{2.1c}$$

$$\rho(x,y,z,t) = \sqrt{\left[r(t) - \sqrt{(x - x_0(x,z,t))^2 + (z - z_0(x,z,t))^2}\right]^2 + y^2} \tag{2.1d}$$

2.3.2 Simulation model of empty TE-101 cavity

As for the geometry, the setup waveguide and cavity have cross-sectional dimensions (along $\hat{z}$) of $a \times b = 90 \times 40$ mm^2. The cavity is enclosed by an iris-plate with a thickness $\delta = 1$ mm, a distance d from the short, and with a circular aperture at its centre of radius $r_0 = 10.5$ mm.

For finer matching, only the stub at $\lambda_g/4 \approx 42$ mm from the iris has been protruded into the waveguide, at a stub protrusion height of $h_s = 13.5$ mm. This is an M14 stub, which has a radius of about 7 mm.

For optical access, the cavity has three more openings aside from the iris-aperture. Each of the optical openings are elongated by roughly cylindrical tubes to be characterized their inner cylindrical shape with radius and height (r, h). Two of the tubes are centered at the upper and lower $\hat{x} \times \hat{z}$-planes respectively. The lower tube with $(r_f, h_f) = (7.5, 60)$ mm^2, and the upper tube a stack of a bottom cylinder and upper horn with $(r_l, h_l) = (5, 5)$ mm^2 and $(r_u, h_u) = (7.2, 22)$ mm^2 respectively. Lastly, a tube that is centered at the short ($\hat{x} \times \hat{y}$-plane), with $(r_s, h_s) = (10, 80)$ mm^2.

As for the material properties, the cavity and waveguide are filled with helium gas allowing us to approximate $(\epsilon_r', \epsilon_r'') \approx (1, 0)$ for the domain material properties. All boundary components are made of aluminum. By [2, p. 21], aluminum conductivity is in the range $\sigma_{Al} \in [1, 3] \cdot 10^7$ S/m. This possible error of a factor $\frac{3}{1} = 3$ would lead to an error for the quality factor Q by a factor $\frac{Q(\sigma=3e7)}{Q(\sigma=1e7)} = \sqrt{3} \approx 1.7$, as follows from (1.17a). Therefore, we determine the aluminum conductivity σ_{Al} specific to our setup by a sweep of the value applied to the geometry in Figure 2.3. and determining for what value of σ_{Al} the pre-pulse measurement values $Q_0 = 2850$ and $\Delta M = 0$ are reproduced. The same is done for the cavity depth d, as this should provide $f_0 \approx 2.4497$ GHz.

Reproducing these values in Comsol, for the geometric properties already known, requires the following additional parameters for the setup:

- $d = 82.52$ mm

- $\sigma_{Al} \approx 1 \cdot 10^7$ S/m

The simulation model of the 2.45 GHz shown in figure 2.3 is modelled as follows. Input port (1) at the left-most surface, just in front of the stub. All remaining boundaries are IBC with $\sigma_{Al} = 10^7$ S/m. Domains other than plasma are given free space material $(\mu_r, \epsilon_r', \epsilon_r'') = (1, 1, 0)$. The plasma is a torus axisymmetric with $\hat{y}$ and centered in between the upper and lower tube, with major and minor radius $r(t)$ resp. $a(t)$. The plasma is given separate properties to be discussed.

Simulation model of 57 GHz setup

The simulation model of the 57 GHz shown in Figure 2.4 is modelled as follows. Input port (1) at the left-most surface, and output port (2) at the right-most surface. Domains other than plasma are given free space material $(\mu_r, \epsilon_r', \epsilon_r'') = (1, 1, 0)$. The horn boundaries are PEC, and the cylinder boundaries not adjacent to the horn-openings are SBC. The plasma is a torus axisymmetric with $\hat{y}$ and centered in between the horns, with major and minor radius $r(t)$ resp. $a(t)$. The plasma is given seperate properties to be discussed.

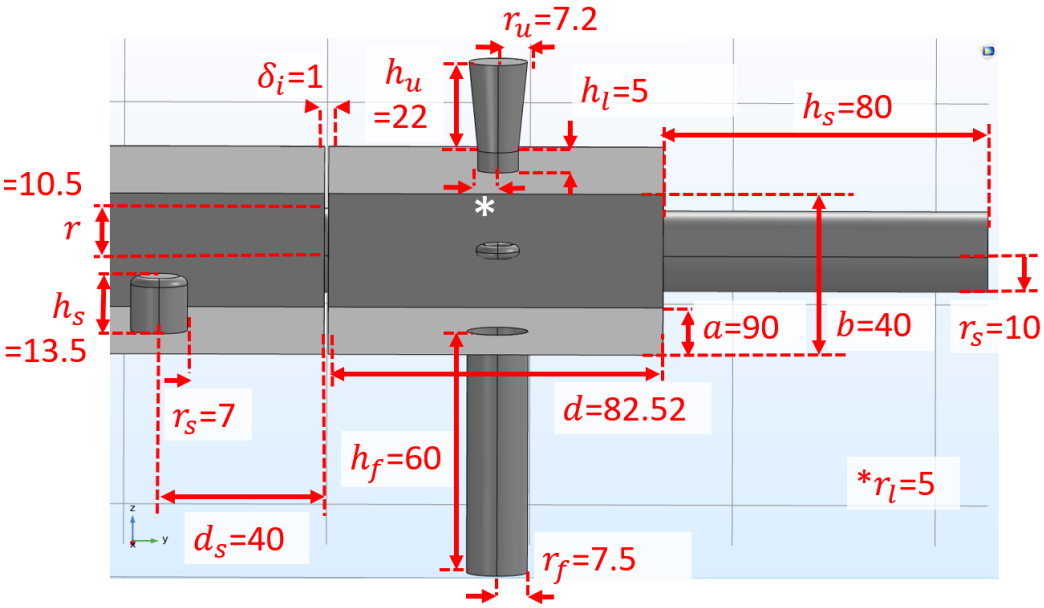

Figure 2.3: *Simulational model of the 2.45 GHz setup. Geometry is indicated in [mm].*

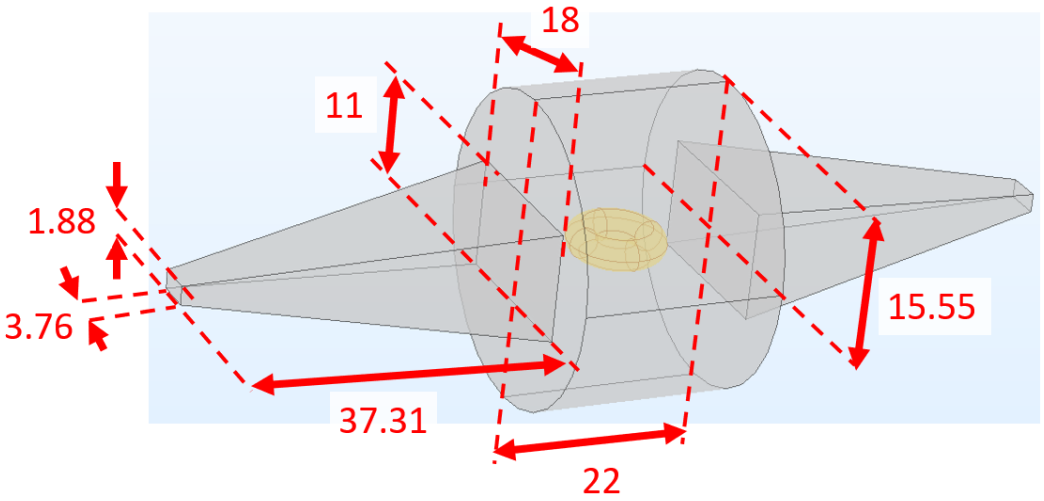

Figure 2.4: *Simulational model of the 57 GHz setup. Geometry is indicated in [mm]. Model geometry is symmetric in the $\hat{x} \times \hat{y}$-plane at the center (I'm just saying that the horns have the same geometry)*

2.4 Preliminary simulations on torus-shape in TE-101 cavity

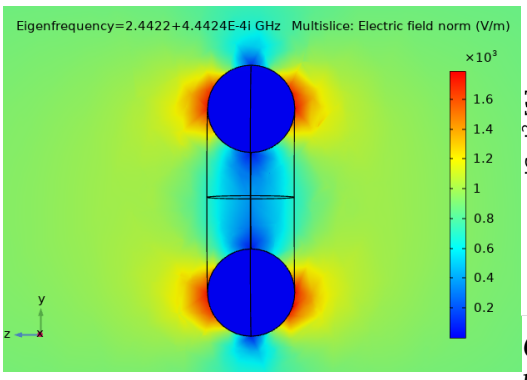

(a) *Magnitude of simulated electric field norm [V/m] near a torus-shape beyond cutoff at the center of the TE_{101} cavity. The 2.45 GHz oscillating electric field is parallel to the torus symmetric axis.*

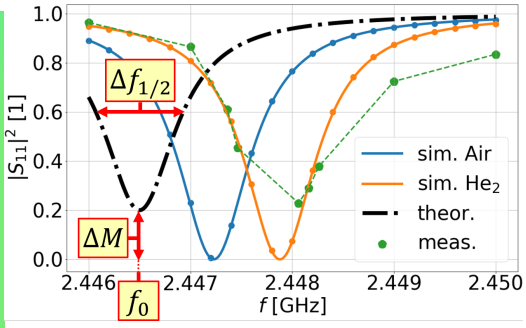

(b) *Comparison of frequency-dependent power reflection-curve, for simulation data sim. and measurement data meas. of the empty cavity. An additional theoretical power reflection curve* (1.23b) *is plotted for example-parameters* $(f_0, Q, \Delta M) = (2.4465[\,GHz], 2850, 0.2)$.

Figure 2.5

Electric field near a plasma beyond cutoff

Before continuing on, it is worth mentioning the shape of the E-field near a torus beyond cutoff at the electric field antinode of (read: center of) the microwave cavity. This can be seen as a linear rainbow-colour plot of the E-field near the plasma in Figure 2.5a.

The perturbed electric field influences the energy density within a shell of 1 mm around the the torus, with the energy density either amplified or reduced depending on the normal direction $\hat{n}$ of the boundary element of the plasma closest to some nearby element. For nearby elements with $\hat{n}$ such that $\hat{n} \perp \hat{R} \sim \hat{n} \times \hat{R} = \hat{\theta} \neq 0$, the field is doubled and the energy density thus quadrupled. Vice versa, for nearby elements with $\hat{n}$ such that $\hat{n} \parallel \hat{R} \sim \hat{n} \times \hat{R} = 0$, the field is negated and the energy density is thus zero.

Direct reproduction of power-reflection data

The ratio of reflected power at t=0 μs, should accurately overlap with the $|S_{11}|^2$ plot produced by simulations of this empty cavity model. The ge-

ometry of the empty cavity is visualized in 2.3, with the corresponding reflected power plotted in 2.5b with label *meas*. From the accordance of simulated values of $|S_{11}|^2$ for the Helium-filled empty cavity (*sim.* He_2) with values from measurements at $t < 0$, we see that we have accurately modeled the empty cavity in simulations. It is useful to address some of the components influencing the RF-properties in small ways in order to justify ignoring them. Such small deviations include the substitution of air with helium, and the tubes opening up the cavity. These differences will be studied in the simulation model of the empty cavity.

Deviating resonance frequency of Air- vs. Helium-filled cavity

An interesting detail was that upon substituting the air in the vacuum chamber for Helium gas, the resonance frequency measurement of the same system shifted upward with $\Delta f_{Air \to He_2} = +0.7MHz$. Of course, it is logically determined from (1.30) that $\Delta f_{Air \to He_2} \approx +0.65$ MHz. Moreover, this shift can also be verified in simulations, and this is seen in Figure 2.5b by comparison of the curve indicated with *sim. Air* and that with *sim.* He_2 to identify the same frequency shift $\Delta f = +0.65$ MHz corresponding to substitution of the Helium with Air into the empty cavity domain, values of dielectric in Table 1.2.

Influences on f_0 and Q by the tube openings

Secondly, the three cavity tubes (characterized in Figure 2.3) influence the cavity RF-properties. Near the tube at the short, the B-field is at maximum. Near the other two tubes, the E-field is at maximum. Any field close to the tube entry leaks into the tube. A field forms in the tube that drops exponentially over the distance from the entry plane, due to cutoff. Because of the tubes are so long, the resulting field near the other end of the tube is nearly ignorable (-60 dB field strength, I believe). The tubes act like an enlargement of the cavity volume, approximated as the sum of tube-volumes containing significant field strength $E(d) > e^{-1} \cdot E_0$ with $E(d = \delta) = e^{-1} \cdot E_0$, as in $\Delta V \approx \Sigma A \cdot \delta$. This virtual increase of cavity volume relates to a decrease in cavity resonant frequency, which for this tube-system is $\Delta f_{\varnothing \to tubes} = -3.6$MHz. To a lesser degree, the power lost to the leakage from the outer ends of the tubes and induced currents within the tube walls cause a reduction of the quality factor which has been found to be a factor 0.95 reduction of the empty cavity quality factor. These are small differences that henceforth will be ignored.

Version of July 8, 2021– Created July 8, 2021 - 13:14

2.5 Transmission line calculations on empty TE-101 cavity

In this section, we aim to construct an equivalent circuit model of setup based solely on the conductivity of the walls, the setup dimensions, and resonant frequency. The behaviour of the resulting resonant circuit is then compared to simulations of the setup. We compute that for the custom waveguide: $Z_{wg} = Z_0 \cdot \frac{\lambda_g}{\lambda_0} = 377 \cdot \frac{166.9}{122.45} = 513\ \Omega$.

Starting with the Q-factor of the boxed empty cavity, equation (1.17a), we get $Q_0 \approx 6466$. From equation (1.11b), we get $L = 97.25\,\text{nH}$. From equation (1.13) with $\mathcal{L} = 0$ we thus get $R = 231.5\,\text{m}\Omega$. This value is verified by equation (1.11a), where $R = \kappa Z_{wg} \alpha d = 1.365 \cdot 513 \cdot 3.97 \cdot 10^{-3} \cdot 83.45 \cdot 10^{-3} = 232\,\text{m}\Omega$ and equivalently, $R = \omega_0 L / Q_0 =$. For the capacitance to give the resonant frequency in (1.12) with the value of L, we must thus have: $C = \frac{1}{\omega_0^2 L} = 43.4\,\text{fF}$. The resulting equivalent circuit is visualized by substitution of these values into their corresponding lumped elements in 1.1b.

By (1.15), the value for the resistance of the cavity needs to be equal to the resistance associated with the source, which gives us the required value for $\mathcal{L}$: $\mathcal{L} = 0.708\,\text{nH}$, as must be the case for ideal power transfer. By first approximation, modelling the iris as infinitely thin, we deduce $r_0 = \sqrt[3]{\mathcal{L}/a}|_{\psi=1} \approx 9.1\,\text{mm}$. The iris thickness we will use in our setup is $t = 1\,\text{mm}$. The corresponding iris correction factor for this radius and thickness by (1.21) equals $\psi = 0.713$. By the relation $r \propto \sqrt[3]{1/\psi}$, the required iris radius for the iris thickness equals:

$$r_0' = \sqrt[3]{1/\psi} \cdot r_0 = 1.12 \cdot 9.1\,\text{mm} = 10.2\,\text{mm}$$

, which is exactly the iris radius to give matching in simulations of the empty TE_{101} cavity, as will be confirmed in Figure 2.6b.

In order to visualize the equations (1.22), we should justify our approach by comparison with simulations in Comsol. The simulation model in Figure 2.3 is used, but without a stub such that $h_s = 0$. We make parametric sweeps of the iris radius r in simulations and analyze f_0, Q, and ΔM in each run. We can then compare these simulation data with the relations deduced in theory (1.22). These plots are given in Figures 2.6a, 2.6b, and exhibit good accordance for all RF-parameters.

Version of July 8, 2021– Created July 8, 2021 - 13:14

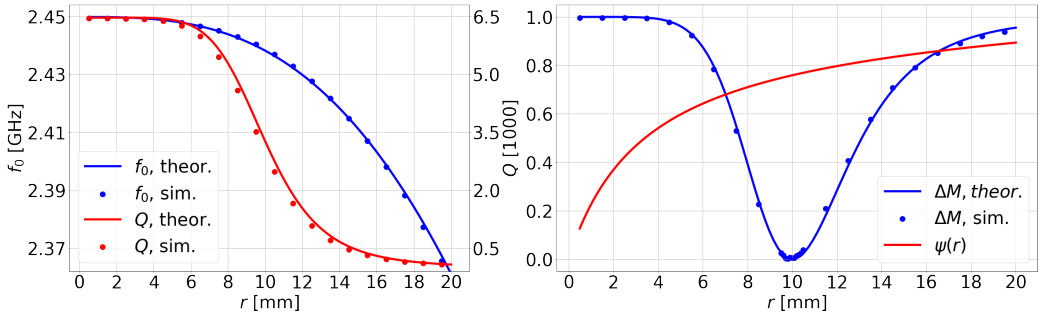

(a) *Resonant frequency and quality factor over iris radius*

(b) *Mismatch and iris correction factor over iris radius*

Figure 2.6: *Simulated (line) and theoretical (scatter) values of f, Q, ΔM, and ψ over r, compared. Theoretical values correspond to equations* (1.22a), (1.22b), (1.22c), *and* (1.21) *for $t = 1$ mm. The simulated values are extracted from a sweep over r in the simulation model of the TE_{101} cavity in Figure 2.3.*

Some useful parameters of the rectangular TE_{101} cavity

For the purposes of power absorption calculations in the plasma (1.48b) and (1.46a), we require the approximate empty cavity field amplitudes B_0 and E_0. For the rectangular TE_{101}-mode heating setup, the approximate quality factor is $Q = 3000$, and the input power $P_{in} = 3$ kW, with the magnetic field distribution given in (1.8). Insertion of these setup parameters into (1.50) yields $B_0 \approx 0.002$ T. Simulations on the TE_{102} rectangular cavity yield $B_0 \approx 0.004$ T.[†] This might be due to time-average field not being accounted for, or due to some other discrepancy. Nevertheless, this value for the magnetic field antinode amplitude and the corresponding value of the electric field amplitude will be used in theoretical capacitive- and inductive power absorption calculations of the plasma for the rectangular TE_{101} and rectangular TE_{102} heating setups. All properties of the TE_{101} setup (also providing approximate properties of the TE_{102} setup) are given in Table 2.1.

[†]The author forgot to analyze field strength in simulations on the TE_{101} cavity. The simulation model of the TE_{102} mode is similar in size and quality factor, however, and is described in Figure 5.4.

B_0	$4 \cdot 10^{-3}$	T		Z_{wg}	513	Ω
E_0	$1.2 \cdot 10^{6}$	V/m		R_0	0.2315	Ω
P_{in}	3000	W		L	97.25	nH
Q_{empty}	2850	[1]		C	43.4	fF
ω_0	$2\pi \cdot 2.45 \cdot 10^{9}$	Hz		λ_g	166.9	mm
V_0	$3 \cdot 10^{-4}$	m^3		$\mathcal{L}$	0.708	nH
λ_0	122.45	mm		α	$3.97 \cdot 10^{-3}$	m^{-1}
a	90	mm		b	40	mm
d	83.45	mm		a_0	$9.3 \cdot 10^{-4}$	$\Omega \cdot s \cdot m^{-3}$

Table 2.1: *Properties of the rectangular* 90×40 *[mm]* TE_{101}*-mode 2.45 GHz measurement setup.*

Chapter 3

CCD image interpretation

The LI-plasma is observed by a CCD camera with select-able view direction; either behind the short (side view), or the opposite to the laser (front view). Only the side view image of the plasma are used, as they best visualize the plasma's composition; because the LP and -EC luminous regions will not overlap and because their axial symmetry allows for the determination of the cross-section emissivity. In Figure 3.1 left and center column, the side view image of the plasma is plotted with colour scale along linear intensity, with raw image on the left and *Inverse-Abel-Transformed* (IAT) image at the center for luminosity under capacitive heating. In terms of the left column, the LP is the vertical disk-shape in the center of the image, and the EC are the two vertical disk-shapes on either side of the LP; the EC is only visible/luminous if capacitive heating is activated. The first goal is to find functions for the geometric parameters of the LP and EC, from the size and position of their luminous regions. Secondly, to make Ansatz function for the (exponential) decay of the LP-electron density, and Ansatz function for the (crescent-shaped) charge distribution within the LP. Lastly, the total intensity inside and outside the LP-demarcation (from LP-geometry $(r, a)(t)$) is used to derive the stability time for the LP resp. EC.

The CCD-images are contained in *.SPE*-files, which are 512×512 [px^2] (1 [mm] $\sim$ 41.45 [px]) arrays representing the radiant intensity measured at each pixel. Aside from section 3.4, analysis in this chapter is limited entirely to the two data-sets *zmage-17678.SPE* and *zmage-17679.SPE* corresponding to inactive resp. active RF-heating. They cover a time period $t \in [22, 104]$ [us] after the laser-pulse, possess a gate width of $\Delta t = 0.25$ [us], and are averaged over 50 exposures. The description of the heating setup used under active heating is explained in subsection 2.2.1.

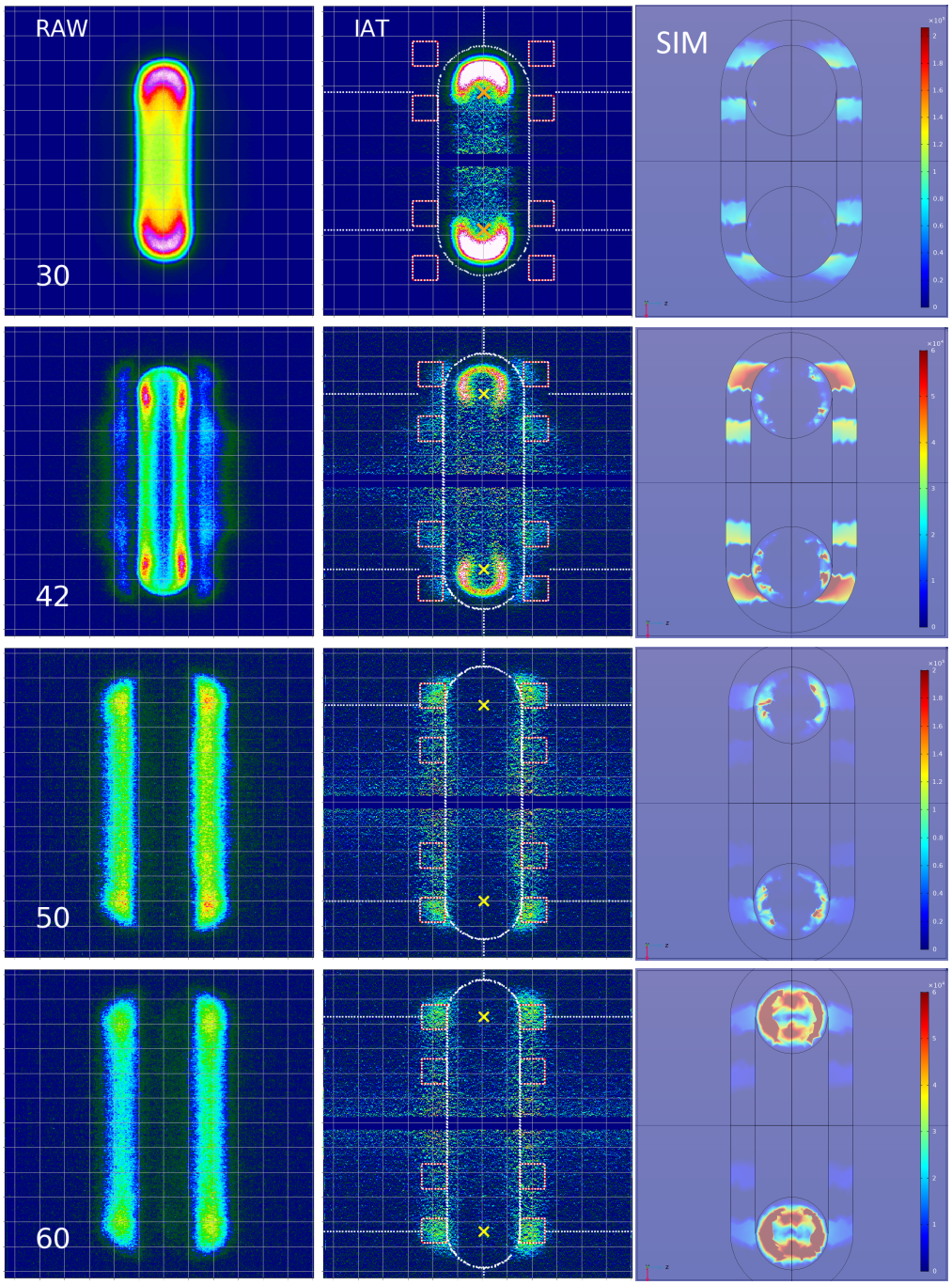

Figure 3.1: *Collage of plasma representations. Each row represents the plasma at - from top to bottom - time* $t \in [30, 41, 50, 60]$*, obtained from zmage-17679.SPE frames* $5, 11, 15, 20$*. Each column represents the plasma as - from left to right - raw image, IAT image, slice of simulated emw.Qe under final characterization.*

3.1 LP-geometry: major and minor radius

The LP major radius and minor radius will be determined by summation over either of the two axes of the (raw/IAT) CCD images, over time. Both parameters will be determined by analysis of a horizontal/vertical intensity-spectrum $I(x)$ to be obtained by summation over one of the .SPE-array-axes. The array has two axes; one being the vertical axis $\hat{v}$ with a range of coordinates v, the other being the horizontal axis $\hat{w}$ with a range of coordinates w. The major radius will be determined by the spectrum summation over the vertical axis $\hat{w}$, giving a spectrum $I(v)$. The minor radius will conversely be determined by summation over $\hat{v}$ giving a spectrum $I(w)$. Spectra hence obtained are noisy. For this reason, such a spectrum will always be converted to a polynomial with a Savitsky-Golay filter.

3.1.1 Determination of major radius $r(t)$

We determine $r(t)$ for two different time domains when the region within the torus-outline (associated with the LP-torus geometry) is luminous, employing a different method and data set on each. During the initial period ($t \in [22, 46]$ [us]), radiant intensity originates from the natural decay of the highly-ionized LP-torus, after which the radiant intensity is indistinguishable from noise. During the final period ($t \in [60, 100]$ [us]), radiant intensity within the torus-outline emerges above noise-level, and originates from RF power absorption.

Evident from Figure 3.1 (first column, second row $t = 41$ [us]), the LP-torus is pierced into a crescent-shape by a (cold, lowly-ionized) *splitting gas disk* (SGD), and images [19, Figure 5.8] at $t = 50$ [us] reveal that the LP has been split entirely into two separate disks. In contrast, the late-period ($t > 60$ [us]) radiant intensity consistently appears from a single torus-shape centered at the LP-cross-sectional outline. Unless the two LP-toruses have merged before $t > 60$ [us], this single-torus power absorption is more likely emergent from the low-conductivity SGD. A study of the early-period LP cross-sectional intensity profile is done in Figure 3.7 of Section 3.3 , and extrapolation of the data yields a merger (or at the least a very close proximity) of the separated LP-toruses around $t = 55$ [us] into a single torus, situated just below the SGD in the $\hat{R}$-direction. Consequently, capacitive RF power absorption necessarily favours the LP at any time over its decay from beyond cutoff to below cutoff, assuming LP-conductivity to be consistently well above SGD-conductivity. If the LP is beyond cutoff, then by Figure 2.5a, no RF-energy is present within the SGD. If the LP is below cutoff, then RF-energy is absorbed into the

LP. In conclusion, radiant intensity within the torus-outline is always attributable to the LP.

Firstly, over time $t \in [22, 46]$ [us] when the LP radiates its initial ionization energy, no heating is used. Analysis starts at the earliest picture $t = 22$ [us] up to the time $t = 46$ [us] where the SNR is too low. For each t, on the corresponding array, a *torus-outline* associated with the side view of a torus with some major radius r and minor radius a is drawn, coinciding with the set of pixels that have closest distance $a = 1$ [mm] to the *center-line*. The center-line is the vertical line between the LP's cross-sectional centers $(w, v) = (c \pm r, c)$. To derive the most probable major radius $r(t)$ of the torus at time t, the major radius is swept around $r \approx 3$ [mm] and the variance of the pixel-intensities at the torus-outline is calculated. By sweeping the outline's major radius r, the optimal major radius $r(t)$ is identified as the major radius r for which the variance is at minimum; this process is outlined in Figure 3.2a. The left column shows the raw image (above) and its IAT (below), and the central column shows normalized intensity of the raw images, with zero-intensity within the torus-outline. From top to bottom, outlines are drawn around optimum, $r = r(t) + \Delta r$, with a margin of $\Delta r = -10, 0, +10$ [px]. In the right column, the IAT-intensity within the torus-outline is given for smaller minor radius $0.75 \cdot a$ in the red scatter plot, where $r = r(t)$ yields gradient of the outline parallel to the gradient of the crescent-shape.

Secondly, over time $t \in [60, 100]$ [us] when the LP radiates energy from RF-power-absorption, heating is used. Analysis starts at the first increase of LP luminosity under RF-excitation at $t = 60$ [us] (see future Figure 3.12a) up to time $t = 100$ [us] when the magnetron is shut off. This process is automated and results are plotted in Figure 3.3. When the raw image is summed over the vertical axis $\hat{v}$, a spectrum $I(w) = \sum_{v=1}^{v=512} I(v, w)$ is obtained with three maxima, with two minima in between called w_1 and w_2 coinciding with the "dark regions" in between the LP and EC. Having obtained this information from the $I(w)$-spectrum, we can filter out the influence of the EC by setting the intensity of the array to zero for $w \in [0, w_1] \cup [w_2, 512]$. Within the slice $[w_1, w_2]$ representing the LP-domain (mid-bottom), the highest luminosity lies just below the center of the actual LP cross-section, because of the raw image being a line integral over the full side view of the LP-torus. In order to obtain the (more suitable) cross-section of this torus, the IAT image $J(v, w) = F^{-1}I(v, w)$ of the raw image is taken, and the LP's intensity-spectrum $J(v) = \sum_{w_1}^{w_2} J(v, w)$ is obtained by summation over the horizontal axis $\hat{w}$ for $w \in [w_1, w_2]$. We obtain two peaks above and below the central axis, with the distance in

Version of July 8, 2021– Created July 8, 2021 - 13:14

between evidently equal to the diameter $d = 2r$ of the LP-torus.

We now have two data sets of $r(t)$ for two different time domains, with a hiatus for $t \in [46, 60]$ us. We must find a function $r(t)$ to fit to the data in order to interpolate between known data values, and extrapolate to acquire data within the hiatus. A visual inspection of the data alone led to the choice of an asymptotic, logarithmic increase $r(t) = r(t = \infty) - \exp\left(\frac{(t_0 - t)}{b}\right)$. However, this is an educated guess, and flow dynamics of vortex ring expansion might correct this radial expansion to follow some n^{th}-root function. By the *curve_fit*-module in *Python* (which employs the Levenberg Marquardt algorithm [20]), the optimal fit $r(t)$ in (3.1a) is deduced, with optimal fit-parameters $r(t = \infty) = 5.8$ [mm], $t_0 \approx 75$ [us], and $b = 42$ [us]. This fit-function is formalized in (3.1a).

3.1.2 Determination of minor radius $a(t)$

The minor radius $a(t)$ of the LP will be determined by the value a for the torus-outline that best corresponds with the interface of LP and EC, under the effects of heating. The LP domain is necessarily restricted in between the two luminous EC-domains, but it is a matter of debate whether the LP occupies the entire region in between the EC as it contains a large dark region. From the left-most column of Figure 3.1, the dark region is visible in between the luminous LP and -EC; in between two plasma-components. Logically, the dark region must also likely classify as a plasma with an electron density somewhere in between that of LP and EC. Parts of the plasma can be luminous either due to radiation during its natural decay or due absorption of the local electric field. For $t < 46$ [us], the LP is luminous because of the former, and the EC is luminous because of the latter. As for the dark region - situated at the edge of the LP-torus such that $\rho \approx a$ -, intensity is surpassed by the higher charge-density-based radiation well inside of the LP $\eta(\rho) \ll \eta(\rho/2)$, yet with electron density beyond cutoff density $\eta(\rho) \ll \eta_0$ such that no RF-radiation is absorbed. The dark region is therefore classified as LP, and is most likely due to non-homogeneous cross-sectional LP-electron density.

The minor radius of the LP is determined using three different routines on the horizontal intensity spectrum, and the method is explained in Figure 3.4a. Before, summation over the vertical axis, in order to filter out the EC 'curling' around the LP (above and below), the pixel-intensities for $v \in [0, c - r(t)] \cup [c + r(t), :]$ are turned to zero. After summation of intensities over the vertical axis, a Savgoy filter is applied to smooth out the spectrum. The three maxima of the resulting polynomial are identified

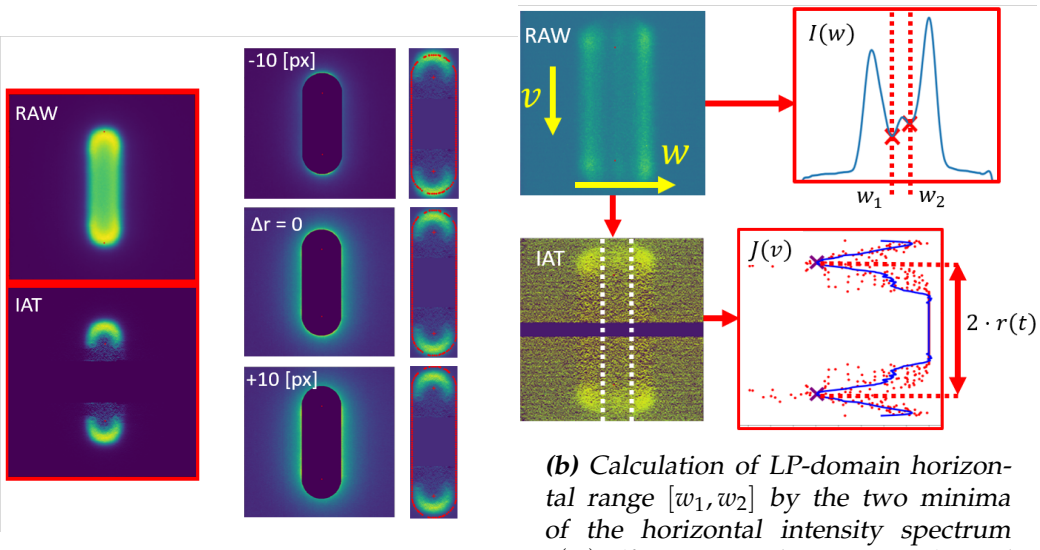

(a) *Parametric sweep of the major radius r, and subsequent initialization of the set of pixels $\{(v_i, w_i)\}$ comprising the race-track, and calculation of the intensity-variance σ_I of pixel-intensities $\{I(v_i, w_i)\}$ at outline-set. The most likely major radius $r(t)$ equals sweep-parameter r for which intensity-variance σ_I is minimal. Method for $t \in [22, 46]$ [us], example: $t = 30$ [us].*

(b) *Calculation of LP-domain horizontal range $[w_1, w_2]$ by the two minima of the horizontal intensity spectrum $I(w)$ (from vertical summation), and subsequent calculation of the maxima of the vertical intensity spectrum $J(v)$ (from horizontal summation) from the IAT-image with non-zero-intensity only within the slice $[w_1, w_2]$ (horizontal sub-domain between pixels w_1 and w_2). The major radius $r(t)$ equals half-distance between the maxima of $J(v)$. Method for $t \in [60, 100]$ [us], example: $t = 80$ [us].*

Figure 3.2: *Visualization of the two methods used for determination of LP major radius, with results plotted in Figure 3.3. The methods are used to determine the most likely major radius '$r(t)$' associated with the LP-torus on the CCD-image at time t. Sub-figures (a) and (b) study non-heated- resp. heated plasma.*

and ordered from high to low value. From highest to lowest maximum, a Gaussian $I(w) = g(w, \mu, \sigma)$ is fitted to the peak and subsequently subtracted from the polynomial. After three-fold repetition of this process, only background noise is left and the spectrum is thus a superposition of the three Gaussian fits. From here, two types of peaks are identified: the outer peaks belonging to the EC, and the inner peak belonging to the LP.

As for the EC, with the outer two Gaussian-fits, the position a is evaluated as half of: (i) the distance between the half-maxima closest to the center, and (ii) the distance between the maxima. As for the LP, corresponding to the inner Gaussian-fit, a is taken as (iii) half the distance between the two one-fifth-maxima (the **inner** Fifth-Maximum threshold consistently yields comparable magnitude of minor radius to the **outer** Half-

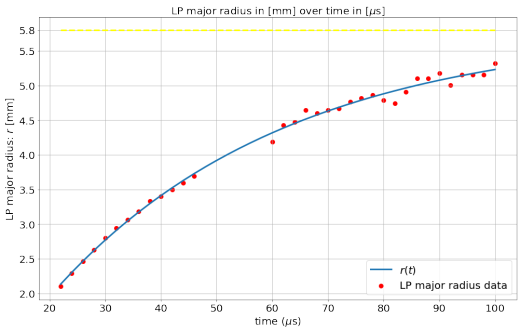

Figure 3.3: *LP major radius $r(t)$. Scattered data obtained by the method in Figure 3.2. Interpolation of an exponential, asymptotic fit is made to the data to obtain equation* (3.1a).

Maximum threshold). The three analyses are visualized at the top-right of Figure 3.4a, and provide the data plotted in Figure 3.4b. A fit to these data is hypothesized as (3.1b), with more reliable evidence to be provided in future.

LP geometry: major radius $r(t)$ [mm] and minor radius $a(t)$ [mm], over time t [μs], under constant volume V

$$r(t) = 5.8 - \exp\frac{(76.64 - t)}{42} \tag{3.1a}$$

$$a(t)|_V = \sqrt{\frac{V}{2\pi^2 \cdot r(t)}} = \sqrt{\frac{180}{2\pi^2 r(t)}} \tag{3.1b}$$

$$V = 180\ \text{mm}^3 \tag{3.1c}$$

3.1.3 Determination of luminous volume $V(t)$, area $A(t)$, and decay length $R(t)$

Although the geometry of the plasma is thus far characterized during its toroidal phase at 30 to 60 microseconds after the laser-pulse, the next section will touch on the thermodynamics of the plasma, in which case we want to characterize the plasma's volume during the early stages of its expansion and subsequent contraction. Namely, the energy deposition of the laser leads to a high temperature at the laser-focus, and thereby to an increase of the plasma's volume. Because the plasma's radiation originates from regions of high temperature, the volume of the plasma's hot region

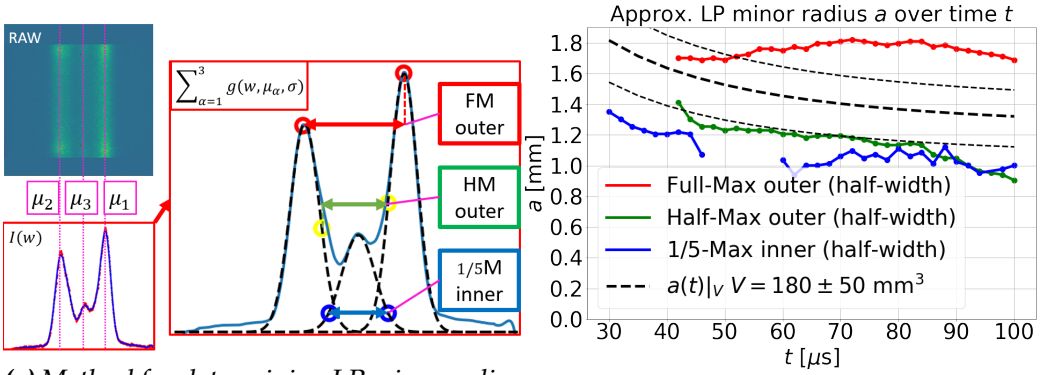

(a) *Method for determining LP minor radius $a(t)$, example: $t = 70$ [us].*

(b) *Plot of evaluation of $a(t)$ from method in (a).*

Figure 3.4: *Three-fold approximate value of LP minor radius $a(t)$ plotted in (b), with method illustrated in (a). Goal: determine minor radius $a(t)$ associated with CCD-image at time t. Method: derivation of horizontal intensity spectrum $I(w)$ by summation of pixel-intensities in between the cross-sectional centers $v \in [c - r(t), c + r(t)]$ associated with* (3.1a)*, then determine the spectrum's maxima μ_1, μ_2, μ_3 ordered in decreasing intensity, then in order of $i \in \{1, 2, 3\}$ fit a Gaussian $g(w, \mu_i, \sigma)$ and subtract it from the intensity spectrum. Result: minor radius is calculated three-fold (i) from the distance between the outer Gaussian maxima, (ii) from the closest distance between the outer Gaussian half-maxima, (iii) from the distance between the inner Gaussian fifth-maxima.*

can be determined by volumetric integration of the its most luminous region.

The volume is determined by re-ordering the $N = 512 \times 512$ pixels comprising the CCD-image from highest luminosity ($I(n = 1) = I(v_n, w_n)$) to lowest luminosity ($I(n = 512^2) = I(v_n, w_n)$) and applying normalization ($\sum_{n=1}^{n=512^2} I(n) = 1$) on the ordered list of pixel-intensities. Cumulative summation of this list yields an ordered list $J(n) = \sum_{i=1}^{n} I(i)$ that is used in post-processing. By setting an arbitrary threshold $tr \in (0, 1)$ for the luminosity, the corresponding critical index $i_{crit}(tr) = \{i : J(i \leq i_{crit}) \leq tr\}$, where the set $[1, i_{crit}]$ is the set of the $i_{crit}(tr)$ most luminous pixels comprising $100 \cdot tr\%$ of the total CCD-luminosity. Lastly, the set of pixels $\{(v_i, w_i)\}_{i \in [0, i_{crit}]}$ is converted to the corresponding volume $V = \sum_{i=1}^{i_{crit}} V(v_i, w_i) = \sum_{i=1}^{i_{crit}} \pi \cdot |v_i - 256| \cdot dx^3$ with $dx \approx 2.4\,[\text{m}\cdot\text{px}^{-1}]$, upon the assumption of axial-symmetry (symmetry in the horizontal axis).

The set of pixels under threshold covers a horizontal range of pixels $w \in [w_{min}, w_{max}]$ $w_{max/min} = max/min(\{w_i\}_{i \in [0, i_{crit}]})$, where each w with has a maximum radius corresponding to maximal distance to the laser

axis equal to $r_i = |v_i - 256| \cdot dx, v_i = max(\{v_j : w_j = w_i\}_{j\in[0,i_{crit}]})$. The subset of pixels $\{v_i, w_i\}_{w_i\in[w_{min},w_{max}]}$ covers the outline/contour of the sub-threshold pixel-set, were the area of this pixel-set then roughly equals $A = \sum_{i=1}^{i_{crit}} A(v_i, w_i) = \sum_{i=1}^{i_{crit}} \pi \cdot |v_i - 256| \cdot dx^2$.

By setting three arbitrary thresholds $tr \in \{tr_a = 0.78, tr_b = 0.89, tr_c = 0.95\}$ for the outline, we obtain three contours of roughly homogeneous intensity, and these are locally parallel. The three contours can be compared pairwise, with each two contours $\{(w_a, v_a)\}_{a\leq N_a}$ and $\{(w_b, v_b)\}_{b\leq N_b}$ possessing average intensities $< I_a > \equiv \frac{1}{N_a}\sum_{a=1}^{a=N_a} I(w_a, v_a)$ and likewise $< I_b >$ along their subset. The average distance between two contours equals $< d_{ab} > \equiv \frac{1}{N_a}\sum_{a=1}^{a=N_a} min(\sqrt{(w_a - w_b)^2 + (v_a - v_b)^2})$. This will be referred to as the characteristic decay length R of the intensity. The ratio of the intensity of the two contours will be referred to as I_1/I_2. All of the above mentioned geometric parameters are encapsulated in Figure 3.5a.

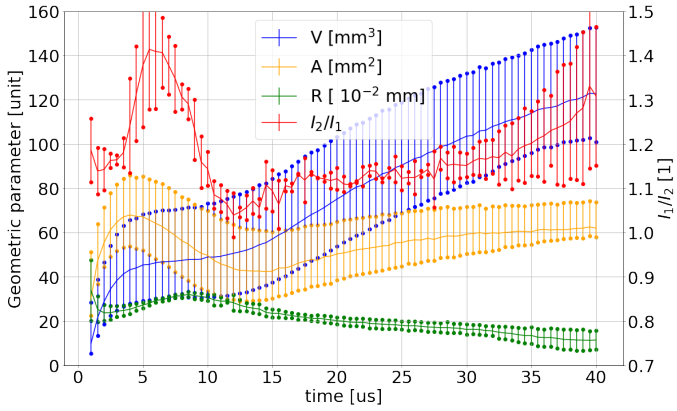

(a) *Geometric properties of the plasma for three threshold values on left axis. Ratio of average intensity at two adjacent contours plotted at right axis.*

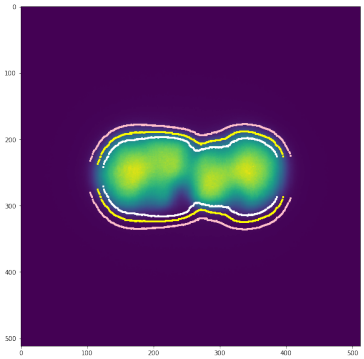

(b) *Raw image of the plasma's radiant intensity at time $t = 2.5$ [us] after the laser-pulse. The pixels within a threshold's contour are represented by the three coloured contours; with the white, yellow, and pink contours representing the thresholds $tr_a = 0.78$, $tr_b = 0.89$, and $tr_c = 0.95$ respectively.*

Figure 3.5

3.2 Dynamic electron density $\eta(t)$, power loss $P_l(t)$, and temperature $T(t)$

Aside from providing the shape of the plasma, the CCD images may also provide information on the material properties of the plasma. Namely, the total radiant intensity of the plasma, the wavelengths at which radiant intensity is emitted, and the relative intensity of the wavelength emissions each provide additional information on the material properties of the plasma: electron density and temperature. From the spectral lines of the plasma's radiant intensity we can deduce the type of radiation process, and the radiation process in turn provides the relation between the intensity and electron density. The relative intensity of the spectral lines provides data on the temperature [21, Equation (7.4)]. Lastly, the - independently calculated - electron density and temperature can then be compared in order to test our equation on the Boltzmann-normalized Saha-equation function $\eta(T)$ in (1.53d).

During the timespan of 10 to 25 microseconds after the laser pulse, the photons emanating from the radiating plasma predominantly possess three wavelengths: $\lambda_1 = 587.5$ [nm], $\lambda_2 = 687.8$ [nm], and $\lambda_3 = 706.5$ [nm] [21, Figure 7.8]. These are spectral lines of the neutral helium atom (He I) [21, Figure 7.3], emitted upon de-excitation of neutral helium atoms. The de-excitation is most likely spontaneous, because this assumption provided a temperature decay [21, Figure 7.4] that provides values in line with simulations on the laser-induced plasma [18, Figure 4.9]. De-excitation of He I is necessarily preceded by its excitation, which probably occurs from impact collision with an energetic electron [22, Paragraph 2.1]. Therefore, the intensity of the spectrum is logically proportional to the electron density, as has been determined for He I in [22, Figure 3(a)] over $n_e \in [10^{16}, 10^{20}] \sim \eta \in [10^{-1}, 10^{3}]$ and for Ar I in [23, Figure 5] over $n_e \in [5 \cdot 10^{15}, 2 \cdot 10^{17}] \sim \eta \in [10^{-1}, 10^{1}]$, meaning $I(t) \propto n_e(t) \propto \eta(t)$.

Upon the assumption that $I(t) \propto \eta(t)$, we want to evaluate the time-dependent normalized electron density $\eta_0(t)$ of the LP from the total non-RF-heated CCD-image intensity $I(t) = \sum_{w=1}^{512} \sum_{v=1}^{512} I(w, v, t)$. We assume that all CCD-intensity $I(t)$ from plasma is due to spontaneous He I de-excitation emissions preceded by electron-impact excitations. Because the intensity $I(t)$ originates predominantly from the LP (to be verified later from the comparison of the intensities in Figure 3.12a), the electron density to be deduced is the electron density of the LP. Substitution of $T(t = 0) = 10^4$ [K] into (1.53d) yields $\eta(t = 0) = \eta(T(t = 0)) = 7.3e6$. Under this constraint of normalization, we obtain the plot of the normalized electron

Version of July 8, 2021– Created July 8, 2021 - 13:14

density over time in Figure 3.6a.

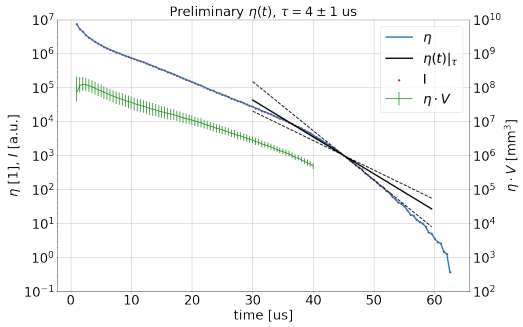

(a) *LP normalized electron density over time. Obtained by normalization of the curve radiant intensity $I(t)$ such that the initial normalized electron density for n_c(2.45 [GHz]), equals $\eta(T = 10^4\ [K]) = 7.3e6$. Plotted in black, electron density under time-independent decay constant $\tau = 4 \pm 1$ [us], $\dot{\tau} = 0$, with pivot at $t = 45$ [us]. Plotted in green is the volume of Figure 3.5a times $\eta(t)$.*

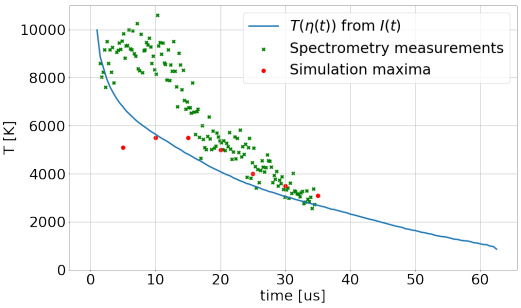

(b) *Temperature of the plasma over time. Spectrometry measurements are data points as plotted in [21, Figure 7.4]. Simulation data are the maximum values of the temperature as provided in [18, Figure 4.9]. The data labeled "$T(\eta(t))$ from $I(t)$" are deduced by the substitution of $\eta(t)$-data in Figure 3.6a into the inverse function $T(\eta)$ of* (1.53d).

Figure 3.6

In order to implement these data into simulations in the next chapter, we aim to extract a function $\eta_0(t)$ over the exponential decay. The function fit is applied over the time range $t \in [30, 60]$ [us], because the composite plasma will be characterized only during this period. The choice for restricting the characterization of the plasma only to this period is motivated by the future method of the reproduction of measurement data: the dynamics of measurements are most outspoken during this same period in both the 2.45 GHz measurements in Figure 2.2a as well as the 57 GHz measurements in Figure 2.2b. Different decay constants are plotted along the pivot $\eta(t = 45)$, and we can infer from these that a suitable value for the LP-decay constant is $\tau_{LP} = 4$ [us]. Although the decay constant is not exactly time-independent, a time-independent decay constant is used with the aim of simplifying our equations as well as reducing the amount of degrees of freedom. The dynamic homogeneous normalized LP-electron density $\eta_0(t)$ is only an order of magnitude estimate, and its implementation in simulations will be made with a parametric sweeps over half order of magnitudes, thereby rendering more unnecessary complexity of the $\eta(t)$ function a mere nuisance.

At the central instant of the characterized period, we read the value $\eta_0(t = 45) = 1e3$, but we will scale this down to the convenient factor $540 \approx \left(\frac{57}{2.45}\right)^2$ in order to ease the normalization of the electron density between 2.45 GHz- and 57 GHz-measurements. In the LP-decay Ansatz (3.2a), we correspond this value to a coefficient c_{LP} with $\eta_0(t = 45) = 1e3 \sim c_{LP} = 1$. Implementation of the Ansatz in simulations will rely on reproduction of the measurements by a parametric sweep of c_{LP}. Because of the exponential decay of $\eta_0(t)$, we will implement this coefficient logarithmically, such that $\eta_0(t) = 10^{\Delta p} \cdot f(t) = c \cdot f(t)$. Sweeping the electron density over half orders of magnitude $\Delta p \in \{0, 0.5, 1\}$, roughly corresponds with sweeping the coefficient c along $c \in \{1, 3, 10\}$. For LP and EC, exponential decay of electron density is expressed in two degrees of freedom; time-independent decay constant τ and logarithmic sweep-parameter c, unified in the Ansatz (3.2).

***Ansatz* for homogeneous LP and EC electron density η_0 over time t in [μs], for decay constant τ in [μs]**

$$\eta_0(t)_{LP} = c_{LP} \cdot 540 \cdot \exp(-(t-45)/\tau_{LP}),\ c_{LP} \approx 1, \tau_{LP} \approx 4[us] \quad (3.2a)$$

$$\eta_0(t)_{EC} = c_{EC} \cdot \exp(-(t-30)/\tau_{EC}),\ \ c_{EC}, \tau_{EC} \text{ unknown} \quad (3.2b)$$

Aside from the material properties, the power loss of the plasma can also be approximated. The electron density decays roughly exponentially after $t = 10$ [us], while decaying inversely with time during the period before 10 [us], as noted in [18]. From these types of decay, it was concluded that the early period was likely recombination-based power loss, while the latter period was diffusion-dominated. Although the latter interpretation is most likely true due to the near-constant late-period volume, the rapid increase in volume during the first 10 microseconds has not been accounted for. Multiplying the electron density with the volume yields the green curve in Figure 3.6a, which does not exhibit $\eta \propto t^{-1}$ dynamics but rather an exponential decrease that carries over into the late period. Therefore, the diffusion-dominated power loss is most likely dominant throughout the entire evolution of the plasma, in the form of heat conduction. The heat conduction power loss is provided in (1.54), and can be expressed in terms of the distance R (decay length) between two contours and ratio of the intensity between two contours by a conversion using (1.53d), using $I_2/I_1 = \eta_2/\eta_1$, and the approximation of the temperature at the boundary

of $T = 3000$ [K]:

$$\Delta T = (I_2/I_1 - 1)\frac{(T_2/T_1 - 1)}{\eta_2/\eta_1 - 1}|_{T\approx 3000\,[\mathrm{K}]} \cdot T \approx 0.2 \cdot 0.1 \cdot 3000\,[\mathrm{K}] = 60\,[\mathrm{K}]$$

With area $A \approx 60$ [mm^2], and $\nabla T = \partial T/\partial y = \Delta T/R = 3 \cdot 10^5$ [K/m]. Evaluation of (1.54) yields $P_l = 1 \cdot 10^{-4} \cdot 3 \cdot 10^5$ [W]$\approx$ 20 [W]. Supposing constant power loss over the plasma's significant temperature over the period of 60 [us], this would yield an energy loss of 1.2 [mJ], which is quite close to the order of magnitude of the initial thermal energy $U(t = 0) = 42$ [mJ].

3.3 LP radial electron density distribution $\eta(\rho)$

Although we will mostly deal with the LP as a domain with homogeneous properties, this does not accurately model the LP, in particular for the LP around cutoff in both the 2.45- and 57 GHz simulations. For this reason, we again assume $\eta \propto I$ in the CCD images, and derive the "cross-sectional" (cs) LP-electron-density $\eta(\rho)$ by studying the intensity $I(\rho)$ within the cs of the IAT-image. This cs-array is a circular sub-array of IAT, in terms of the larger array coordinates, center [$c + r(t)$,c] and radius $a(t)$ from (3.1a) resp. (3.1b). By a partition of the cs into radial $(\rho, \rho + d\rho)$ and angular $(\phi, \phi + d\phi)$ domains represented in Figure 3.8, computing the average value of I at every domain of the mask to characterize the distributions $I(\rho)$ and $I(\theta)$.

Determination of LP radial electron density distribution $\eta(\rho)$

When we plot the average intensities of the mask-domains over their corresponding radii ρ, we obtain the scattered data plotted in Figure 3.9a. The choice for the function used to fit the data will be explained.

When we plot the average intensities of the mask-domains over their corresponding radii ρ, we obtain the scattered data plotted in Figure 3.9a. The (scatter-plot) data indicate that the distribution over ρ is some power of a sine that elapses roughly half a period π between the cs-center $\rho = 0$ and the cs-outline $\rho = a(50) \approx 1.3$ mm. This leads us to the fit $I(\rho)$ to the spectrum (3.3).

$$I(\rho)|(a, \alpha) = A \cdot \sin^{\alpha}(\frac{\pi \cdot \rho}{a}) \tag{3.3}$$

Version of July 8, 2021– Created July 8, 2021 - 13:14

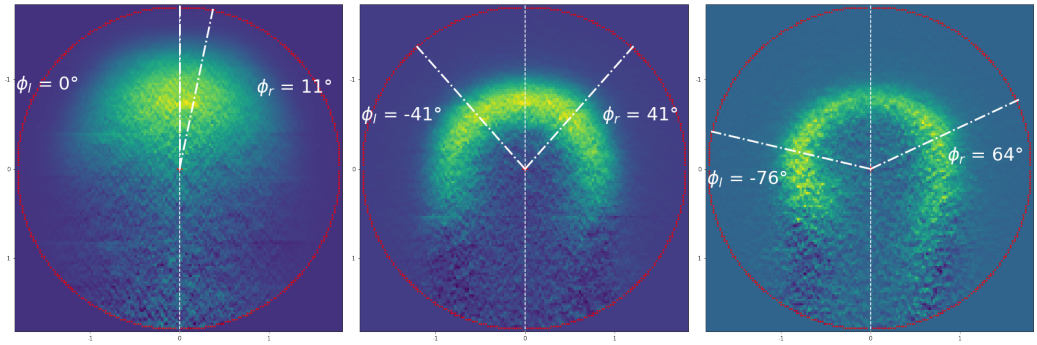

(a) *t=22 [μs]* **(b)** *t=34 [μs]* **(c)** *t=40 [μs]*

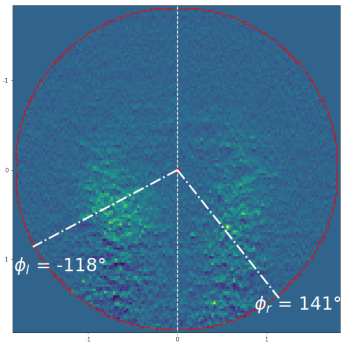

(d) *t=46 [μs]*

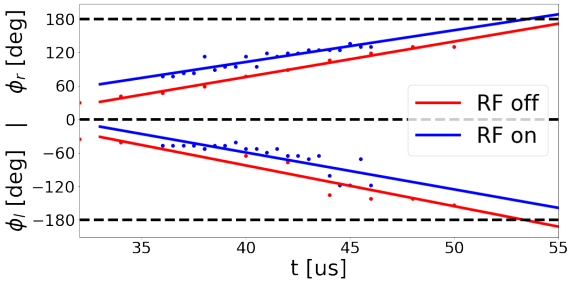

(e) *Angles ϕ_l and ϕ_r of maximum intensity along cross-section.*

Figure 3.7: *Intensity sub-arrays of the IAT-image, with size* 150×150 *[px²] centered on the toroidal cross-sectional (cs) center. At time t, the sub-array has time-dependent center-coordinate* $[c - r(t)[px], c]$*. Radial distance (red circle) from center coordinate consistently equals* $a(t = 48) \approx 1.56$ *[mm]* ~ 75 *[px], with zero-valued intensity outside. The angles ϕ_l and ϕ_r to the left resp. right of the vertical line indicate maximum total intensity within the cone* $[\phi \pm 3\circ, \phi \mp 3\circ]$*.*

Fitting this spectrum to the data for degrees of freedom α and a, we get the data represented as scatter-plot in Figure 3.9b. The parameter a in (3.3) relates to the position of the spectrum maximum $I(\rho = a/2) = A$. Substituting the parameter $\boldsymbol{a = a(t)}$ with previously-derived minor radius in (3.1b) provides good correspondence with the data. The other parameter is on average $\boldsymbol{\alpha = 4}$ over time, which provides the average distribution over $\alpha \in [1, 8]$. As a result, fixing of the DOFs $a = a(t)$ and $\alpha = 4$, with DOF A as fit parameter, (3.3) is plotted alongside the $I(\rho)$ spectra in Figure 3.9a, providing excellent correspondence with data on the cs-distribution.

Finally, the DOF A in the curve fits can be resolved as well by the dominance of radiant intensity from the LP corresponding to $I(t) \propto \eta_0(t)$ in (3.2a), under the premise of a homogeneous and time-independent decay-

Version of July 8, 2021– Created July 8, 2021 - 13:14

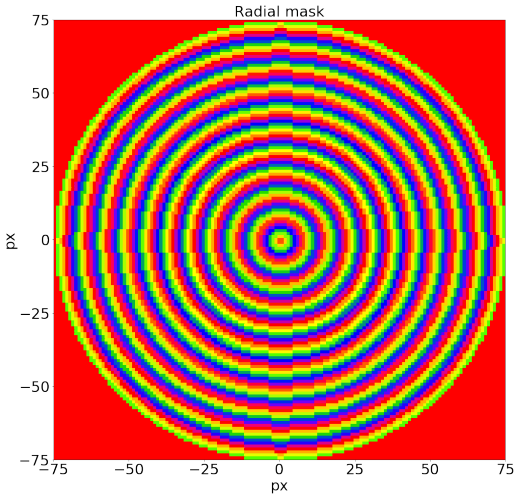

(a) *Radial mask of cross section. It segments into regions of similar cross-sectional radial distance ρ*

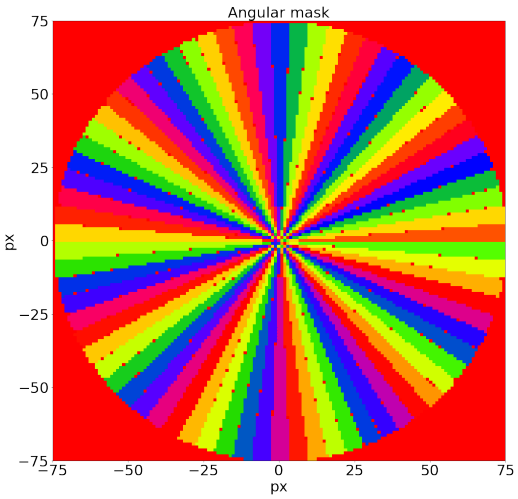

(b) *Angular mask of cross section. It segments into regions of similar angle ϕ*

Figure 3.8: *Masks used in determination of electron density distribution over their respective segmentation*

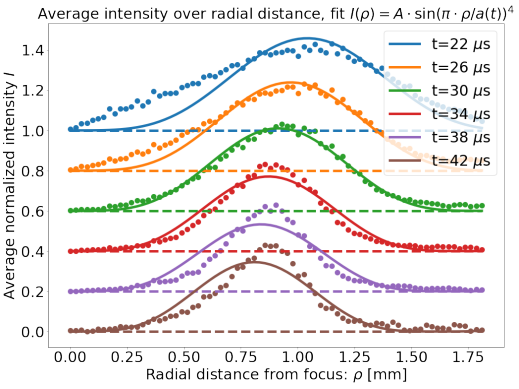

(a) *Intensity over radial distance. Spectra $k \in [0,5]$ normalized and translated within range $[0.2 \cdot k, 0.2 \cdot k + 0.2]$.*

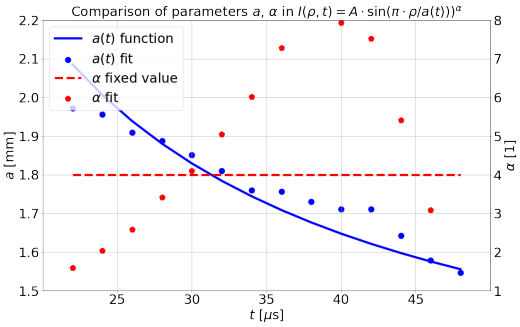

(b) *Fit parameters α and a over time*

Figure 3.9

constant τ_{LP}. One final amendment needs to be made as to the renormalization in converting from a homogeneous electron distribution $\eta(\rho) = const$ to a radial distribution $\eta(\rho) \propto \sin^4(\pi\rho/a)$. As can be seen from the appendix on toroidal coordinates, to retain an equal amount of total electrons under both homogeneous and $\sin^4$ distribution requires the renor-

malization factor factor 2.5. With that, we come to the LP cross-sectional electron density Ansatz (3.4).*

***Ansatz* for the non-homogeneous LP normalized electron density distribution η over ρ [mm] for time t in [μs].** $a(t)$ **from** (3.1b), $\eta_0(t)$ **from** (3.2)

$$\eta(\rho, t) = 2.5 \cdot \eta_0(t) \cdot \sin^4\left(\frac{\pi\rho}{a(t)}\right) \tag{3.4}$$

Determination of LP angular electron density distribution $\eta(\phi)$

A parameter over which η also varies but will not be implemented is the cross-sectional angle ϕ. A mask that segments the cross-section into angles is made, with the angle ϕ of the segment rotating counter-clockwise and with $\phi = 0$ at the point $(1, 0)$ in the complex plane. We can derive a polynomial periodic distribution that is therefore fitted to a sum of sines in the function (3.5).

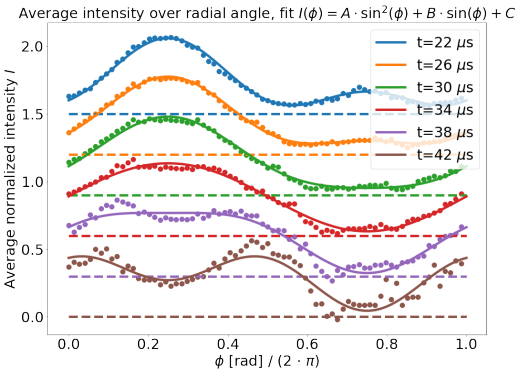

(a) *Intensity over angle*

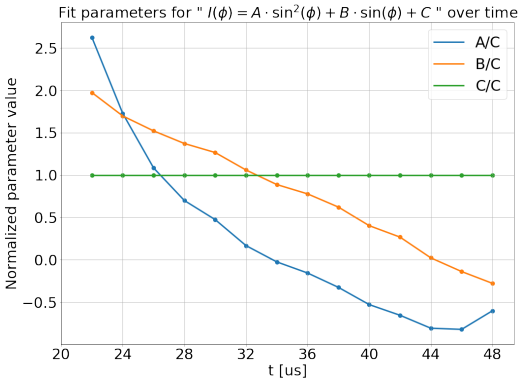

(b) *Angular intensity profile, fit parameters A, B, C over time*

Figure 3.10

*It is confusing to call the function an Ansatz since the only DOF to be determined in parametric sweeps is the OoM electron density constant c_{LP}, which is already embedded in $\eta_0(t)$ (3.2a). After fixing c_{LP}, we will however identify the necessity for adding some offset η_a to $\eta(\rho, t)$ in order to reproduce $Q(t)$. Due to the high gradient over ρ, parts of the lobes that are below cutoff $\eta(\rho \approx a) < 1$, are predominantly too small to cause losses by $\epsilon'' \frac{V_s}{V_0} \ll \frac{1}{Q_0}$. The offset η_a resolves this problem by boosting the power absorption into outer lobes of the $\sin^4$.

$$I(\phi) = A \cdot \sin^2(\phi) + B \cdot \sin(\phi) + C \tag{3.5}$$

The numerical values of the data, and the fit to the data with equation (3.5) are plotted in Figure 3.10a. However, this dependence of η on ϕ will not be implemented for two reasons. Firstly, examination of the distribution in Figure 3.10b gives the impression that the distribution varies radically over the examined time period [22,44] us; we cannot reliably extrapolate to times [44,60] where the distribution will have a larger impact. Secondly, for each separate t, a horribly complex re-normalization for this new distribution $\eta(\rho, \phi)$ would need to be made, at the risk of fallacies.

In conclusion, we conclude non-homogeneous distributions over both parameters ρ and ϕ, with only the distribution $\eta(\rho)$ to be finally implemented in simulation. Whereas $I(\rho)$ requires a near-constant single-DOF $\alpha(t) \approx 4$ distribution and its parameter ρ has a predictable effect on the response to RF-fields, $I(\phi)$ follows radically-dynamic triple-DOFs $(A, B, C)(t)$ and its parameter ϕ has an unpredictable response to RF-fields.

3.4 EC-geometry

Without RF-heating activated, CCD images on the plasma do not give any reliable indication of the presence of a plasma outside of the LP-domain. Namely, radiant intensity outside of the LP-domain (torus-outline (3.1), shown in middle-column of Figure 3.1) is much lower compared to intensity within the outline and might be attributable to aberration of the lens or charges that have diffused from the LP. Per illustration, setting zero-intensity to pixels within the outline, a "glow" remains as shown in the center column of Figure 3.2a, and is identified by steadily decreasing intensity over distance from the outline. The summation of all pixel-intensities outside of the LP-domain over time is given in Figure 3.12a, with labels *EC, RF off* and *EC, RF on* representing the total intensity without capacitive heating resp. with capacitive heating during $t \in [30, 100]$ [us]. Heating (*RF on*) is abruptly deactivated at $t = 100$ [us], and is visible as an abrupt decrease of the radiant intensity of LP- and EC-domain to their relative intensities under the absence of heating (*RF off*). The non-zero *noise-intensity* for LP- and EC-domain at $t \to \infty$ is most likely attributable to background-intensity from leakage of light from the laboratory-setting to the CCD-camera. The noise is homogeneous over the CCD-pixel-array, with unequal noise-intensity for LP- and EC-domain due to

unequal amount of pixels N within these domains: $I_{EC} : I_{LP} \sim N_{EC} : N_{LP} \sim 512^2 - (2r) \cdot (2a) + \pi a^2 : (2r) \cdot (2a) + \pi a^2 \sim 4 : 1$.

Under the absence of heating, the EC-intensity stagnates at $t = 45$ [us] to logarithmic *Signal-to-Noise-Ratio* $\sim SNR_{dB} = 0$. Under heating, in contrast, the EC-intensity decreases more slowly beyond $t = 30$ [us], with intensity maintained beyond $t = 45$ [us] at one order of magnitude above background-intensity.

Upon studying IAT CCD images of the plasma under capacitive heating in Figure 3.11, intensity outside of the LP domain can be identified in two region types, with both types present at either side ($w \in \{[c - a - h, c - a], [c + a, c + a + h]\}$) of the LP, in terms of center $c = 256$ [px] and approximate horizontal height $h = 41.45$ [px]. A first ring-shape structure with inner and outer radius $a_1 = 1.5$ resp. $a_2 = 2.5$ mm, that is luminous between 36 and 50 [us]. A second ring-shape structure with inner and outer radius $a_3 = 3.75$ resp. $a_4 = 4.75$ [mm], that is luminous from 40 [us] until magnetron shut-off at 100 [us]. The intensity within these regions indicate the presence of significant electron density within, classifying as plasma.

Independence of EC on capacitive heating

Before asserting this as the definitive EC-geometry, we need to justify that the geometry observed under capacitive heating is not an artifact of heating only. Namely, under the presence of an (absorbing) LP only, capacitive heating leads to ambipolar diffusion: charges are torn from the LP and diffuse outside of its domain. This would form plasma near the outline of the LP that becomes luminous under heating, similar to what is (possibly wrongly) identified as a pre-existing *EC*.[†] In order to prove that these luminous regions are pre-existing (read: formed by the laser-pulse), we require evidence that the luminous regions are independent from: (i) capacitive heating in general, (ii) from nearby induced current density within the LP, and (iii) from the local electric field magnitude.

Firstly, the quality factor $Q(t)$ in Figure 2.2a provides evidence for a composite plasma, the two components of which simultaneously decay. The quality factor is based on power-reflection measurements, where no heating was applied; the composite LI-plasma decays unperturbed. The low quality factor before $t = 35$ [us] indicates that some resistive domain is pre-existing. The likely candidate for this resistive domain is the EC-

[†]Credit goes to Vincent Kooij bringing this up.

Version of July 8, 2021– Created July 8, 2021 - 13:14

domain in CCD-images indicated by the excess intensity for *EC* beyond $t = 30$ [us] in Figure 3.12a, associated with the luminosity within the boxes of Figure 3.11. Additionally, subsequent quality factor reduction beyond $t = 42$ [us] indicates that there must be some highly conductive domain that is beyond cutoff. The likely candidate for this conductive domain is the LP-domain in CCD-images indicated by excess intensity for *LP* beyond $t = 45$ [us], associated with the luminosity within the outline of Figure 3.11. We may therefore conclude that the EC is a pre-existing domain below cutoff, and the LP is a torus shape that is beyond cutoff.

Secondly, by the fact that the LP is beyond cutoff, the nearby Electric field magnitude is perturbed as visible from Figure 2.5a. By (1.4a) induced current density within the LP is situated at parts of its surface parallel with the E-field, next to low E-field magnitude. This possibly causes the formation of charges, identified as luminosity in the outer cylinders at $t \in \{36, 38, 40\}$ [us] Figure 3.11. However, this does no explain the presence of the inner cylinders, because no nearby (absorbing) regions of the LP are present. Moreover, ambipolar diffusion and power absorption by the LP are negligible, to be proven later in section 4.3 resp. Figure 4.7.

Thirdly, the location of the Electric field magnitude in Figure 2.5a cannot be reconciled with the stationary properties of the luminous EC-regions. The regions of luminosity remain roughly static, whereas the high E-field magnitudes move outward, along with r.

Relation of the EC with flow-simulations

The inner radius of the luminous inner EC-rings in Figure 3.11 $t \in \{36, 38, 40\}$ [us] coincides with the radius of an inward moving, "self-piercing" shock-front concluded from flow simulations on the torus-formation in [18, Figure 4.9] with radius $\mathcal{R} \approx 1.5$ [mm] $= a_1$. The high temperature of the laser-kernel causes its expansion from the rough initial condition of a spherocylinder (which is a union of a cylinder and two hemispheres axisymmetric with the circular boundaries at either end, all objects having equal radius). Assuming homogeneous initial pressure, outward expansion along the entire surface leads to loss of shock-front-energy; the spherical expansion is more energy-intensive, leading to (near-simultaneous) collapse of the shock front on either end while cylindrical expansion continues. The two shock-fronts simultaneously meet at the initial location of the laser-focus, creating the torus-topology. The near-equal momentum of the collapsing fronts leads to a net circular "splitting" shock-front expanding radially outward into the torus, creating the crescent-shape. Although the simulation assumes equal energy deposition on either side of the focal

point, higher energy deposition closer to the laser is more plausible because of the laser-intensity decaying along the beam's path. Consequently, unequal collapsing shock-front energy creates a net counter-clockwise vorticity identifiable for the LP in Figure 3.11(a,b,c), as well as a net draft from left to right. The cold gas dragged behind the collapsing shock-fronts with radius $\mathcal{R} \approx 1.5$ [mm] $= a_1$ would explain displacement of charges within $R < a_1$, and their deposition in the surrounding region $a_1 < R < a_2$.

As a side note: future implementations of the EC-characterization are focused on reliably proving that no power absorption takes place within the EC under inductive heating, where power absorption favours high conductivity. By CPT (1.26b), under constant quality factor, a decrease in sample volume implies an increased electron density and thereby an increased conductivity. Although the EC-geometry does not include all radiant-intensity outside of the LP-domain, the use of this minimalistic geometry will provide an upper limit for the EC-conductivity. This will allow us to rule out power absorption by the EC under inductive heating, later on.

Another noteworthy remark: by Figure 3.11(d,e,f), the majority of EC-intensity - and thereby the majority of power absorption - originates from the outer cylinders for $t \geq 50$ [us]. Naively, this would indicate non-homogeneous η. However, assigning homogeneous η across the EC-domain remains realistic by Figure 2.5a; the field at the inner cylinders is negated because $r(t \geq 50) \gg a_2$. Simulations on the homogeneous EC near beyond-cutoff-LP reproduce this principle, visible in the right column of Figure 3.1.

The EC-geometry described above is formalized in (3.6). Here $\sigma(x)$ is the sign function with parametrization $\sigma(x) = -1, x \leq 0$ and $\sigma(x) = 1, x > 0$. Over R, $f(R) = 1$ for $a_1 < R < a_2$ and $a_3 < R < a_4$, whereas $f(R) = 0$ elsewhere.

EC geometry in terms of laser-axis radius R in [mm] and distance from focal plane h in [mm], and t in [us]

$$\eta'(R,h) = \eta'_0(R,h) \cdot f(R,h) = f(h) \cdot f(R)$$

$$\text{Optional: } f(h) = 1 + \frac{1}{2} \cdot [\sigma(|h| - a(t)) \cdot \sigma(-|h| + a(t) + 1[\text{mm}])] \tag{3.6a}$$

$$f(R) = 1 + \frac{1}{2} \cdot [\sigma(R - a_1) \cdot \sigma(-R + a_2) + \sigma(R - a_3) \cdot \sigma(-R + a_4)] \tag{3.6b}$$

$$(a_1, a_2, a_3, a_4) = (1.5, 2.5, 3.75, 4.75) \tag{3.6c}$$

$V_s = 50\ \text{mm}^3$, Effective EC volume; volume of outer cylinders

Topological definition of the EC in simulations

The definition of the EC-geometry in (3.6) is made in a block-function form because of the inconvenience of implementing a cylindrical shape in simulations. Whereas the EC-domain is static, the LP domain undergoes many changes, as seen in (3.1a) and (3.1b). The close proximity of the LP and EC implies that their interface boundaries may overlap or leave tiny gaps, all of which causes complications with the meshing. For this reason, the EC-domain is implemented in simulations as a coordinate-wise Boolean of material properties. For $f(R) = 1$, EC material properties are assigned, whereas for $f(R) = 0$ free-space material properties are assigned. It is applied to the *shell*-topology explained below.

The EC-geometry can be defined as a topological combination of four axisymmetric objects - two toruses and two cylinders. Each point on the EC's outer boundary has a distance of 1 mm from the closest point on either (i) the outer boundary of the LP torus with major/minor radius r/a or (ii) the outer boundary of the LP-concentric cylinder with radius r and height $2 \cdot a(t)$. The inner boundary of the EC domain is equal to the outer boundary of the union of objects (i) and (ii). The EC-geometry thus defined is equivalent to the union of (iii) a torus with $(r, (a + 1))$, and (iv) a LP-concentric cylinder with $(r, 2 \cdot (a + 1))$, subtracted by the union of (i) and (ii). The entity thus created acts like a one-mm-thick *shell* around the LP-torus for $R \geq r(t)$, but with flat circular shape for $R < r(t)$. Within the this EC-domain, the electron density is limited to four cylinders, two on either side by the material function (3.6).

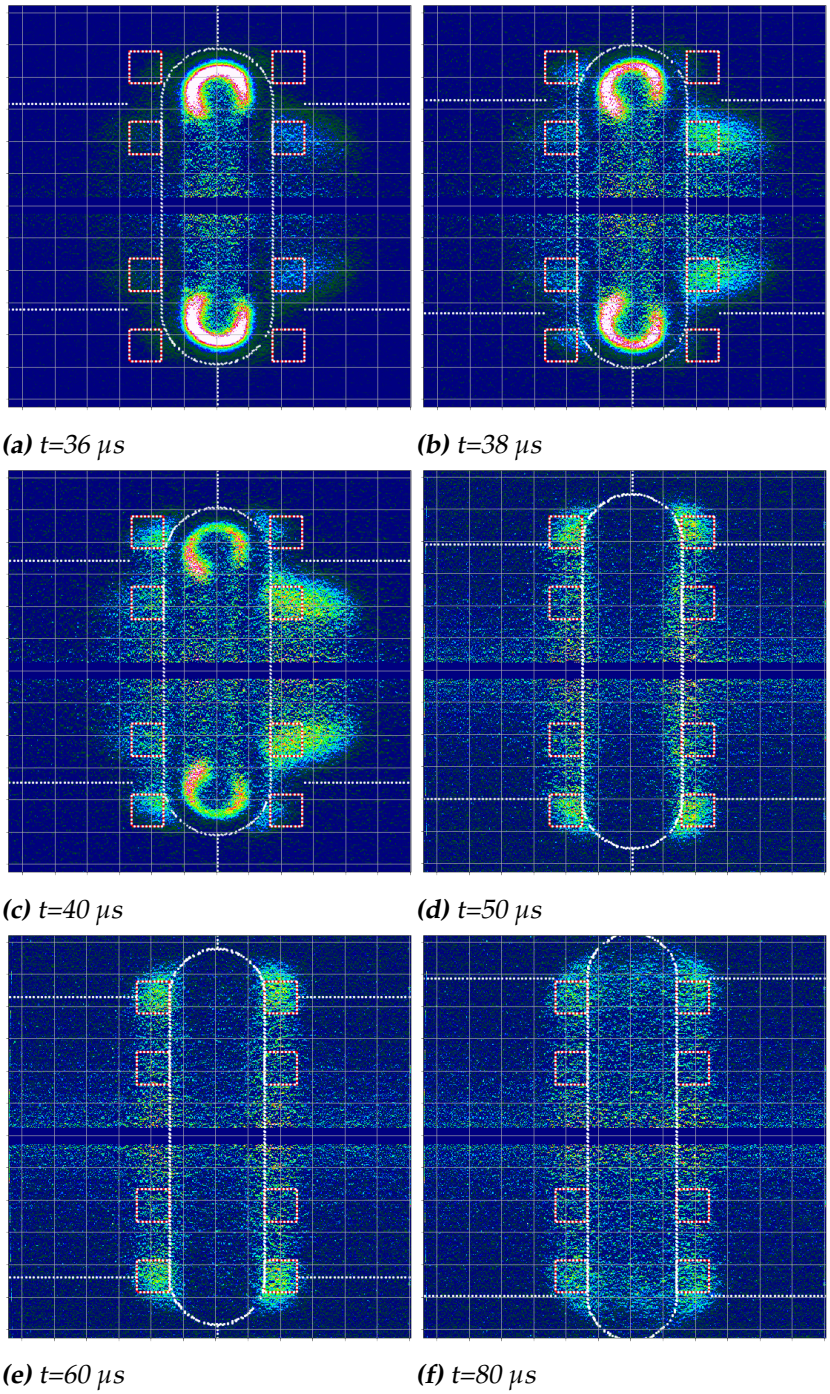

(a) *t=36 μs* ***(b)*** *t=38 μs*

(c) *t=40 μs* ***(d)*** *t=50 μs*

(e) *t=60 μs* ***(f)*** *t=80 μs*

Figure 3.11: *IAT CCD images under capacitive RF heating. Boxes in red-white indicate outline of the EC cross-section in* (3.6)*. Data-sets: zmage-17382 RF 35-46 us step 0.5 20 avg gain 250 gate 500ns yields (a-c), zmage-17679 yields (d-f).*

3.5 Total intensity of LP and EC under RF-heating

The CCD images of the plasma under RF-radiation have exposed different behaviour for LP and EC. There is an increase/stability of luminosity for the EC beyond 45 us, and for the LP beyond 60/70 us. This indicates that the RF power absorption attains the magnitude of power loss at different times $t_{s,EC}$ and $t_{s,LP}$ for EC resp. LP. They can be studied separately and compared, by a dichotomy of the CCD image in their associated domains through the torus-outline, corresponding to the geometry in (3.1a) and (3.1b).

Our theory assumes that the intensity I of a region in the CCD image is proportional to the power loss P_l in that region. Therefore, if the plasma-specific intensity remains stable, the power loss P_l radiated by the plasma-component must be equal to the power absorption P_a in that component, and therefore a stable intensity I reflects plasma stability $P_a = P_l$. It is evident that the EC is stable beyond $t_{s,EC} = 45$ us. The LP intensity starts increasing at $t = 60$ us and stabilizes at $t = 75$ us.

The torus-outline presents a sharp cut at the LP and EC interface that inescapably assigns some EC radiant intensity to the LP. Around minimum LP-intensity under RF-heating, $I_{LP}(t \in [50, 60])$, the noise-like LP-intensity without RF-heating is exceeded by a factor ten. This minimum intensity is most likely attributable to the EC, and therefore LP stability must correspond to the end of the intensity-increase: $t_{s,LP} = 75$ [us].

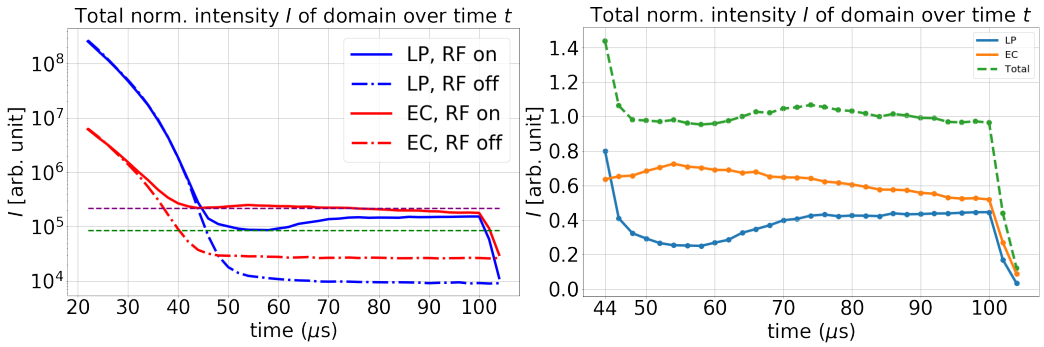

(a) *Normalized intensity over time, RF on and RF off compared.*

(b) *Normalized intensity over time, starting just before LP-equilibrium*

Figure 3.12: *Total intensity over time, over LP- and EC-domain, with and without heating, of the raw CCD images. The LP-intensity is the sum of pixel-intensities within the torus-outline, and the EC-intensity is the sum of intensity over all pixels outside of the outline.*

Version of July 8, 2021– Created July 8, 2021 - 13:14

Chapter 4

Characterization of capacitive plasma heating

This chapter will determine the dynamic material properties of the two components of the plasma: LP and EC. Characterization is made by reproduction of experimental from the presence of the LI-plasma at the E-field antinode of the rectangular TE_{101} cavity. The dynamic characterization of the plasma is made for $t \in [30, 60]$ us after the laser-pulse. Afterwards, based on these material properties, the efficiency of capacitive heating of the plasma at each time will be investigated.

Firstly, under the assumption of homogeneous material properties, we will theoretically determine the material properties of both plasma- components. This is accomplished by solving the formulae (1.52a) and (1.52b) to follow experimental measurements in Figure 2.2a. Degrees of freedom are eliminated by applying steady exponential decay of η; Ansatz (3.2) for (c_{LP}, τ_{LP}) and (c_{EC}, τ_{EC}).

Secondly, under assumption of non-homogeneous material properties, we will simulation-wise determine the material properties of the plasma-components. This is accomplished by implementation of Ansatz (3.4) to the LP-domain, and subsequent parametric sweep of c_{LP} and γ_{LP} to follow experimental measurements of Figure 2.2a as well as Figure 2.2b.

Lastly, the material properties deduced through the simulation-wise characterization are implemented in the capacitive heating model of Figure 2.3. Under this unperturbed plasma-decay characterization over $t \in [30, 60]$, the efficiency of RF-power absorption is determined by analysis of the share of power absorption into LP- and EC-domain and the reflected power.

Version of July 8, 2021– Created July 8, 2021 - 13:14

4.1 Characterization of the homogeneous composite plasma

The goal of this section is to characterize the LP and EC under the assumption that they possess homogeneous material properties η and γ.

Firstly, a simulation-wise investigation is made of the response of cavity RF-properties Δf and Q to the presence of a **LP-torus** at the center of the cavity in Figure 2.3. For $\sigma \to \infty$ a variation of its geometric properties around $(r, a)(t \approx 45\,\text{us})$ is used to verify (1.33a). For $(r, a)(t \approx 45\,\text{us})$, a variation of its the material property $\eta \approx 1$ around cutoff is used to verify (1.52a) and (1.52b) under existence of LP only $(\eta, \gamma, V, p)_\alpha = (0, 0, 0, 0)$.

Secondly, an order of magnitude estimate of the dynamic material properties of the EC is made by inferring from the 2.45 GHz data for (1.26b).

Lastly, a dynamic characterization $(c[\cdot\eta],\ \gamma,\ \tau)_\alpha$ by combining the simultaneous LP and EC decays under (1.52a) and (1.52b) and resolving remaining degrees of freedom for the material properties.

4.1.1 Characterization of the LP

This subsection fully focuses on the effects of the LP in both simulation and theory. By comparison of simulation data with evaluation of the theoretical formulae for the simulation parameters, we verify the validity of equations (1.33a), (1.52a), and (1.52b).

Frequency shift due to presence of conductive torus

We know from (1.33a) that a downward frequency shift from the plasma is caused by the presence of an object within the cavity that is beyond cutoff. Almost the entire frequency shift is caused by the LP, which is conductive.* We have already accurately determined the major radius over time $r(t)$ found in (3.1a). The minor radius $a(t)$, however, could not be determined accurately, as seen in (3.4b) and (3.3). In order to ensure constant frequency shift $\Delta f \approx 5.7$ MHz, the final equation for $a(t)$ (3.1b) has been postulated such that - under (1.33a) - constant volume $V_s = 180\ \text{mm}^3$ is kept under growing major radius $r(t)$.

In order to verify the validity of equation (1.33a) and therefore also the validity of the formula for the minor radius (3.1b), a simulation-wise sweep of a is made under r for different t around the presumed LP-volume

*Another cause of the frequency shift might be the EC. However, the low impact of the EC will be proven independently in the next subsection.

Version of July 8, 2021– Created July 8, 2021 - 13:14

$V_s = 180\ \text{mm}^3$. The torus is implemented at the center of the cavity in Figure 2.3 with infinite conductivity, and the above sweep of values a and r delvers the data visualized in Figure 4.1b. From the figure, we determine that the frequency shift remains at $\Delta f \approx -5.7$ MHz for a torus volume of $V_s = 180\ \text{mm}^3$. This must thus be the volume of the LP, and it is thus correctly implemented for the formula of $a(t)$ (3.1b).

As a matter of reflection, we visualize the corresponding torus-size by implementation of the torus-outline corresponding to (3.1a) and (3.1b) in CCD images. This is done in Figure 3.1 and in Figure 3.11, with the latter providing the interesting information about luminosity under RF-heating. The torus-outline consistently touches the outer edge of the dark region in between the luminous regions. The fact that a region of the CCD image can be dark yet be beyond cutoff indicates that the radiant intensity is not necessarily indicative of a high electron density. Although this will only become relevant later, it alludes to the possibility that the electron density in the outer regions of the non-homogeneous LP $\eta(\rho)$ distribution in (3.4) is underestimated. We will eventually recognize the necessity of raising $\eta(\rho)$ by some offset η_a.

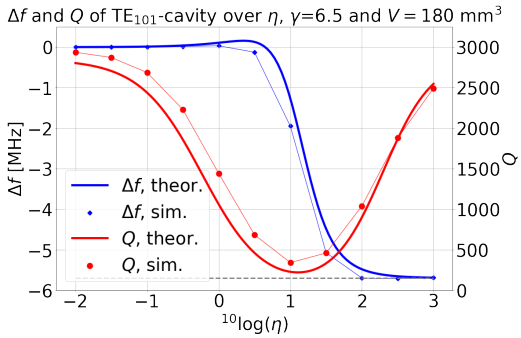

(a) *Total system quality factor and frequency shift over η for a homogeneous toroidal plasma with $\gamma = 6.5$, $(r, a) = (3.75, 1.58)$ [mm] at the center of the TE-101 cavity. Simulation-data named sim., theoretical estimation theor. from* (1.52a) *and* (1.52b).

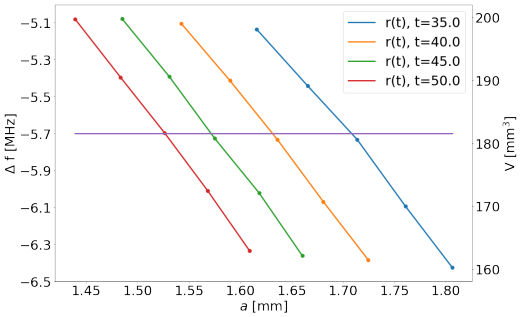

(b) *Frequency shift from LP beyond cut-off over volume. The vertical axis on the right is not exact! It is only a representation of the five volumes swept over for the four major radii.*

Figure 4.1

Frequency shift and quality factor reduction due to presence of torus near cutoff

In order to verify equations (1.52a) and (1.52b), it is useful to test these by comparison with simulations on the torus with material properties around cutoff ($\eta \approx 1$). Under 2.45 GHz measurements, the electron density decays exponentially over (possibly) multiple orders of magnitude, while the collision frequency changes over at most an order of magnitude by Table 1.3. Therefore, we assume room temperature $\gamma = 6.5$ and constant geometry $(r, a)(t = 45\,\text{us}) = (3.75, 1.58)$ for the torus and make a sweep of η for multiple orders of magnitude. The resulting material dielectric properties (from (1.39a) and (1.39b)) $(\epsilon_r', \epsilon_r'')$ are then implemented for the material properties of the toroidal domain, the field under RF-excitation is computed for *dielectric loss*-wave equations, from which finally the frequency shift and quality factor of the cavity are then extracted.

The resulting simulated data is visualized as the scatter-plots in Figure 4.1a as "*sim.*". As for the theory, the same sample properties $\eta \in [1e-2, 1e3]$, $\gamma = 6.5$, $V_s = 180$ mm^3, and $a = 1.58$ mm are implemented in formulae (1.52a) and (1.52b), and their evaluations are plotted alongside the simulation data in line-form as "*theor.*". We identify good accordance of theory with simulations.

As a side note, we see that the upward frequency shift ($\eta \approx 0.5$) pales in comparison to the downward frequency shift ($\eta > 0.5$) . This makes it alluring to simplify equation (1.52a) by setting the upward frequency shift equal to zero. However, this severely decreases the gradient of the frequency shift transition around cutoff, which might lead us to wrongly underestimate the decay constant τ per compensation. Therefore, the upward frequency shift due to $\Delta\epsilon_r'$ is an essential component in accurately determining the plasma characterization parameters and needs to be maintained in formulae.

4.1.2 Characterization of the EC

This subsection fully focuses on the effects of the EC on the RF-properties of the cavity. This mostly deals with the quality factor reduction due to power absorption, which is briefly gone through.

Field-amplification and -negation within the EC-domain

We have seen from simulation on a torus beyond cutoff in Figure 2.5a that the electric field amplitude distribution, and consequently the elec-

tric field energy density near the torus is perturbed. The EC is situated within a distance of 1 mm of the LP. Therefore, at some coordinate within the EC-domain, if $R \ll r(t)$ the field is negated and if $R \approx r(t)$ the field is amplified. These two cases lead to reduced resp. increased power absorption into the plasma, and the consequent influence on Q must thus be taken into account in determining ϵ_r'' of the EC. We know from (3.6) that electron density is mostly situated in two bands with $1.5 < R < 2.5$ mm and $3.75 < R < 4.75$ mm. As for the positions of amplified E-field, we know from (3.1a) that over the range $t \in [30, 60]$ us, $< r >_t \approx$ 3.6 mm. This time-averaged major radius corresponds with a net field amplification in the outer ring of the EC and a net field negation in the inner ring of the EC. For the reason of field negation into the inner rings, we approximate the effective volume of the EC as the volume of the outer cylinders only, such that $V_s \approx 50$ mm^3, already mentioned in (3.6). As for the field amplification visible in Figure 2.5a, this can be as high as a factor 2, corresponding with an energy density amplification of a factor 4. To account for the shifting position of the field amplification $r(t)$, and to account for the decreasing energy density away from the torus boundary, we average the field amplification at a factor $\sqrt{2}$ corresponding with energy amplification at a factor 2 for the outer EC domain. This is already implemented in (1.52c) for the EC-sample $\alpha = 2$.

Approximation of decay-Ansatz-parameters c_{EC} and τ_{EC}

The imaginary part of the relative permittivity, ϵ_r'', can be determined directly from the total system quality factor using (1.26b) with $V_s = 50$ mm^3. To account for the field-energy amplification (factor 2), the evaluated ϵ_r'' is divided by two a posteriori.

Before the quality factor is significantly influenced by the LP (around the peak at $t = 42$ us) the quality factor of the system rises due to recombination within the EC. From Figure 2.2a, $Q(t = 30us) = 400$ and $Q(t = 40us) \approx 700$. Inserting both values in the formula (1.26b) and dividing by field amplification factor (2), we get: $\epsilon_{r,EC}''(t = 30us) \approx 1.6$, and $\epsilon_{r,EC}''(t = 40us) = 0.8$. For the Ansatz of the EC decay of electron density (3.2b), we infer for a cold EC $\gamma = 6.5$:

$$c_{EC} = \eta_{EC}(t = 30 \text{ us}) = \frac{\eta \cdot \gamma}{1 + \gamma^2} \approx 11$$

From the gradient of ϵ_r'', which is also the gradient for η under constant γ, we can determine the decay constant τ_{EC} using (3.2b). The factor $1/2$

decrease over a 10 us time-span yields:

$$\tau_{EC} = \frac{-10}{\ln(1/2)} \approx 15 \text{ us}$$

4.1.3 Dynamic characterization of homogeneous plasma

We can now finalize the characterization of the homogeneous plasma by implementing the above Ansatz-parameters for the LP and EC samples in (1.52a) and (1.52b). At any point in time, these equations require for both the LP and EC the following DOF-parameters: (η, γ, V). The parameter of the LP- and EC-sample volume V is already known in (3.1) and (3.6). The two remaining parameters for both components are to be determined from simulations: $(\eta_{LP}, \gamma_{LP}, \eta_{EC}, \gamma_{EC})$, all of which are reasonably approximated - for $t \approx 45$ us - to be close to:

$(540 \cdot c_{LP} = 540, \gamma(T = 3000 \text{ K}) = 2.5, c_{EC} \cdot \exp(-15/\tau_{EC}) = 4, \gamma(T = 300 \text{ K}) = 6.5)$

This raises the following issue.

Suppose for the moment that we do not know the dynamics Q and Δf nor the exponential decay of η; we are only given the values Q and Δf caused by the composite plasma at a single point in time t'. We cannot resolve the four degrees of freedom embedded in the plasma-parameters $(\eta, \gamma)_{LP,EC}(t')$ from two values of measurement data $Q(t')$ and $\Delta f(t')$. This exposes the necessity for having postulated the Ansatz (3.2) and the knowledge of the full time range of data of Q and Δf. Under the assumption of exponential decay and its Ansatz, the DOF $\eta(t)$ requires two DOFs τ and c. Although adding two more degrees of freedom $\tau_{LP,EC}$ seems like a step in the wrong direction, these parameter-values will allow us to extrapolate for the full range t, which will now be done.

The objective: we require the determination of the parameters: (η_{LP}, τ_{LP}, γ_{LP}, η_{EC}, τ_{EC}, γ_{EC}) from the Ansatz formulae (3.2) with constant γ_{LP} and γ_{EC} such that reproduction of Figure 2.2a is accomplished upon implementation in (1.52a) and (1.52b).

By identifying that the dynamics of Q for $t \in [30, 40]$ us is dominated by the EC, we have already deduced c_{EC} and τ_{EC}. Similarly, we can apply this strategy to deduce LP-parameters using constraints:

$Q_{LP}(t = 42) \approx Q_{EC}(t = 42)$,
$Q(t = 60) \approx Q_{LP}(t = 60)$,
$d/dt\ Q_{LP}(t = 60) = 60$.

Version of July 8, 2021– Created July 8, 2021 - 13:14

We could then solve the equations (1.52a) and (1.52b) to resolve any remaining DOFs, but these equations are monstrosities. Therefore the equations have been implemented numerically in *Python*, and a fit to measurement data is made under a parametric sweep of the six parameters. Trial and error eventually yielded the good fit in Figure 4.2, the parameters of which are presented in Table 4.1.

	LP theor.	EC theor.		LP sim.	EC sim.
c	0.21	5.5		3	3.67
τ [us]	9	10		4	15
γ	6.5	5		2.5	4
V_s [mm^3] (constraint)	180	50		″	″

Table 4.1: *Parameters of LP and EC that provide reproduction of 2.45 GHz measurement data for implementation in* (1.52a) *and* (1.52b) *with constant decay under* (3.2)*.*

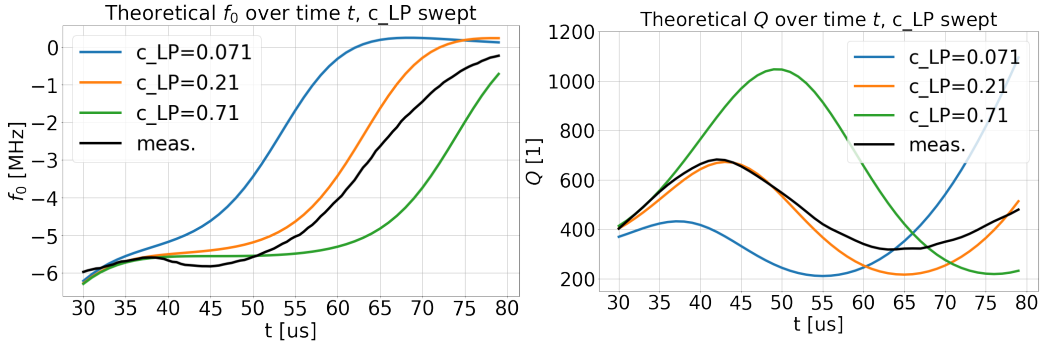

(a) ***(b)***

Figure 4.2: *Theoretical frequency shift and quality factor over time, compared to experimental data of the 2.45 GHz capacitive setup. Parameters are represented in Table 4.1, and are swept over some deviating c_{LP}. Parameters are implemented in* (1.52a) *and* (1.52b)*, with η produced from c and τ in* (3.2)*. The measurement data are represented with meas.*

Some remarks about the theoretical model

The above theoretical model of the plasma influences on f_0 and Q has some short-comings.

Version of July 8, 2021– Created July 8, 2021 - 13:14

Firstly, the model is constructed for homogeneous material properties of the plasma, whereas cross-sectional CCD-image analysis have indicated a non-homogeneous LP- normalized electron density distribution over cross-sectional radial direction $\eta(\rho)$ in (3.4). Implementing this $\eta(\rho)$-distribution in theory would require segmenting the torus cross-section into radial shells of infinitesimal thickness $d\rho$, and computing the infinitesimal transmission $d|T|^2$ and attenuation $\exp(-d\rho/\delta(\eta))$. However, this would be so complex that we are better off relying on simulations only when implementing the radial distribution.

Secondly, the implementation of material homogeneity of the LP cannot possibly reproduce the measurement data. By (1.52b) with $\gamma = 6.5$, the model necessarily leads to a minimum quality factor $Q \approx 200$ caused by the LP; this is endemic to its homogeneous nature and cannot be circumvented. Moreover, the low gradient of $\Delta f(t)$ and $Q(t)$ can only be reproduced for very high LP decay constant $\tau_{LP} = 9$ [us] $\gg 4$ [us], as found from CCD-image intensity decay in Figure 3.6a. These two issues are solved simultaneously upon implementation of the non-homogeneous distribution $\eta(\rho)$ in (3.4). The endemic property of such a distribution is that near $t \in [40, 50]$ us the shallow tails at $(\rho = a)$ are well below cutoff, while the peak at $(\rho = a/2)$ is well beyond cutoff; with two consequences.

With respect to the homogeneous distribution with same τ, the non-homogeneous distribution will imply a lower gradients $d/dt\ Q$ and $d/dt\ \Delta f$. Instead of the entire LP-domain absorbing optimally all at once, the power absorption gradually shifts from $\rho = a$ to $\rho = a/2$. Likewise, this non-simultaneous decrease below cutoff leads to a more gradual gradient of Δf.

Examination of the electron density distribution $\eta(\rho) \propto \sin^4(\rho \cdot \pi/a)$ yields a large simultaneous difference in the magnitude at $(\rho = a)$ with respect to $(\rho = a/2)$. Supposing optimal power absorption near electron density at cutoff density $\eta_{opt} = 1$ for a volume element. Peak-value η_{opt} implies low absorption at the edges which act like free space $\eta \ll 1$. Edge-value η_{opt} implies low absorption at the peak which acts like a good conductor $\eta \gg 1$.

We thus conclude that the implementation of non-homogeneous material properties of the LP is a necessary condition for the reproduction of measurement data.

Version of July 8, 2021– Created July 8, 2021 - 13:14

4.2 Characterization of the non-homogeneous composite plasma

In transitioning to the non-homogeneous plasma, we will apply non- homogeneous properties only to the normalized LP electron density distribution $\eta_{LP}(\rho)$. The remaining material-parameters η_{EC}, γ_{LP}, and γ_{EC} will be presumed homogeneous and constant. The latter will be justified shortly.

Simulations will be made under the model in Figure 2.3, which (like the 2.45 GHz measurement setup) is matched when empty with corresponding $Q = 2850$. The LP-geometry is a torus with major radius $r(t)$ and minor radius $a(t)$ given in (3.1a) resp. (3.1b). The material properties within LP and EC are determined by corresponding γ and η, yielding complex permittivity (1.39a) and (1.39b) for which the field is computed from the "*dielectric loss*"-wave equations in simulations. The resulting Q and f is extracted as data. The normalized collision frequency γ is homogeneous over the plasma. The normalized collision frequency $\eta(\rho)$ is a sine to the power four distribution that elapses half a period from $\rho = 0$ (the center of the torus cross-section) to $\rho = a$ (the edge of the torus cross-section) as argued in (3.4).

Justification for homogeneous γ

The normalized collision frequency is determined from the LP temperature T. The temperature of the unperturbed plasma for $t = 30$ [us] roughly equals $T = 3000$ [K] by Figure 3.6b, finding accordance both under spectrometry- and simulation data values. If we extrapolate the temperature decay above, temperatures may drop well below $T = 3000$ K for $t \in [30, 60]$ us. However, spectral emission measurements by both [24] and [19] discredit this. Most importantly, by [19, figure 5.9], spectral emission measurements indicate (electron) temperatures as high as $T_e = 5000$ K.[†] The figure also shows a non-homogeneous distribution of temperature over a crescent-shape similar to the intensity profile found from CCD images in Figure 3.7.

The remarks indicate many possible sources of error if we implement γ as non-homogeneous or time-dependent; whether to use the electron temperature or the gas temperature for implementation in (1.36b), and

[†]Electron temperature is expected at least one order of magnitude higher than the gas temperature, making the steep gas temperature decay suggested by flow simulations plausible.

Version of July 8, 2021– Created July 8, 2021 - 13:14

what temperature decay to expect. Whatever the resolution to these issues, the resulting deviations of $\gamma \in [1, 6.5]$ for all possible gas temperatures $T \in [10^4, 300]$ [K] would be small compared to the steep exponential decay of $\eta \in [540 \cdot 10^{-15/4}, 540 \cdot 10^{15/4}]$, justifying a loose approach to γ. Therefore, the normalized collision frequency γ is assumed to be a constant, and assumed to be homogeneous across the sample.

Preliminary characterization of EC

For the geometric properties in the simulation-model, we use the formulae for LP major/minor radius in (3.1a) and (3.1b), and the constant geometry of EC cylinders as a block function on a geometry occupying 1 mm around the LP, as explained in (3.6).

Beforehand, the properties of the EC are constrained by the assumption of the LP well beyond cutoff at $t = 30$ us. Thus, simulations have been made on an LP entirely beyond cutoff upon which η_{EC}, τ_{EC}, and γ_{EC} are swept to reproduce the values of Δf and Q for t between 30 us and 40 us. Reconciliation of the simulation data with both measurement data could only be made under $\gamma_{EC} = 4$. The right gradient of $Q(t)$ could only be achieved by taking $\tau_{EC} = 15$ us. Finally, the frequency shift at $t = 30$ us of an additional -0.3 MHz with value $Q = 400$ could only be reproduced by taking $\eta_{EC} = 1.35$.

EC material properties in terms of axial radius R in [mm] and time t in [us], applied to shell-topology

$$\eta'(R, t) = \eta'_0(t) \cdot f(R) \tag{4.1a}$$

$$\eta'_0(t) = 1.35 \cdot \exp(-(t - 45)/15) \tag{4.1b}$$

$$\gamma_{EC} = 4 \tag{4.1c}$$

4.2.1 Ansatz- and data comparison for 2.45 GHz

On the equations for the plasma material properties in equation (4.2), two parameters are swept.

Firstly, the LP electron density over half orders of magnitude with a sweep factor $\mathbf{c_{LP}} \in \{1, 3, 10, 30\}$

Secondly, the LP collision frequency for LP- temperatures 300 K and 3000 K corresponding respectively to $\boldsymbol{\gamma_{LP}} \in \{6.5, 2.5\}$. ‡

‡The simulation data is actually for a dynamic $\gamma_{LP}(t)$ with the sweep parameter im-

$$\eta(\rho, t) = 2.5 \cdot \eta_0(t) \cdot \sin^4\left(\frac{\rho\pi}{a(t)}\right)$$

$$\eta_0(t) = 540 \cdot \mathbf{c_{LP}} \cdot \exp(-(t-45)/4)$$

$$\gamma(t) = \gamma_{LP}$$

Measurement data for the 2.45 GHz setup and the simulation data for its simulation model under the combined sweep of $\{\mathbf{c_{LP}}\} \times \{\gamma_{LP}\}$ are plotted together in figure 4.3.

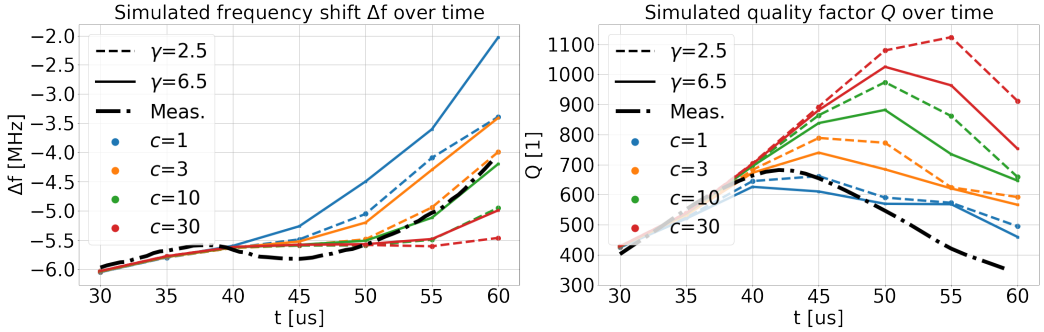

(a) *(b)*

Figure 4.3: *Quality factor and resonant frequency shift over time, experimental and swept simulation values compared*

For the dynamics of $\Delta f(t)$ in Figure 4.3a, there are two solutions that accurately follow the measurements.

$$(c, \gamma) \in \{(3, 2.5),\ (10, 6.5)\}$$

As for the solutions to the dynamics of $Q(t)$ in Figure 4.3b, the only possibility is $c = 1$ with γ almost irrelevant. Evidently, the peak of the quality factor is postponed for higher values c. Therefore, we rule out the most extreme parameter $c = 30$ in any future simulation-runs.

$$(c, \gamma) \in \{(1, 2.5),\ (1, 6.5)\}$$

plemented as $\gamma_{LP} = \gamma(t = 60)$ under linear decay $\gamma_{LP}(t)' = 2.5 + (t - 30)/30 \cdot (\gamma_{LP} - 2.5)$. However, this has been simplified to constant γ due to the main deviation $\Delta\gamma$ mainly at $t = 30$, where its effect can be ignored due to the LP being well beyond cutoff this early on.

Improvements on the $\eta(\rho) \propto \sin^4$ model

There is thus not clearly one combination (c, γ) that gives accordance in both Δf and Q. However, we will not consider more solutions to γ and c, but rather advance the following (possible) resolutions to more accurate reproduction of measurement data.

Firstly, an instinct would be to decrease γ below the values here considered. For $\gamma = 6.5$, c is an entire order of magnitude apart. For $\gamma = 2.5$ c is half an order of magnitude apart. Therefore, it would be logical that Q and Δf both coincide for $\gamma = 1$ and $c = 1$. However, this would imply a temperature of $T = 10,000$ K, which is in conflict with the initial value of the temperature under simulations on flow[18], and in conflict with spectral measurements in [19]. Both of these sources indicate a temperature of $T = 5000$ K at the most. Therefore, we will definitively assume constant $\gamma_{LP} = 2.5$, equivalent with $T_{LP} = 3000$ K.

Secondly, the current distribution $\eta(t, \rho)$ could be refined to a distribution $\eta(t, \rho, \phi)$. Analysis of CCD images exposed a strong angular intensity dependence $\eta(\phi)$, evident from Figure 3.10a. Implementation of this distribution over ϕ endemically requires a higher normalization factor (factor 2.5 for renormalization of $\eta(\rho) \propto \sin^4$) in order to sustain $\iiint_V \eta(t, \rho, \phi) d\tau = \eta_0(t)$. This more accurate distribution would possibly allow for measurement data reproduction under $(c, \gamma) = (1, 2.5)$.

Lastly, processes such as diffusion of charges and imperfections of the $\eta(\rho)$ distribution would introduce some offset electron density η_a on top of the ideal $\sin^4(\rho\pi/a)$ distribution, yielding a *hybrid* electron density distribution $\eta(\rho) = \sin^4 \frac{\rho\pi}{a} + \eta_a$. This is further supported by the fact that across the above parameter-sweeps, the ideal $\sin^4$-distribution achieved data-reproduction of Δf only, whereas simulated Q was consistently higher than in measurement data. This is the exact opposite to the problem with the homogeneous distribution in Figures 4.2a and 4.2b, where Q consistently went below the measured minimum quality factor $Q \approx 350$. This is strong backing to the argument for a *hybrid solution* to be presented as the final characterization of the plasma.

4.2.2 Ansatz- and data comparison for 57 GHz

Having dropped the sweep-parameter-values $c_{LP} = 30$ and $\gamma_{LP} = 6.5$ to be unlikely solutions, we can narrow down to three sweeps in the 57 GHz simulations detailed in Figure 2.1b, with the aim to reproduce measurement data of Figure 2.2b.

We will now implement the sweep $\mathbf{c_{LP}} \in \{1, 3, 10\}$ and $\gamma_{LP} \in \{2.5\}$.

Version of July 8, 2021– Created July 8, 2021 - 13:14

We re-normalize the parameters for the response to the 57 GHz measurement frequency by:

$\tilde{\eta_0(t)} = \eta_0(t) \cdot (\frac{\omega}{\tilde{\omega}})^2 \approx \eta_0(t)/540$

$\tilde{\gamma} = \gamma \cdot \frac{\omega}{\tilde{\omega}} = 6.5 \cdot \frac{2.45}{57} \approx 0.1$

The sweeps are implemented on the plasma containing the LP only, according to (4.3). Visualizing the simulation-model in the Figure 2.1b with propagation direction from left to right: port 1 is at the left-most boundary and port 2 is at the right-most boundary. The transmission data in Figure 4.4 are made by the following evaluation:

$$|S_{21}| \equiv |S_{21}|(c, \gamma, t)/|S_{21}(0, \gamma, t)|$$

, with $|S_{21}(0, \gamma, t)|$ and $|S_{21}|(c, \gamma, t) \approx 0.8$ evidently the transmitted voltage between ports for absence resp. presence of plasma.

$$\tilde{\eta}(\rho, t) = 2.5 \cdot \tilde{\eta_0}(t) \cdot \sin^4\left(\frac{\rho\pi}{a(t)}\right)$$

$$\tilde{\eta_0}(t) = \mathbf{c_{LP}} \cdot \exp(-(t-45)/4)$$

$$\tilde{\gamma(t)} = 0.1$$

Examination of the graph yields the best accordance for the single solution:

$$(c, \tilde{\gamma})_{LP} = (10, 0.1) \rightarrow (c, \gamma)_{LP} = (10, 2.5)$$

This is well outside of the set of solutions $\{(c, \gamma)_{LP}\} = \{(1, 2.5), (3, 2.5)\}$ that gave best accordance with measurement values on the 2.45 GHz setup. For this reason, we will settle the final solution as a logarithmic golden mean $c = 3$ with an error factor that encapsulates the optimal solutions for both setups $c = 1$ resp. $c = 10$. We do this by introducing a power factor p with an error of $\pm\Delta p = \pm 0.5$, where c in the above equation is substituted accordingly:

$$c \rightarrow 3 \cdot 10^{\pm\Delta p} = 3 \cdot 10^{\pm 0.5}$$

4.2.3 Hybrid model- and data-comparison for 2.45 GHz

The parametric sweep will be narrowed down once more to just $c_{LP} \in \{1, 3\}$ and $\gamma_{LP} \in \{2.5\}$. The parameter $c = 10$ is not considered because it is at the "wrong" side of the error margin with $\Delta p = +0.5$. The offset-value to give the correct minimum value of $min(Q)$ for both sweeps $(c, \gamma_{LP}) \in \{(1, 2.5), (3, 2.5)\}$ under 2.45 GHz simulations was found by

Version of July 8, 2021– Created July 8, 2021 - 13:14

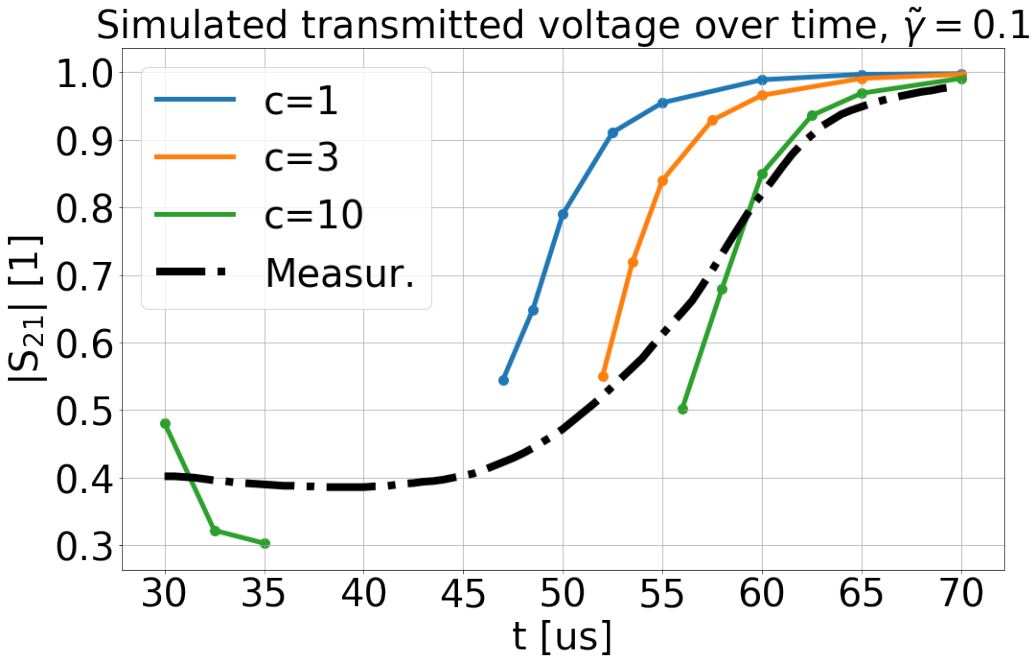

Figure 4.4: *Comparison of simulated transmitted voltage with measurements on the 57 GHz setup. The corresponding simulation model is as detailed in 2.4, with the LP-torus centered between the two horns, no EC present. The electron density is swept with c, with normalized collision frequency* $\tilde{\gamma} = 0.1$ *and the distribution of the electron density as detailed in* (4.3)*. Not all instances of time are represented in the figure, because the simulation would not find convergence to a solution in a reasonable amount of time.*

trial and error to be $\eta_a = 2$. [§] This offset superimposed on the $\sin^4$ distribution delivers the equations laid out in (4.4).

$$\eta(\rho, t) = 2.5 \cdot \eta_0(t) \cdot \sin^4\left(\frac{\rho\pi}{a(t)}\right) + \eta_a, \quad \eta_a = 2$$

$$\eta_0(t) = 1.5 \cdot 10^3 \cdot 10^{\pm 0.5} \cdot \exp\left(-(t-45)/4\right)$$

$$\gamma(t) = 2.5$$

The simulation data corresponding to the implementation of the *hybrid*-distribution in (4.4) with $\eta_a = 2$ are plotted in Figure 4.5, where $c = 3 \sim \Delta p = 0$ represents the "golden mean" with 57 GHz simulations

[§]The corresponding offset for 57 GHz is $\eta_a = 2/540$ which will barely make a difference for the transmitted voltage, dominated by scattering behaviour. Therefore, the results of Figure 4.4 are likely reproduced under the additional offset η_a, so no new simulations for the hybrid distribution are required for 57 GHz.

Version of July 8, 2021– Created July 8, 2021 - 13:14

and where $c = 1 \sim \Delta p = -0.5$ represents the "right side" of the error margin Δp, reproducing the 2.45 GHz simulations.

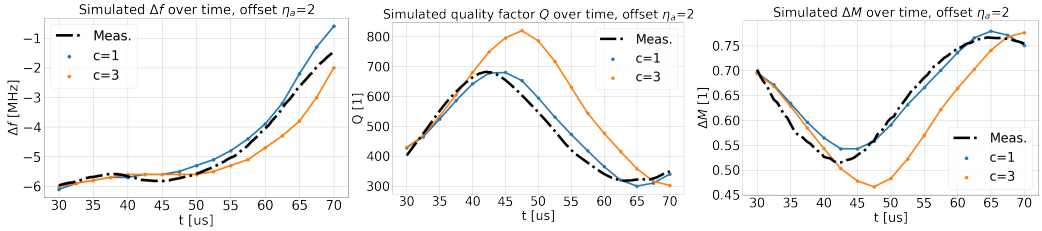

Figure 4.5: *Simulation data for* (4.4)*. Plotted for* $c = 3$*, along with* $c = 1$

Final characterization equations of LP and EC, with error

Under the hybrid distribution, the offset $\eta_a = 2$ is consistently lower than the sine-amplitude amplitude $2.5 \cdot \eta_0(t)$. The offset was only proof that higher values $c = 3$ and $c = 10$ are valid solutions, unlike was presumed from Figure 4.3b. Therefore, we set the offset to zero again, and conclude the parameter-solutions $c_{LP} = 3$, $\Delta p = \pm 0.5$, $\gamma_{LP} = 2.5$.

LP material properties in terms of cross-sectional radius ρ in [mm] and time t in [us]

$$\eta(\rho, t) = 2.5 \cdot \eta_0(t) \cdot \sin^4\left(\frac{\rho\pi}{a(t)}\right) \tag{4.5a}$$

$$\eta_0(t) = 1.6 \cdot 10^3 \cdot 10^{\pm 0.5} \cdot \exp(-(t-45)/4) \tag{4.5b}$$

$$\gamma_{LP} = 2.5 \tag{4.5c}$$

$$\sigma_{LP}(\rho, t) = \epsilon_0 \omega \frac{\eta(\rho, t) \cdot \gamma_{LP}}{1 + \gamma_{LP}^2} \tag{4.5d}$$

In order to determine the conductivity of the plasma, we convert the values of eta and gamma for each to sigma by (1.41b). For the theoretical homogeneous parameters, and for the simulated non-homogeneous parameters, the conductivity is plotted in Figure 4.6.

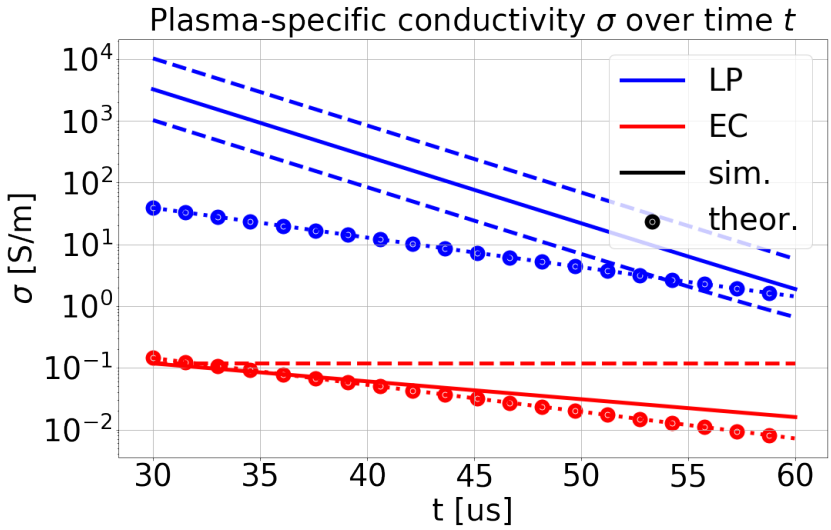

Figure 4.6: *Conductivity over time for LP and EC computed from $\sigma(\eta, \gamma)$ in equation* (1.41b) *in combination with $\eta(t)$ in* (4.5a) *and* (4.1a)*, and $\gamma(t)$ in* (4.5c) *and* (4.1c)*. Margin of error for σ_{LP} is half an order of magnitude $\pm\Delta p = \pm 0.5$. The margin of error for σ_{EC} (with the presumed decay constant $\tau_{EC} = 15$ us) is based off of the extremes $\tau_{EC} \in (1/\infty, \infty)$, pivot at t = 30 us.*

4.3 Characterization of capacitive power absorption efficiency

In the previous section, we characterized the plasma by reproducing experimental values from the plasma-filled cavity. Under these properties of the plasma-components LP and EC, placed within the rectangular TE-101 cavity, we will characterize the efficiency of capacitive heating of the plasma across and beyond the characterized period $t \in [30, 70]$ [us]. As mentioned in the introduction, our ultimate goal is to devise an effective and efficient heating method; where this last section on capacitive heating concerns the evaluation effectiveness and efficiency of capacitive heating. Effectively, capacitive heating should stabilize the LP at a high temperature or ionization grade. Efficiently, this state of LP-stability should possess a high RF-efficiency $\eta_{RF} \equiv P_{a,LP}/P_{in}$, with $P_{a,LP}$ the power absorption in LP and P_{in} the magnetron input power.

Firstly, a simulated determination is made for the ($0\% < \bar{P}_{a,\alpha}(t) < 100\%$) share of power absorption into the absorbing components $\alpha \in \{$LP, EC, and cavity$\}$. Secondly, the properties of the stable LP and EC at the measured stability time are determined, as well as the associated power

absorption under reduced transmitted power to the cavity from subsequent mismatch and mistune. Lastly, the total power absorption associated with the measured stability times in LP- and EC-components ($P_{a,LP} \approx P_{a,EC} \geq 100$ [W]) is used to evaluate the heat-conduction power loss, and whether this is comparable to the simulated power absorption.

4.3.1 Simulated capacitive power absorption ratio

Although a theoretical equation has been developed in order to estimate the capacitive plasma's power absorption in (1.52c), this will not be used to determine the power absorption ratio. Namely, this equation was formalized only for (invalid) homogeneous LP electron density $\eta(\rho) = \eta_0$, and the theoretical LP decay constant τ_{LP} is an underestimate with respect to that of the (realistic) non-homogeneous LP. This can be identified from Table 4.1.

The estimated plasma properties in (4.5) and (4.1) are implemented in the TE_{101} simulation model of Figure 2.3. For different t, three evaluations are made, from which share of power absorption $\bar{P}_\alpha$ into component $\alpha \in \{LP, EC, cav\}$ is extracted by the following equations:

$\bar{P}_{LP} \equiv \iiint_{V,LP} emw.Qe\ d\tau \cdot (1 - |S_{11}|^2)^{-1} \cdot P_{in}^{-1}$,

$\bar{P}_{EC} \equiv \iiint_{V,EC} emw.Qe\ d\tau \cdot (1 - |S_{11}|^2)^{-1} \cdot P_{in}^{-1}$,

$\bar{P}_{cav} \equiv P_{in} \cdot (1 - |S_{11}|^2) - \iiint_{V,LP} emw.Qe\ d\tau - \iiint_{V,EC} emw.Qe\ d\tau$.

Adding these shares of power absorption into a bar-plot produces Figure 4.7.

Expected vs. measured LP- stability time

The data for the power absorption ratio $\bar{P}_{LP}(t)$ in Figure 4.7 represents the share of power absorption into the LP at each time. However, this ignores any (mismatch- and mistune) power leakage by the cavity and assumes that the input power is activated at precisely the time of evaluation t. Namely, if the power input is activated before the evaluation time, components of the plasma are perturbed, thus no longer being comparable to power absorption under the unperturbed decaying plasma properties determined at a glance from Figure 4.7.

As for the plasma's power absorption, under the supposition of matching and tuning, the RF- input power of $P_{in} = 3$ [kW] can be multiplied with the power absorption share in Figure 4.7 to yield the total power absorption $P_a(t)$.

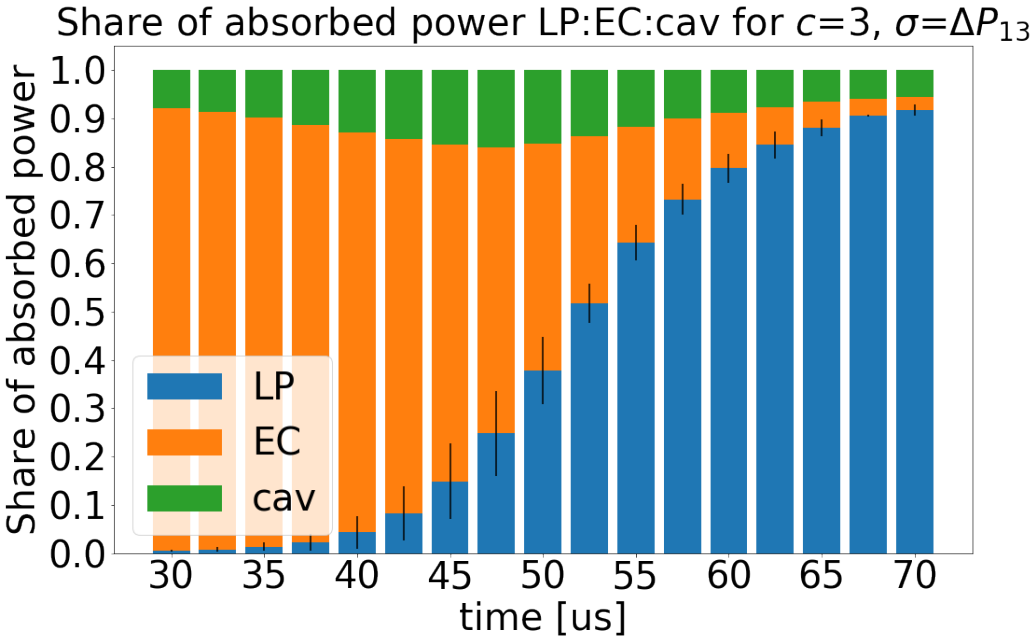

Figure 4.7: *Power absorption ratio for capacitive heating in the old TE_{101} setup. The plasma properties are materially* (4.5) *and* (4.1)*, and geometrically* (3.1) *resp.* (3.6)*. The bar values are solutions for $\Delta p = 0 \sim c = 3$, and the associated error σ in black for each t is the difference of power loss with the case $\Delta p = -0.5 \sim c = 1$, such that $\sigma = \Delta P_{13}/P_1 = \{|P_{LP}(c=3) - P_{LP}(c=1)| + |P_{EC}(c=3) - P_{EC}(c=1)|\}/2$.*

The expected LP stability time $t_{s,LP}$ follows from the intersection of the approximate heat conduction power loss (1.54) in the order $P_l(t) \approx 10$ [W] with the curve $\bar{P}_{a,LP}(t) \cdot P_{in}$ with $P_a(t)$ in Figure 4.7, with the intersection for both LP and EC likely well before the measured stability time $\mathbf{t_{s,LP} = 75}$ **[us]**, by constant intensity in Figure 3.12.

In order to deny that this discrepancy follows from mismatch or mistune, we take into account the factors that reduce the RF-power available to the LP, such absorbing components (EC and cavity walls) or power reflection from the cavity (mismatch, mistune).

Power loss to EC, mismatch and mistune

Parasitic components that absorb RF-power simultaneously with the LP are the cavity walls and the EC. As per the measured EC-stability $t_{s,EC} = 45$ [us] with $Q = 300$ (Figure 2.2a), the EC-power absorption is much larger than cavity power absorption, because $P_{cav}/P_{EC} = Q(t = t\_s, EC)/Q =$

Version of July 8, 2021– Created July 8, 2021 - 13:14

300/2850. Evident from Figure 3.12a, the EC and its properties stabilize. In contrast to Figure 4.7, the share of capacitive EC power absorption is perturbed beyond the EC- stability time $t_{s,EC} = 45$ [us], with $P_{EC} \geq P_{LP} \rightarrow P_{EC} \geq 50\%$.

Mismatch ΔM is one of two causes of power reflection, and is caused by the absorption by the EC and LP under an expected total quality factor $Q \approx 300$. Suppose that the cavity is matched to the waveguide only when empty, with empty-cavity resistance $R = R_0 \approx 0.25\ \Omega$ by Table 2.1. The absorption of the plasma raises the total cavity resistance with the plasma resistance which equals $R_p \approx 4.5\ \Omega$, by (1.13). By substitution in (1.22c), the mismatch equals $\Delta M \approx \frac{R_p^2}{(2 \cdot R_0 + R_p)^2} \approx 0.67$. The associated power attenuation equals $|S_{21}|^2_{\Delta M} = 1 - \Delta M \approx 0.3$

Mistune $\Delta f = f_{mag} - f_0$ is the other cause of power reflection. Suppose that the cavity is tuned to the magnetron frequency only when empty. As per Figure 2.2a, the mistune due to the presence of the plasma is about $\Delta f = -5$ [MHz]. The reflected power associated with this mistune can be computed in combination with the cavity full-width-half max $\Delta f_{1/2} \approx 8$ [MHz] in case $Q \approx 300$. By substitution in (1.23b), the associated attenuation of power transmission equals $|S_{21}|^2_{\Delta f} = \left((2 \cdot \Delta f / \Delta f_{1/2})^2 + 1\right)^{-1} = ((2 \cdot 5/8)^2 + 1)^{-1} \approx 0.4$.

The total power transmission attenuation due to mismatch and mistune is therefore $|S_{21}|^2 = |S_{21}|^2_{\Delta M} \cdot |S_{21}|^2_{\Delta f} = 0.3 \cdot 0.4 \approx 0.1$. Combined with 0.5 share of total power absorption in the EC as well as a 0.5 share of total power absorption in the LP, this yields a minimum total available LP power absorption of about $P_a \gtrapprox 100$ [W] at the LP stability time $t_{s,LP} = 75$ [us].

Properties of the stable plasma under capacitive heating

Because of plasma stability, the power loss is equal to the power absorption and we must thus have for the **plasma (both LP- and EC-) power loss $\mathbf{P_l} \gtrapprox$ 100 [W]**. Evaluation requires the properties of the stable plasma under which these losses need to be calculated.

As for the electron density, we have seen for both LP and EC that their stability times t_s correspond to similar electron density by (4.1b) and (4.5b) accounting for $\eta_0^{(\mathrm{EC})}(t_s = 45) = 0.5$ resp. $\eta_0^{(\mathrm{LP})}(t_s = 75) = 0.83$. For both LP and EC, $\eta_0 \approx 1$ corresponding to $T = 1000$ [K] by (1.53d). Because a power loss of $P_l = 10$ [W] assumed a boundary temperature $T = 3000$ [K],

its remains unexplained why the plasma stabilizes so late.

Note on improvement of capacitive heating

The method of capacitive heating (when started before $t = 30$ us), has the issue of stabilizing the EC well before the stabilizing the LP by Figure 3.12a, whereby the plasma settles at an unfavourable share of power absorption to the EC by Figure 3.12b.

An improvement on the efficiency of capacitive heating would be to postpone the RF signal well beyond the EC stability time $t = 45$ us and near LP stability time $t = 60$ us. This postponement would ensure that the EC decays well below significant losses. By CPT (1.26b), a plasma of the size $V_s = 100$ mm^3 within the capacitive heating setup only decreases the available RF-power if $Q_s \leq 1/2 \cdot Q_0$ meaning $\epsilon_r'' \ll \frac{1}{Q_0}\frac{V_0}{\chi_E V_s} = 0.25 \sim \eta_{EC} \approx 2$. Therefore, postponing RF-heating until $t_s \approx 75$ us - where $\eta_{EC} \approx 0.07 \ll 1$ by (4.1a) - will ensure that virtually all RF-power absorption will take place in the LP.

However, after such a decay, the LP has lost its hallmark high ionization grade. Moreover, when the capacitive heating stabilizes the LP, the skin effect concentrates most heating near the boundary of the LP, leading to high heat conduction losses due to the proximity to the cold surroundings. Consequently, this dissipation of heat - possibly in combination with ambipolar diffusion - might form a plasma around the LP over time, possibly creating the unfavourable situation analogous to the presence of the EC.

Conclusively, capacitive heating of a LI-plasma is inefficient and poorly optimizable. We require a new (inductive) heating method that will be discussed in the next chapter.

Version of July 8, 2021– Created July 8, 2021 - 13:14

Chapter 5

Characterization of inductive plasma heating

Where the previous chapter has investigated heating the plasma through the oscillating electric field, this chapter will investigate heating the plasma by its positioning at the oscillating magnetic field. The power absorption over conductivity will (in both theory and simulation) be analyzed with the goal of determining whether inductive power absorption favours LP over EC, and to determine at what optimal conductivity σ_{opt} the LP power absorption is maximal. Two new cavity types are designed to facilitate this *inductive heating* by the magnetic antinode at the center of the cavity volume: the rectangular TE_{102}-, and the cylindrical TE_{011}-cavity. Through simulation, we predict how these cavities affect the plasma power absorption ratio $\bar{P}_a$ into LP, EC, and cavity walls. For inductive heating in the rectangular TE_{102} cavity, we will estimate the power absorption theoretically and compare these evaluations with simulations of inductive heating. Afterwards, we explore benefits by transitioning to inductive heating in the cylindrical TE_{011} cavity.

5.1 Characterization of inductive power absorption

In order to provide a lucid characterization of the power absorption into LP and EC, it is convenient to maintain a single degree of freedom in homogeneous conductivity σ applied to a static geometry; the geometry should reflect both LP- and EC-geometry over the time-domain $t \in [30, 60]$ [us], (the time domain for which we have characterized both components).

Version of July 8, 2021– Created July 8, 2021 - 13:14

An oscillating magnetic field strength $|B|$ then induces a current density J within the domain, to be derived from (1.48a). This is finally integrated over the (toroidal) geometry along (1.48b) to obtain the power absorption within the domain.

Firstly, the geometry we maintain will be the geometry of the LP at central time $t = 45$ us, which by (3.1) roughly entails a torus with $(r, a) = (3.75, 1.58)$ [mm]. This approximate static geometry roughly models that of the EC (3.6) as well, because the EC is concentrated within two pairs of rings with central radii $r_1 \approx 2$ [mm], $r_2 \approx 4$ [mm], and square cross-section with side-length $h = 1$ mm. Subsequently, the combined EC-volume $V_s = 80$ [mm^3] is in the same order of magnitude as that of the LP ($V_s = 180$ [mm^3]), with most of this volume concentrated near $r_2 \approx r = 3.75$ [mm]. The geometry is thus a valid approximation for both LP and EC, and this can be confirmed with some imagination from the cross-sectional geometry of the composite plasma visualized in the third column of 3.1.

Secondly, the conductivity must span the full range of conductivities of LP and EC within the characterized time-span $t \in [30, 60]$ us. At a glance from Figure 4.6, this means that the lower limit of the range must coincide with $\sigma_{EC}(t = 60) = 1e-2$ [S/m] and the upper limit of the range must coincide with $\sigma_{LP}(t = 30) = 1e4$ [S/m], giving $\sigma \in [1e-2, 1e4]$ [S/m]. Theoretical computations of the induced current density and power absorption will be made under fixed real free-space relative permittivity $\epsilon'_r = 1$, to ignore effects from ϵ'_r. Although the characterization of the plasma estimated $\gamma \approx 2.5$, which for $\sigma \gg 1$ [S/m] implies $\epsilon'_r \ll 1$, simulations on inductive heating of the plasma indicated that effects of ϵ'_r on power absorption could be ignored, with absorption dominated by σ.

Lastly, the local amplitude $|B|$ of the oscillating magnetic field equals B_0 by the plasma's placement at the cavity's center $(x, y, z) = (a/2, b/2, d/2)$, as is evident from the field equations (1.27). Unlike the plasma-parameters r, a, σ, the amplitude B_0 of the magnetic field is dependent on the cavity type chosen - cylindrical or rectangular - because these possess different quality factor Q, cavity volume V_0, and energy density ratio χ_B - as evident from (1.50). However, this paper only covers and will only provide power absorption simulation data on the initial rectangular TE_{102}-setup, and we limit ourselves to the rectangular cavity magnetic field amplitude only. This possesses properties that closely resemble that of the rectangular TE_{101}-setup, with comparable cross-sectional dimensions a and b, volume V_0, quality factor Q, and equal density ratio χ_B. Under the assumption of matching and tuning along with 3 kW input power, by Table 2.1, the local amplitude near the plasma equals $B_0 = 0.004$ [T].

5.1.1 Induced current density

In order to determine whether the theoretical calculation of the inductive current density is accurate, it is compared with simulations on the induced current density within the plasma. This comparison is executed for a single conductivity $\sigma = 30$ [S/m], which is the mean conductivity of theoretical and simulated approximation at $t = 45$ [us] in Figure 4.6. Moreover, this is a representative sample-value of conductivity because it is close to the logarithmic average of the range of conductivities to be investigated later.

The theoretical evaluation of the induced current density distribution is numerically determined by insertion of plasma-cross-sectional coordinates (r, ϕ) into equation (1.48a) for the geometric properties as described above, with magnetron frequency $f_{mag} \approx 2.45$ GHz (but with reduced field B_0' to be determined soon). The coordinate-dependent absolute value of the induced current density $|J_i|(r, \phi)$ is evaluated in Python for a meshgrid of the torus cross-section $(0 < r < a, 0 < \phi < 2\pi)$. The simulated evaluation of the induced current density across the cross-section is made by positioning the plasma at the center of the TE_{102} model axisymmetric with $\hat{x}$ in Figure 5.4 and evaluating the *slice* across a plane through the center of the torus, parallel to $\hat{x}$. This simulation model is excited with an RF-signal at the system's resonance frequency and with input power $P_{in} = 3$ kW. Although thus tuned, the model is not matched; it is matched only for the empty cavity (read: for no plasma power absorption). Moreover, plasma power absorption reduces the available field energy and thereby the system's quality factor. This needs to be accounted for in theoretical evaluations, by the introduction of the plasma resistance R_p.

In terms of transmission line theory, the total cavity resistance is raised by plasma power absorption incorporated into the plasma resistance R_p, leading to a non-zero mismatch and reduced quality factor by (1.22c) resp. (1.22b). Here, P_0 is the total plasma power absorption under un-reduced field magnitude B_0, P_{in} is the input power, and R_0 is the cavity resistance. We can compensate for the subsequent reduction in magnetic field amplitude B_0 by substitution of this plasma resistance (5.1a) into (1.50). Consequently, we account for the non-zero mismatch and the reduced quality factor by reducing B_0 to B_0' through the two equations (5.1), lucidly encapsulating the required theory for determining the *re-normalization factor* c (5.1c) of the field magnitude.

$$R_p = \frac{P_0}{P_{in}} \cdot R_0 \tag{5.1a}$$

$$B_0' \equiv c \cdot B_0 \propto \sqrt{Q}\sqrt{P} \propto \sqrt{Q}\sqrt{(1 - \Delta M)} \tag{5.1b}$$

$$c \equiv \frac{B_0'}{B_0} = \sqrt{\frac{2}{2+\alpha}}\sqrt{1 - \frac{\alpha^2}{(2+\alpha)^2}}, \quad \alpha \equiv \frac{P_0}{P_{in}} \tag{5.1c}$$

The power absorption under un-reduced field magnitude for $(r, a) = (3.75, 1.58)$ [mm], $\sigma = 30$ [S/m] and $B_0 = 4$ [mT] equals $P_0 \approx 12$ [kW] by evaluation of (1.48b) (or see un-reduced field power absorption computed for the full range of σ and plotted in Figure 5.2a). Subsequently, evaluation of (5.1a) yields $R_p = 12/3R_0 = 4 \cdot R_0$, such that $\alpha = 4$ in (5.1c), and thereby the field is reduced by a factor $c = 0.43$ with $B_0' \approx 1.8$ mT. However, this is only a zeroth order estimate of the reduced field. Firstly, the recursive nature of the re-normalization means that this new reduced field implies a higher quality factor and lower mismatch than the un-reduced field, raising B_0', moreover requiring infinite subsequent re-evaluations. Secondly, the magnetic field magnitude B_0 and cavity resistance R_0 of the TE_{102} setup are only estimates based on the TE_{101}-setup leading to a possibly erroneous value of B_0'.

Simulations on the tuned, empty-matched TE_{102}-setup with input power $P_{in} = 3$ [kW] and the plasma-parameters as above, the induced current density slice over the cross-sectional plane yields Figure 5.1b, with upper limit of the induced current density $max(|J|) = 6.5e5$ [A/m^2]. In theoretical evaluation on the plasma-parameters combined with $c = 0.43$, on the other hand, evaluation of (1.48a) yields maximum induced current density of 9.5 [A/m^2]. For a nice side-by-side comparison of the cross-sectional induced current density distributions, the field magnitude renormalization factor has been reduced further from $c = 0.43$ to $c = 0.3$ and the subsequent distribution is plotted in Figure 5.1b.

Version of July 8, 2021– Created July 8, 2021 - 13:14

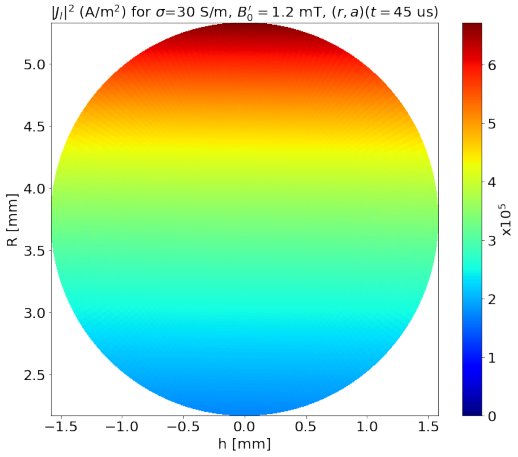

(a) *Theoretical induced current density*

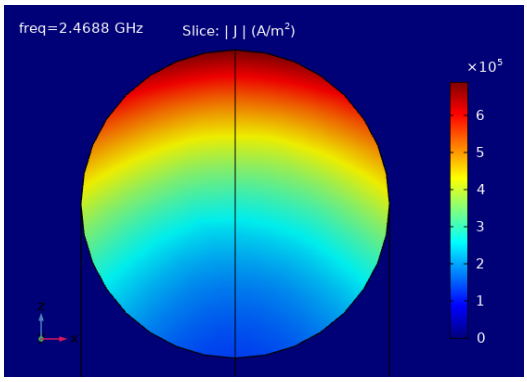

(b) *Simulated induced current density*

Figure 5.1: *Comparison of theoretical vs. simulated induced current density* $|J|$ *[A/m^2] along torus cross-section for* $\sigma = 30$ *S/m and* $(r,a) \approx (3.75, 1.58)$ *[mm]. Simulation-data for torus at center of matched and tuned rectangular* TE_{102} *cavity with* $P_{in} = 3$ *kW matched cavity. Theoretical data from numerical implementation of* (1.47a) *with normalized reduced field strength* $B_0' = 0.3 \cdot B_0 = 1.2$ *mT.*

From comparison between theoretical (Figure 5.1a) and simulated (Figure 5.1b) induced current density, we conclude good magnitude of $|J|$ from theory. Accordance under $c = 0.3$ with $|J| \propto |B|$ also implies that the induced current density would have been at most half an order of magnitude off had it not been normalized (in which case $c = 1$). Moreover, the simulated distribution resembles that of the induced current density under magnetic induction, and we may conclude that magnetic induction is indeed dominated by the longitudinal excitation assumed in (1.48a).* As for its deviation, this is likely because the simulations incorporate induced current from transverse magnetic field as well, which is visible as a non-axisymmetric (w.r.t. the laser-axis, $\hat{R}$) distribution in Figure 5.1b, whereas Figure 5.1a is axisymmetric.

Regardless, the developed theory on magnetic induction holds up to simulation in the two main aspects: the magnitude of $|J|$ and subsequently the magnitude of P_a, as well as the re-normalization factor c. Now that the accuracy of theory is proved for single σ, we can rely on the theory in an inquiry of the plasma's magnetic-induction power absorption over the full range of σ.

*One can rule out that transverse excitation dominates by comparison with [14, Figure 3(a)], rotated 90 degrees with respect to Figure 5.1.

5.1.2 Power absorption ratio

Inspired by the previous subsection, this subsection on power absorption will employ the same approach to determining the power absorption of the plasma under inductive heating: for each σ in the range of LI-plasma conductivities, the total power absorption is computed under un-reduced field and is then re-normalized by this magnitude through the constraint $P_{in} = 3$ [kW]. For starters, the total power absorption is determined at the un-reduced magnetic field strength $B_0 = 4$ [mT], and for the average toroidal geometry $(r, a)(t = 45) = (3.75, 1.58)$ [mm] over the range of $\sigma \in [1e-2, 1e4]$ [S/m]. The total absorbed power is computed over this range of conductivities σ, and it is plotted in Figure 5.2a. The subsequent power absorption far exceeds the input power, and must therefore be re-normalized. We have concluded previously that renormalization required both the mismatch and quality factor. By far the largest error in calculating c is due to the mismatch, because (5.1c) relies on accurate empty-cavity resistance R_0.[†] Therefore, the cavity has been matched for each σ by substitution of un-reduced power absorption corresponding to plasma resistance R_p in (5.1a) which, by implementation of theory on matching, leads us to a matching iris radius r as follows:

$$r = \sqrt[3]{\frac{\mathcal{L} \cdot \sqrt{1 + \frac{P_0}{P_{in}}}}{\gamma \cdot \psi(r_0)}}$$

Because the order of magnitude of the induced current density - and thus the magnitude of the power absorption - is similar for both theory and simulation, the theory can be used for cavity matching in simulations. The iris radii thus deduced were checked to have a maximum tuned reflected power of $(|S_{11}|^2) = 0.1$, but they have been calibrated further to give maximally $(|S_{11}|^2) = 0.01$.

The values in Figure 5.2a are renormalized under reduced quality factor and zero mismatch using (1.51), and are plotted with label *theor.* in Figure 5.2b. The plasma power absorption in simulations are determined from simulations on the tuned and matched TE_{102} cavity, and are plotted with label *Sim.*.

[†]This will not be computed for the TE_{102} cavity because of the presence of FQ-slabs, with subsequent perturbed field equations as well as interference behaviour leading to reflection/transmission at Air-FQ interfaces.

Version of July 8, 2021– Created July 8, 2021 - 13:14

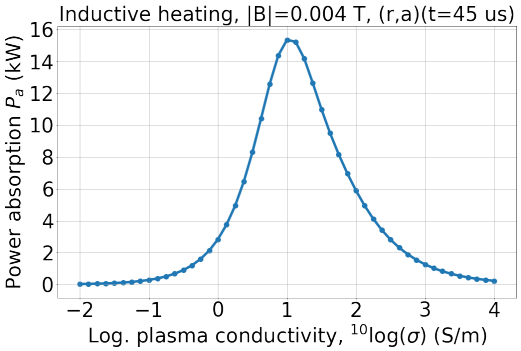

(a) *Theoretical total power absorption for constant field strength*

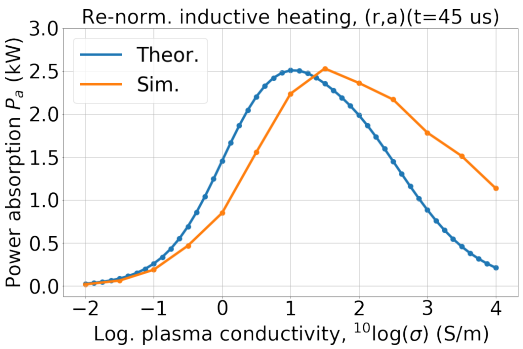

(b) *Calibrated values of theoretical power absorption, plotted along simulated power absorption in a TE-$_{102}$ cavity.*

Figure 5.2

Power absorption ratio of LP and EC, and stability

From Figure 5.2b, an accurate comparison is made between total plasma power absorption within the TE_{102}-cavity predicted by theory and by simulation. We identify from the curve maximum a theoretical optimal power conductivity $\sigma_{opt} = 10$ [S/m], whereas simulations predict half an order of magnitude higher at $\sigma_{opt} = 30$ [S/m]. We also see that for modelling the EC with the geometry of the LP (a torus), its corresponding power absorption is much lower by comparison of the logarithmic time-average conductivity $\sigma_{EC} \approx< \sigma_{EC} >_t \approx 1e-1.5$ [S/m] and $\sigma_{LP} \approx< \sigma_{LP} >_t \approx 1e2$ [S/m]:

$$P(\sigma = 10^{-1.5}\ [\mathrm{S/m}]) \ll P(\sigma = 10^{2}\ [\mathrm{S/m}]) \rightarrow P_a(\sigma_{EC}) \ll P_a(\sigma_{LP})$$

This indicates than we can likely ignore influence of the EC under inductive heating. However, the deviation of the LP geometry from the EC as well as possible perturbations of the field amplitude distribution due to LP-cutoff have not been accounted for. Therefore, we will confirm this hypothesis of negligible EC inductive power absorption later, through simulations on the composite plasma under inductive heating (to be plotted in Figure 5.5).

Resonant frequency shift Δf from beyond-cutoff torus under inductive heating

As could be seen from the simulation data in Figure 5.2b, the plasma absorbs a large amount of energy even for high conductivity. Therefore, if a

high input power is chosen, it is likely that the plasma will stabilize (power equilibrium $P_a = P_l$) for a high conductivity $\sigma \gg \sigma_{opt}$. At such conductivities, important effects on the frequency shift need to be considered. Firstly, the corresponding skin depth is so small that the torus can be considered perfectly conducting, thus settling at some geometry-dependent frequency shift Δf, by reasoning similar to $\eta \to \infty$ under capacitive heating in Figure 4.1a. Under (capacitive) placement at the E-field, a conductive torus causes a frequency shift fully determined by its (constant) volume and the torus-specific shape factor $x = 1/2$. However, for (inductive) placement at the B-field, this proportionality might not (and will not) hold. Secondly, the temperature increase due to (now successful) power absorption under inductive heating will cause an increase of temperature within the torus, such that its cross-section expands radially outward along $\hat{\rho}$ (a increases, r remains unchanged). The subsequent increase in volume leads to a frequency shift, and per compensation requires additional re-tuning of the cavity. Therefore, we require an inquiry into the frequency shift for major radius r at different instances, and containing different volumes V around the LP's unperturbed (constant) volume $V_s = 180\text{mm}^3$. This is (roughly) attempted in the appendix on the frequency shift under inductive plasma heating.

5.2 Characterization of rectangular TE-102 cavity

The new setup that will be used to heat the LP will be a rectangular cavity. Instead of the previous dimensions of a custom waveguide, a WR-340 waveguide will be used with a circular aperture (same iris type) isolating the cavity at its short. The dimensions of the WR-340 waveguide cross-section are $a \times b = 86.36 \times 43.18$ [mm^2], with corresponding $\lambda_g|_{-f_{mag}} = 171$ [mm].

First, we will address the issue of tuning when inserting slabs of fused quartz into the cavity. Then we will derive the appropriate cavity dimensions. The power absorption ratio of LP, EC, and cavity walls will then be studied for the composite LI-plasma at the cavity-center, with EC as (4.1), and non-homogeneous LP as (4.5).

5.2.1 Tuning-relation $(w, d)|\delta$ for the rectangular TE-102 cavity containing FQ slabs

CPT tells us that inserting a dielectric in a cavity changes its resonant frequency. Aside from the requirement of heating the plasma, injection

of gas and extraction of plasmolysis-products requires the plasma to be preferably isolated from the remainder of the cavity. Conventionally, fused quartz is used in applications of flow confinement because of its low dielectric loss factor ϵ''. The plasma is usually confined within a (hollow) FQ-tube placed concentric with the cavity's E-field antinode, while gas is injected on one end, and extracted on the other.

In the case of this setup, the plasma is placed axisymmetrically- and concentrically with B-field antinode. In case of a concentric and axisymmetric placement of the FQ-tube partially occupying the nearby E-field, the homogeneity of the E-field along $\hat{y}$ (1.27) for the TE_{101}-mode is violated by the non-homogeneous relative permittivity. Therefore, the plasma and surrounding gas are confined by placement of two rectangular FQ-slabs with a thickness $\delta = 10$ mm, each on either side of the plasma and oriented orthogonal to the propagation direction $\hat{z}$.

The cavity resonance frequency is reduced because of the electric-field energy within the above-unitary relative permittivity of the FQ-slabs; we thus need to reduce the cavity depth d in order to raise the cavity resonant frequency to the magnetron frequency f_{mag}. In the absence of additional constraints, the two slabs could be translated along $\hat{z}$ at constant inter-window-distance w, differently perturbing and occupying the cavity standing-wave E-field pattern depending on each slab's position z by (1.27). For the sake of simplicity, the two slabs provide equal frequency-shift if placed symmetrically with respect to the half-plane of the cavity (plane through the cavity's volumetric center, orthogonal to $\hat{z}$). Additionally, symmetric placement of the FQ-windows are supported by the goals to be satisfied by the final setup:

1. Tune the cavity resonant frequency to the magnetron frequency (tuning)
2. Match the cavity with or without plasma to the waveguide (matching)
3. Position the laser focus, and thus plasma, midway between the slabs (minimal influence on flow-dynamics of torus-formation, minimal electron density at the interface with the slabs)
4. Have the laser focus - and thus the plasma - at the position of the magnetic field antinode (magnetic induction heating)

Fulfilment of the final two bulletin-constraints requires symmetric placement of the dielectric slabs from the cavity half-plane $d/2$. Namely, both

Version of July 8, 2021– Created July 8, 2021 - 13:14

slabs will then contain equivalent electric field strength and thereby perturb the cavity's resonant frequency equally, yielding equation (1.32). Consequently, equal field perturbation in either slab settles the magnetic field antinode exactly halfway the cavity depth and exactly halfway both slabs, thus satisfying the final two bulletins.

In order to derive the relation $d(w)$, simulations are made on a fully-enclosed ("boxed") WR-340 TE_{102}-mode cavity containing two WR-340-cross-section FQ-slabs of thickness $\delta = 10$ [mm] symmetric to the cavity center, with distance w between their (volumetric) centers. By a parametric sweep of the cavity depth d for sample window-distance w, combinations (w, d) satisfying resonant frequency $f_0 = f_{mag} = 2.469$ [GHz] are plotted in Figure 5.3. Additionally, the solutions (w, d) to equation (1.32) are plotted for comparison.

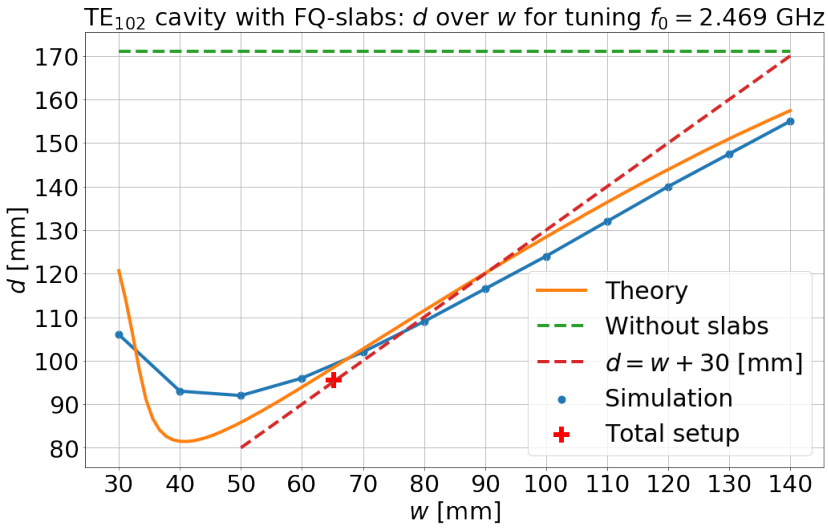

Figure 5.3: *Cavity depth d over window distance w for empty-cavity resonance frequency tuned to magnetron frequency $f_0 = 2.469$ [GHz]. Both windows with FQ-permittivity occupy a thickness $\delta = 10$ [mm], while the remainder of the cavity-volume contains free-space-permittivity, as provided in Table 1.2. Theoretical solutions "Theory" are provided by* (1.32)*, simulated solutions "Simulation" are provided by the simplified simulation model in Figure 8.2a, and full-model solution "Total setup" is provided by the full simulation model in Figure 5.4.*

From Figure 5.3, we see that there is some discrepancy between the theory and simulations. This is most likely due to the electric field energy distribution over the cavity depth - $|E|^2(z)$ - not being a perfect sine squared - $\sin(z)^2$ - but a perturbation of such a distribution. This is due to EM-waves travelling more slowly through the FQ-dielectric - $z \in [\pm w -$

$\delta/2, \pm w + \delta/2]$ - : the phase change along a depth of 10 mm in air being smaller than the phase change along a depth of 10 mm of FQ. Nevertheless, by examination of Figure 5.3, the theory is usually in accordance up to an error of about $\pm$ 5 mm.

5.2.2 Properties of the TE-102 cavity setup

Matching of the (plasma-filled) TE-102 cavity

Just like in the case of the old TE_{101} cavity setup, matching is achieved through a combination of a circular aperture iris with fixed radius placed at the interface of waveguide and cavity, and a stub with variable height at quarter guide wavelength in front of the iris. The variability of the stub height allows for matching at different cavity resistivities associated with plasma power absorption. The motorized stub with maximum protrusion $\max(h_s) = 25$ [mm] (along with the possible addition of a stub opposite in $\hat{y}$) corresponds to maximum turn ratio and minimum (empty) cavity resistance. In case of non-zero plasma power absorption, thus raising the cavity resistance, the stub can be lowered per compensation. Because we have not addressed theory on the stub height and because the iris alone matches the cavity for unknown (non-empty) cavity resistance, the equivalent circuit investigations will not be made for the WR-340 TE_{102} setup. In comparison with the 90×40 [mm^2] custom waveguide of the TE_{101}-cavity, the approximate shape $a \times b$ and waveguide impedance Z_{wg} are roughly equal. Moreover, the insertion of FQ-slabs will reduce the cavity depth down to $d \approx 95$ [mm] (see Figure 5.3, *Total setup*), which is comparable to that of the old TE_{101}-setup with $d \approx 83$ [mm]. By comparable magnitude of Z_{wg} and d, the cavity resistance is equal and the approximate empty-cavity-matching iris radius is likely about $r_0 \approx 11$ [mm]. **For additional properties of the TE_{102}-mode cavity, refer to Table 2.1**.

Tuning of the (plasma-filled) TE-102 cavity

As for engineering constraints on cavity design, an analysis of the dimensions of the components in between the slabs (optical tubes and window-flanges) have yielded that the minimum possible distance between the closest slab-surfaces of $\min(w - \delta) = 55$ [mm], corresponding to required window distance $\boldsymbol{w \geq 65}$ **[mm]**. Another constraint was the need for a distance of $\boldsymbol{d_{i,S} = 10}$ **[mm]** between iris and the closest surface of the first window. By the requirement of symmetric placement of the slabs, the latter constraint completely solves all cavity dimensions. Namely, we re-

Version of July 8, 2021– Created July 8, 2021 - 13:14

quire (nearly)‡ equal distance $ds, S \approx d_{i,S} = 10$ [mm] between the second slab and the short. Consequently, the total depth of the cavity equals $d = 2 \cdot d_{i,S} + \delta + w$, with the corresponding relation between depth d and window distance w of: **Constraint: $d = w + 30$ [mm]**. From the intersection of the constraint-relation with simulation data in Figure 5.3, we read the solution $(w, d) \approx (77, 107)$ [mm]. However, solutions $d(w)$ did not account for the insertion of the iris, the slab-flange protrusion, and the optical tubes, all of which decrease the resonant frequency, and thereby result in a smaller cavity depth d. Therefore, a sweep $(w, d) = (w, w + 30), w \in (77]$ [mm] is made on the full simulation model with iris, slab protrusion, and optical tubes in Figure 5.4, yielding resonance at magnetron frequency $f_{mag} = 2.469$ [GHz] for the actual solution $(w, d) = (65.25, 95.5)$ [mm], indicated with a red cross in Figure 5.3. This solution only just satisfies the constraint on the minimum window distance, where the reduced cavity depth d has the convenient benefit of increasing the (magnetic) field energy density within the cavity.

Below the dimensions in Figure 5.4, the E- and H-field magnitude for the TE_{102} are visualized for the induction heating configuration on the LP with properties (3.1), (4.5) at laser-pulse-delay-time $t = 45$ [us]. Following the strategy outlined in the subsection on power absorption share for capacitive heating on the capacitive TE_{101} heating setup, the share of power absorption into the identical composite plasma with characterization properties ((4.5), (4.1), (3.1), (3.6)) upon its implementation in magnetic induction heating configuration in the TE_{102}-setup is accomplished. Resulting magnetic induction heating power absorption shares $\bar{P}_a$ (into LP, EC, and cavity) are plotted in Figure 5.5.

5.3 Characterization of inductive power absorption efficiency

5.3.1 Simulated inductive power absorption ratio

Evidently from examination of Figure 5.5, the parasitic EC power absorption under inductive heating is vastly reduced with respect to capacitive heating in Figure 4.7. Although, the RF-energy efficiency η_{RF} has increased by reduced power absorption in the EC, the LP does not absorb as much

‡Tuning is done through a sliding short, necessarily requiring variability of $d_{s,S}$. In the final dimensions of the setup, $d_{s,S}$ is given extra distance to provide additional tuning leeway in case some frequency-shift-effects have not been accounted for in simulation.

Version of July 8, 2021– Created July 8, 2021 - 13:14

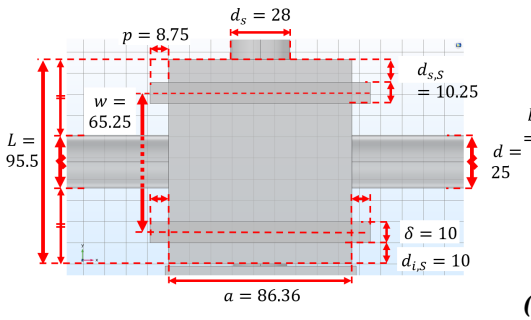

(a) View above the final double cavity

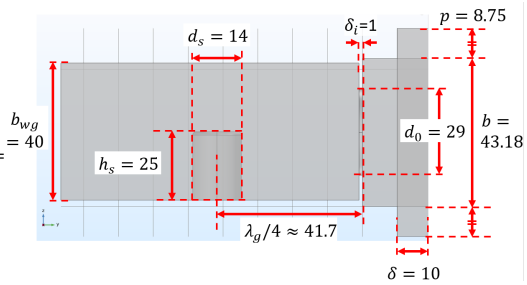

(b) Side view of the final double cavity matching circuit

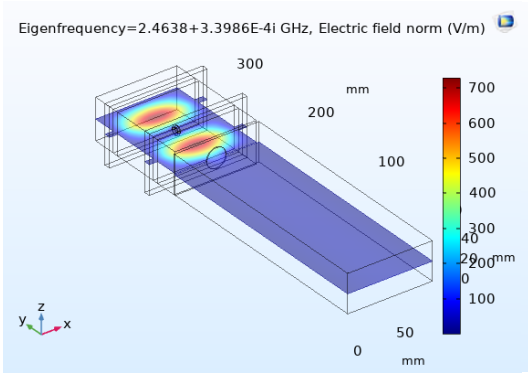

(c) Free view and the electric field strength.

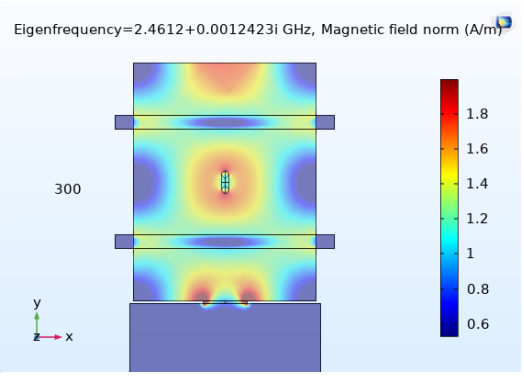

(d) Top view and the magnetic field strength

Figure 5.4: *Geometry of the rectangular TE_{102}-mode setup given in [mm]. Along with field norms of Electric and Magnetic field for simplified version.*

power under inductive heating as it did under capacitive heating. As a consequence, the LP now competes for power absorption with the cavity walls. The maximum inductive power absorption ratio $\bar{P}_a$ for the LP is at $t \approx 50$ [us], with the cavity walls still absorbing up to 30 percent of power ($\sim \alpha = 2$). In contrast, under capacitive power absorption, the LP absorbs optimally at $t \approx 70$ [us], with cavity walls absorbing only up to 5 percent of RF-power ($\sim \alpha = 20$). In other words, capacitive heating into the LP at the E-field antinode of the TE_{101}-cavity and with $\sigma(t = 70) = \sigma(\eta = 2, \gamma = 2.5) = 0.7$ [S/m] leads to more power absorption than the LP at the B-field antinode of the TE_{102}-cavity and with $\sigma(t = 50) =< \sigma(\rho, \eta = 300, \gamma = 2.5) >_\rho \approx 0.4 \cdot 21$ [S/m] $= 8$ [S/m]. By (3.1), the LP-geometry is roughly the same at both instances, and is thus not the cause of this different behaviour.

The question becomes: what makes capacitive heating at optimum capacitive conductivity more absorptive than inductive heating of the same sample at optimum inductive heating. This different behaviour is domi-

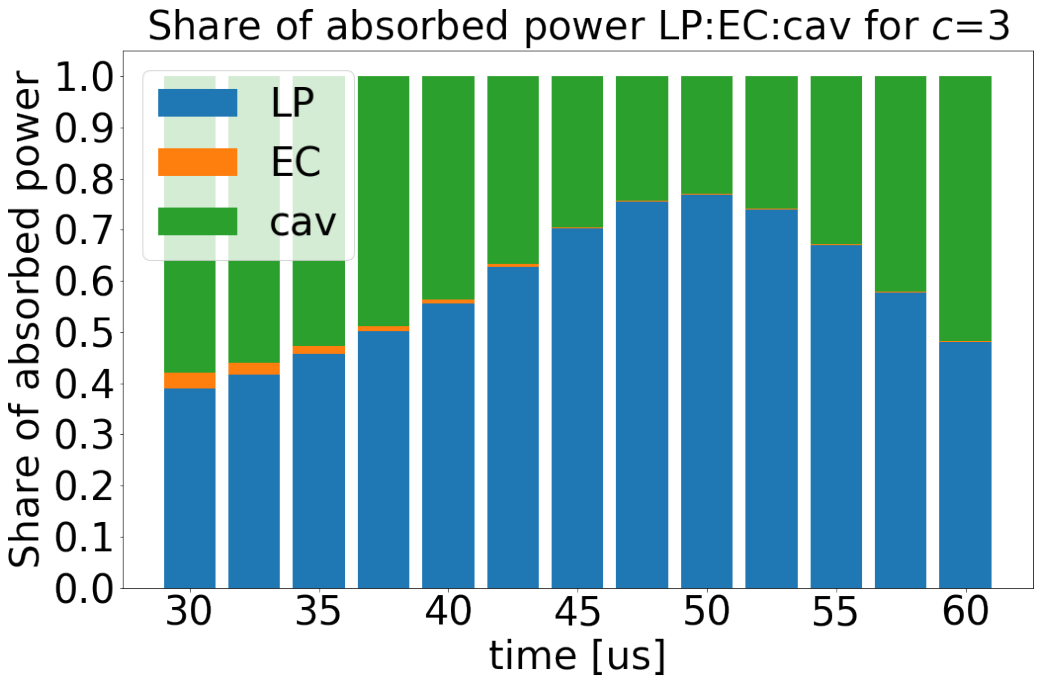

Figure 5.5: *Power absorption ratio for inductive heating in the TE_{102} setup-model of Figure 5.4. Plasma properties are materially* (4.5) *and* (4.1) *with $\Delta p = 0$, and geometrically* (3.1) *resp.* (3.6).

nated primarily by the optimum conductivity σ_{opt}, which is different for capacitive and inductive heating. In both cases, conductivity is expected to be optimal at the transition of cutoff, meaning: the field within the sample volume is negated to induce (current) losses ($G, Y < 1$) yet such that enough field penetrates the sample in order for most of the sample volume to contribute to absorption ($G, Y \gg 0$). Under capacitive heating of the LP, this is evident in case of optimum power absorption $\sigma = \sigma_{opt}$, because by (1.46b) $G(\sigma_{opt} = 0.7\,[\mathrm{S/m}]) = 1/(1 + 2.5 \cdot 1.6/12.2) = 0.75$ such that losses occur within virtually 75 percent of the sample volume. Under inductive heating of the LP, the effective fractional volume is equal to $Y(\sigma)$ in (5.2) [25, Self-inductance of thin wire shapes, bulletin two, cross-reference to: Rosa (1908)], and attains a form similar to that of (1.46b).

$$Y(\sigma) \equiv 1/(1 + 0.5 \cdot a/\delta(\sigma)) \tag{5.2}$$

It is therefore no surprise to find under substitution of the optimal inductive conductivity that $Y(\sigma_{opt} = 8\,[\mathrm{S/m}]) = 1/(1 + 0.5 \cdot 1.6/3.5) = 0.81$ such that (current) losses occur within virtually 81 percent of the sample volume, which is almost identical to the "optimal" fractional effective vol-

ume in the case of capacitive heating.

Finally, we can now explain why power absorption under inductive heating is endemically lower than power absorption under capacitive heating. Substitution of these effective fractional volumes G and Y into (1.42) allows extract the integrand and derive proportionality relation of $P(\sigma)$, the power absorption at optimum conductivity. For capacitive heating, this yielded (1.46a) simplified with $|T|^2 \approx 1$ to $P_c^{(opt)} \approx V_s \cdot G \cdot J^2/\sigma_{c,opt}$. For inductive heating, the equivalent relation can be found through substitution $G \to Y$ such that $P_i^{(opt)} \approx V_s \cdot Y \cdot J^2/\sigma_{i,opt}$. We can thus find the ratio of optimum power absorption for capacitive over inductive heating, by the convenience $Y \approx G$ for optimal absorption as well as (very roughly) equal induced current densities by $< J_c > c \cdot \sigma \cdot E \approx 0.3 \cdot 0.7 \cdot 1.2e6 \approx 2.5e5 \approx < J_l >$:

$$\frac{P_c^{(opt)}}{P_i^{(opt)}} = \frac{\sigma_i^{(opt)}}{\sigma_c^{(opt)}} = \frac{8.4}{0.7} \approx 10$$

By the renormalization equation (1.51) this means that $\alpha_c = 10 \cdot \alpha_i$, which is exactly what was found from the peak power absorption ratios in Figure 5.5 and Figure 4.7, with $\alpha = 2$ resp. $\alpha = 20$. In summary: with respect to capacitive heating, the higher optimum conductivity for inductive heating implies that peak inductive power absorption is lower.

5.3.2 Plasma power loss at stability under inductive heating

In order to determine the total reactor energy efficiency in equation (1), we need to supplement the RF-efficiency $\eta_{RF} \approx 0.7$ with an account of the plasma power loss associated with the stable plasma under inductive heating, which requires an estimate of the plasma's properties at stability. At stability under inductive heating, we may assume that the LP will stabilize near its optimum conductivity attained at $t = 45$ [us], by (4.5d) and (4.1) corresponding to LP-conductivity $\sigma_{LP}(t = 45[\text{us}) = \sigma_{opt} = 30$ [S/m] and EC-conductivity $\sigma_{EC}(t = 45[\text{us}) = 0.03$ [S/m]. Due to the low power absorption associated with the EC-conductivity, $P_l \gg P_a$ and the EC will die out. At optimum conductivity, the LP attains $\eta \approx 1,600$, by (1.53d) corresponding to $T_g \approx 2000$ [K]. The LP- heat conduction power loss at optimum conductivity by (1.54) equals roughly $P_l(T_g = 2000\,[\text{K}], R \approx 0.75\,[\text{mm}]) \approx 60$ [W]. The total LP- power loss $P_l \approx 100$ [W] is less than or equal to the expected power absorption $P_a = \eta_{RF} \cdot P_{in} \approx 2000$ [W], jus-

tifying the assumption of LP stability near optimum conductivity as well as justifying ignoring plasma power loss with respect to power loss to the cavity.

5.4 Characterization of cylindrical TE-011 cavity

Although the rectangular TE_{102} cavity will likely be successful in sustaining the LP beyond 30 us, its simulated maximum efficiency $\eta_{RF} = 0.8$ ($t = 50$ us in Figure 5.5) can be improved upon with a different cavity design. Since the power loss to the EC has already been mitigated by implementing inductive heating, the efficiency can only be optimized by reducing the power loss to the cavity walls. With respect to the rectangular cavity, the topology of the more symmetric cylindrical counterpart inherently possesses a higher quality factor, mitigating the power loss to the cavity walls.

The ground cylindrical TE_{011} mode is the likely candidate for implementation of inductive heating upon examination of its field equations in (1.28). For this cylindrical cavity with dimensions $(\text{radius}, \text{height}) = (a, h)$ this mode sustains the magnetic field antinode at the center of the cavity $(0, h/2)$, providing a location for inductive heating of the LI-plasma.

Moreover, the ratio of magnetic energy density χ_B is raised, with $\chi_B \approx 10$ for the cylindrical mode $(a, 2a)$, a.o.t. $\chi_B = 2$ for the rectangular mode. By (1.50) in combination with (1.17a), this implies that RF-inefficiency is reduced by a factor $1/5$ (even) if rectangular- and cylindrical cavity possess equal quality factor and volume.

Out of all combinations (a, h) such that the cylindrical cavity is resonant at 2.45 GHz, the corresponding quality factor can be proved to be maximal if cylinder diameter equals height $a \approx h/2$. The equation for the resonance frequency of the cylindrical cavity mode can be found by substitution of λ_g, λ_c (equations (1.28)) into the relations (1.5) to obtain $\lambda_0 = c/f_0$. Under the constraint $\lambda_0 = 122.45$ [mm], the relation $a(h)$ can be substituted into formula (5.3b), with maximum Q at $a = h/2$. Consequently, the distance from cavity-center to cavity-walls is maximal, thus minimizing loss of heat to the walls as well as perturbations on flow by reflection of laser-pulse-shock-waves by the walls, thereby nicely satisfying engineering goals (3.) and (4.) mentioned in the engineering of the rectangular inductive heating setup. The dimensions have already been derived under the constraint of tuning (1.), which leaves only the goal of matching (2.) the cavity to be accomplished.

Cylindrical cavity design

The cylindrical cavity design to be discussed here is not a proper cylinder, but a cylinder with its sharp corners ($r \approx a, z \approx \pm h/2$) rounded by a circular boundary. This shape has been built through simulations, and is visualized in 5.6a. It can be formed by a union of four axisymmetric topological objects, consisting of two toruses and two cylinders. An inner cylinder $(R, h) = (82.2, 90)$ [mm]. Centered at the top and bottom planes of this cylinder are toruses with $(r, a) = (52.8, 29.4)$ [mm]. Concentric with the first cylinder is a more longitudinally shaped cylinder with $(R, h) = (52.8, 149)$ [mm]. The exciting waveguide is chosen to be 90×40 [mm], and transitions into the cylinder with $h = 90$ [mm] at an interface of a circular aperture with radius r through a cross-sectional plane of thickness $\delta = 1$ [mm]. In simulations, the iris radius $r_0 = 11.8$ [mm] causes matching under the premise of a homogeneous Aluminum-wall conductivity $\sigma_{Al} = 10^7$ [S/m], although this cannot be confirmed through conventional theory. The iris's position at the interface-transition of rectangular TE_{10}- and cylindrical TE_{011}-modes requires tailored calculations, and may even require additional implementation of an inductive iris in front of the circular iris [26].

Equivalent circuit for cylindrical cavity

This setup's properties can be approximated by those of a cylindrical cavity with radius a and height h such that $(a, h) = (82.2, 149)$, sustaining a cylindrical TE_{011} mode with field equations given in (1.28). This validity of this approximation can be derived from an examination of the distribution of the square field magnitudes $|H|^2$ and $|E|^2$ corresponding to the TE_{011} mode, which do not carry much energy density at the corners. Therefore this cut has little impact on the general properties of the cavity, and we will be therefore be working with the formulae for the perfect cylinder. From the height of the cavity being $h = 148.8mm$, we find $\lambda_g = 2 \cdot h = 297.6mm$. By (1.10) this yields $Z_{wg} = 916\ \Omega$.

Formulae regarding mode losses - α and Q_0 - are taken from [7, paragraph 2.19], where parameters can be found in equations (1.28), and deliver the propagation constant α and boxed quality factor Q_0 specific to the cylindrical cavity mode.

$$\alpha = \sqrt{\frac{\omega\epsilon_0}{2\sigma}}\frac{1}{a}\left(\frac{\lambda_0}{\lambda_c}\right)^2 \cdot \left[1 - \left(\frac{\lambda_0}{\lambda_c}\right)^2\right]^{-1/2} = 2 \cdot 10^{-3}\ [\mathrm{m}^-1] \tag{5.3a}$$

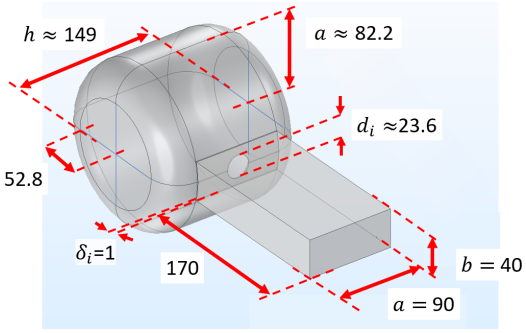

(a) *Geometry of cylindrical cavity in [mm]*

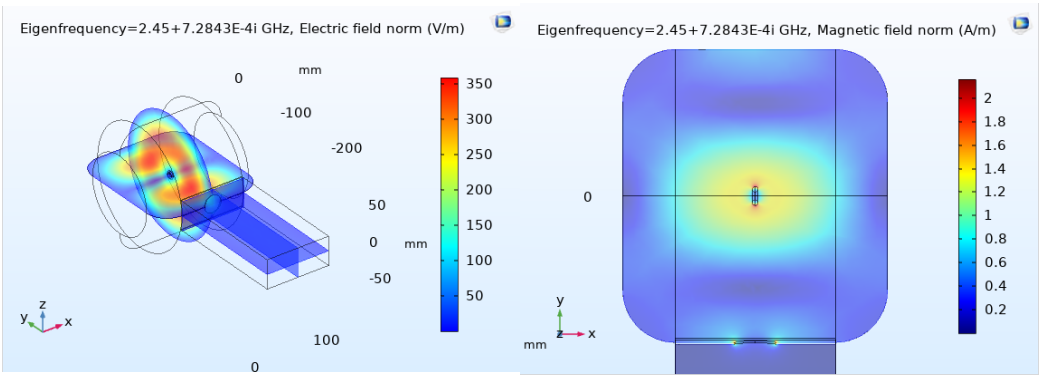

(b) *Free view and the electric field strength.* ***(c)*** *Top view and the magnetic field strength*

Figure 5.6: *Simplified setup of cylindrical TE_{011}-mode cavity.*

$$Q_0 = \pi\sqrt{\frac{2\sigma}{\omega\epsilon_0}}\left[\frac{\lambda_0}{a}\left(\frac{\lambda_0}{\lambda_c}\right)^2 + \frac{4}{n}\left(1-\left(\frac{\lambda_0}{\lambda_c}\right)^2\right)^{3/2}\right]^{-1} = 25,008 \quad (5.3b)$$

Matching of the cylindrical TE-011 cavity

As for matching, we require that the cavity resistance equals the waveguide resistance. The cavity resistance is (like previously) computed over two approaches. Approach (i): determining the value of "boxed" quality factor Q_0 from (5.3b) and the value of the cavity inductance L from (1.11b) and substituting these values in (1.13) to deduce the cavity resistance R. Approach (ii): determining the value of the cavity resistance R directly from the attenuation constant α of the cylindrical TE_{01} waveguide by (5.3a), from the waveguide impedance Z_{wg} by (1.10), the depth d of the cavity along the propagation direction, and lastly the constant κ from integration of the squared magnetic field amplitude $|H|^2$ along the entire waveguide boundary divided by this integration along the boundary par-

allel to $\hat{d}$.

As for the (indirect) boxed cavity approach, the boxed cavity quality factor (5.3b) is $Q_0 \approx 25,000$, which is confirmed through simulation. The equation for the cavity inductance L in (1.11b) was derived through formulae that likewise hold for the cylindrical cavity. Equation (1.11b) may therefore be assumed to apply to the cylindrical cavity and evaluation yields $L \approx 552$ nH. Substitution of these parameters in (1.13) yields $R = 0.34\ \Omega$. Moreover, the capacitance can be found by substitution of L and f_0 in (1.12) yielding $C = 7.64$ fF.

As for the (direct) shorted waveguide approach, the attenuation constant by (5.3a) yields $\alpha = 2e - 3$ [m^{-1}]. The only remaining unknown is the value κ which has been estimated numerically in Python by computing a meshgrid-array of the magnetic field energy density distribution $|B|^2$ in a domain $\theta = 0$, $R \in [0, a]$, $z \in [0, h]$ using (1.28b) and then determining the magnetic field energy distribution by a virtual revolution around the cavity symmetric axis by multiplication of each of the array elements with corresponding R. The constant κ is then evaluated by a ratio of energies at cavity-boundary elements, with the numerator the summation over transverse **and** longitudinal grid-elements $h|_{-}(R = a)$, $R|_{-}(z = 0)$, $R|_{-}(z = h)$, and with the denominator the summation over longitudinal grid-elements $R|_{-}(z = 0)$, $R|_{-}(z = h)$, yielding $\kappa \approx 1.4$. Substitution of all parameters into (1.22e) yields $R = 0.382\ \text{m}\Omega$. The boxed quality factor of the cylindrical cavity is found by substitution of L and R into (1.13) and yields $Q_0 \approx 22,300$.

The two approaches are roughly in accordance over Q and we can thus reliably state that the cavity resistance of the cylindrical cavity is roughly $R_0 = 0.35\ \text{m}\Omega$. Substitution of this cavity resistance in (1.22c) will yield the iris radius for the relation (1.22d) because the same 90 by 40 mm waveguide is used to excite the cavity. Zeroth order ($\psi = 1$) estimate of required iris inductance yields $\mathcal{L} = 0.86$ nH corresponding to $r = 9.73$ [mm]. Evaluating (1.21) yields $\psi(r) = 0.75$, such that $r_0 = 10.7$ [mm]. However, as we have determined from simulations, the actual matching radius should be $r_0 = 11.8$ [mm]. This discrepancy likely arises from the multitude of differences between the conventional interface of the iris for the rectangular TE_{101}-setup on which the theory is accurate and the interface of the rectangular waveguide to the cylindrical TE_{011}-cavity. Firstly, this iris is the transition from rectangular to circular waveguide. Theory has been derived for such a transition in [2, section 5.32], but only applies if both rectangular and cylindrical cavity possess parallel propagation direction,

along the same direction $\hat{z}$. Secondly, thereby, the modes in the cylindrical setup possess orthogonal propagation direction. This requires the development of new theory specific to this scenario. If the reader would try to develop such theory, then they should look for the literature recommended in [4, page 340, references in footnote].

Some properties of the cylindrical cavity are different from that of the rectangular TE_{101}-cavity. Properties of the cylindrical cavity are provided in Table 5.1, where unmentioned properties w.r.t. Table 2.1 are upheld.

B_0	$6 \cdot 10^{-3}$	T		Z_{wg}	916	Ω
E_0	$1.8 \cdot 10^{6}$	V/m		R_0	0.35	Ω
$Q_{empty}^{matched}$	12,500	[1]		L	552.25	nH
V_0	$3 \cdot 10^{-3}$	m^3		C	7.64	fF
$a \times h$	82.2×148.8	mm^2		λ_g	297.6	mm
α	$2 \cdot 10^{-3}$	m^{-1}		$\mathcal{L}$	0.86	nH

Table 5.1: *Properties of the cylindrical TE_{011}-mode 2.45 GHz heating setup.*

Chapter 6

Discussion of results

Before the end of this paper, it is appropriate to come full circle to the ultimate goal of its implementation in CO_2-dissociation. Chapter 1 to 5 addressed the optimization of heating through maximization of RF-efficiency η_{RF}. This was accomplished through the transition from capacitive heating to inductive heating, and through the transition from the rectangular-TE_{101}- and TE_{102}-mode to the cylindrical TE_{011}-mode.

The next goal in the application of the LI-plasma in CO_2 dissociation is the implementation of gas-injection and -extraction in this new cylindrical TE_{011}-mode inductive heating setup, which brings us back to the theory on the overall reactor efficiency η_{tot} in equation (1) of the introduction.

Goals in engineering of CO_2 dissociation reactor

Similar to the engineering of the inductive heating setups, goals for the implementation of CO_2 dissociation set constraints by which to pursue engineering of the reactor setup, aiming for effective and efficient conversion into the dissociation reaction products. The reactor is like a black box, where input-parameters RF-input power P_{in} and CO_2-gas injection flow rate $\dot{V}$ result in the output-parameter of conversion rate α. **Effective** dissociation is accomplished if a high flow rate ($\dot{V}$ high) can be applied to the reactor while also delivering a high conversion rate ($\alpha \rightarrow 1$). **Efficient** dissociation is accomplished if the SEI (associated with the input power P_{in}, flow rate $\dot{V}$, and conversion rate α) is raised to the enthalpy ΔH; accomplished through the maximization of RF-efficiency ($\eta_{RF} \lessapprox 1$) and the minimization of the total plasma power loss ($P_l \ll P_{in}$). These goals are summarized as follows:

Version of July 8, 2021– Created July 8, 2021 - 13:14

1. Maximize the conversion rate of the reactor-plasma
   (a) Maintain plasma temperature beyond dissociation temperature
   (b) Ensure that all extracted molecules have passed through the reactor plasma to undergo dissociation
2. Minimize power lost to processes other than dissociation
   (a) Minimize power loss by the reactor-plasma
   (b) Minimize the rate of reverse reactions through quenching
   (c) Minimize the power reflection of the cavity
   (d) Maintaining plasma conductivity at optimum conductivity (thus reducing share of parasitic power absorption)

Although the paper will not address (CO_2) injection- and extraction, knowledge of the plasma's effect on RF-properties are best mentioned to set some expectations in the engineering of a successful reactor setup.

Necessary reactor plasma properties

First and foremost, dissociation can be achieved only if the plasma maintains at least the required dissociation temperature; $T \geq T_{dis}$ by goal 1(a) . The approximate dissociation temperature of CO_2 is about $T_{dis} = \Delta H / \Delta S = 5.5\,[\text{eV}]/1.53\,[\text{meV}] \approx 3600\,[\text{K}]$, the ratio of enthalpy of the primary dissociation reaction over entropy [27]. Goal 2(a) requires minimized plasma recombination-, heat conduction-, and thermal radiation-based power loss P_l, each requiring either minimized plasma temperature T_p or its associated ionization grade; such that preferably $T \leq T_{dis}$. **Constraint I: T $\approx$ 3600 [K] $\sim \gamma \approx$ 2**.

Secondly, assuming the approximate geometry $(r, a) = (3.75, 1.58)$ [mm] for the reactor-plasma yields required plasma conductivity $\sigma_{opt} = 30$ [S/m] by goal 2(d), associated with $\eta \approx 600$ by (1.41b) and $\gamma = 2$. **Constraint II: $\sigma \approx$ 30 [S/m] $\sim \eta \approx$ 600**.

Lastly, goal 2(c) requires the minimization of power reflection, which results from either mismatch or mistuning to the plasma-filled cavity. Assuming the cavity's proper turn-ratio $Z_{wg} : R$ and resonance frequency f_{empty} cannot be adjusted, then constant cavity resistance/resonance-frequency $R_{tot} = R \cdot (1 + P_a(r, a, \sigma)/P_{in})$ (see (1.48b)) resp. $f_{tot} = f_{empty} + \Delta f_p(r, a, \sigma)$ (see Figure 8.3, and (5.2)) need to be maintained, and consequently stable plasma-properties σ, r, a. **Constraint III: $\dot{\sigma} = \dot{r} = \dot{a} = 0$**.

The above constraints do not cover goal 1(b) and goal 2(b), because these involve plasma- and flow-physics. Likewise, the geometric properties (r, a) were chosen for the LI-plasma at $t \approx 45$ [us] $\sim (3.75, 1.58)$ [mm], because very little is known about the relation with flow. Passive flow completely changes the geometric properties in (3.1a)& (3.1b) [18, Figure 5.6 and 5.7], while active flow might influence the geometry for the fulfilment of goals 1&2(b). In order to influence and fixate the geometry, active intervention on the flow may be necessary, which may be accomplished through the creation of a flow vector field that equilibrates the reactor plasma geometry. For example, the vorticity inherent to the (LP-) reactor plasma may lead it to equilibrate for major radius r on the interface of two opposing axisymmetric streamlines.

Convenient reactor plasma properties, and convenient FQ-tube insertion

By goal 2(b), molecules being ejected from the plasma (by thermal velocity) pass through a steep temperature gradient, and undergo "quenching". A steep temperature gradient mitigates the amount of molecules undergoing the reverse reaction $2CO + O_2 \rightarrow 2CO_2$ that molecules can undergo between room- and dissociation temperature. Successful quenching is achieved for a local temperature gradient of at least $\nabla T \cdot \hat{n} = \partial T / \partial \rho \geq 10^6$ [K/s], perpendicular to the plasma's toroidal surface [28]. Supposing a steady state central temperature $T(\rho = 0) = 4000$ [K] (ignoring cross-sectional power absorption dependence over ϕ), toroidal minor radius $a \approx 2$ [mm], (minimal) room-temperature thermal velocity, evaluation indicates that backward-dissociation will likely not occur, and a may possibly be raised.

$$\frac{\partial T}{\partial \rho} \geq \frac{\Delta T}{\Delta \rho} \cdot \frac{\Delta \rho}{\Delta t} = \frac{4000 \text{ [K]}}{2e - 3 \text{ [m]}} \cdot 300 \text{ [m/s]} = 6 \cdot 10^8 \text{ [K/s]} \gg 10^6 \text{ [K/s]}$$

A different combination r, a, σ of the reactor plasma may enhance the conversion rate and power absorption. Most notably, high major radius r combined (supposing constant $a \approx 2$ [mm]) has two main advantage: higher inductive power absorption by (1.48b) (due to the encapsulation of a larger magnetic flux) and lower associated optimum conductivity σ_{opt} consequently yielding higher optimum power absorption because of $P^{(opt)} \propto 1/\sigma^{(opt)}$.

The reactor design might involve the injection and extraction of gas through a FQ-tube used conventionally for microwave heating purposes.

Version of July 8, 2021– Created July 8, 2021 - 13:14

If - for cavity radius a - a high thickness $\delta \lessapprox a/2$ of the tube is chosen occupying the cavity-section $R_{inner} < a/2 < R_{outer}$, the cavity volume can be decreased in similar fashion to the insertion of the FQ-slabs in the TE_{102} setup. Namely, the high dielectric constant then overlaps with the high electric field magnitude at $R \approx a/2$ as per field equations (1.28), allowing for a decreased cavity volume, increased magnetic field energy density, and consequently increased plasma power absorption.

Chapter 7

Conclusions

In conclusion, the employment of inductive heating of the LI-plasma is more effective and more efficient than capacitive heating. High heating efficiency is attained because of more favourable power absorption within the higher conductivity of the LP with respect to EC during the characterized period of 30 to 60 microseconds after the laser-pulse. High effectiveness is attained because of the inductive-heating optimal conductivity possessed by the LP at 50 microseconds into its decay, corresponding to absorption of 70 percent of the unattenuated input power upon central placement within the rectangular TE-102 cavity, axisymmetric with its magnetic field. Examination of the cylindrical TE-011 cavity yielded higher quality factor and higher magnetic field magnitude at the central magnetic field antinode, providing a suitable candidate for future increase of the inductive heating efficiency of the LI-plasma.

The properties of the LI-plasma had been determined both theoretically for homogeneous properties and simulation-wise for non-homogeneous properties, through reproduction of the dynamic quality factor and -frequency shift determined through 2.45 GHz power-reflection measurement data. These methods possessed overall good accordance on the EC-conductivity to be between 0.01 and 0.1 [S/m], but with approximate accordance on the LP-conductivity only between 50 to 60 microseconds after the laser-pulse corresponding to between 1 and 10 [S/m]. Whereas the theoretical model could not implement the non-homogeneous electron density of the LP, simulations in COMSOL^{TM} were able to account for the sine-to-the-fourth dependence, with a subsequent reduction of the decay constant to four microseconds. As a consequence, simulations reproduced experimental data under dynamic LP-conductivity between 1 and $1e4$ [S/m] over 30 [us] period.

The requirement of the LP's electron density non-homogeneity along with the decay constant equal to four microseconds were both inspired by the analysis of CCD-images. The total intensity of the CCD-images likewise decayed $1/e$ about every four microseconds over the post-laser-pulse-period 30 to 60 microseconds, and the cross-sectional intensity distribution of the LP-torus also followed approximately the sine-to-the-fourth dependence within the same time period. By the proportionality of electron density and radiant intensity, the average electron density within the LP was deduced by normalization through the Boltzmann-normalized Saha equation and the initial temperature from initial 42 [mJ] thermal energy from the laser. The EC- and LP-geometry were derived for the former by the identification of luminous areas under RF-heating, while the latter was derived from the absence of luminosity in regions between the luminous EC. This analysis concluded an EC-volume of 50 [mm^3] confined mainly within two rings of central radius ~ 4 [mm] and with square cross-section of side-length 1 [mm] on either side of the LP; the LP-volume was estimated to be a torus with a volume of 180 [mm^3] and with average major radius of 4 [mm] over the relevant time period. The latter geometry was confirmed to reproduce the plasma's ~ 6 [MHz] downward frequency shift in simulations on a torus beyond cutoff at the center of the rectangular TE-101 cavity, as well as CPT-calculations corresponding to the ratio of sample- and cavity volume along with the torus shape-factor.

Lastly, two cavities were engineered to employ inductive heating, with the rectangular TE-102- and cylindrical TE-011 cavities. Theoretical calculations that ensure tuning and matching were confirmed to reproduce the dimensions of the TE-101 cavity, and were then applied to engineering the inductive-heating cavities. As for the TE-102 cavity, additional theory was developed to ensure tuning upon insertion of fused-quartz windows through reduction of the cavity depth, encapsulated in an equation relating the downward frequency shift from reduced depth and the upward frequency shift from insertion of dielectric. Both inductive heating cavities were also built in simulations, and their geometries were refined to ensure tuning and matching.

Acknowledgements

First and foremost, I would like to thank Felix Smits, who has been my trusted supervisor throughout my Bachelor project. He has supported me throughout the writing of this thesis over a period of 14 months, spanning from February 2020 to March 2021, even though the initial deadline for the

thesis was marked at June 2020. The employment of inductive heating and transition from the rectangular- to the cylindrical cavity are attributable to him. Although my (sometimes) slothful and stubborn approach has no doubt stretched his patience, Felix has remained helpful throughout the development of my thesis. I attribute the success of this thesis to him and I hope it will serve both him and other members of the research group as a reliable enchiridion during the rest of the research project.

I would like to express my gratitude to Dirk Bouwmeester for checking in on my progress every two weeks during the (unfortunately arduous) beginning of this project. Although his focus has understandably shifted to other occupations, this paper and subsequent experimental verification will hopefully prove his time investment to have been worthwhile.

I hereby thank Léon van Velzen for his company in the office during our simultaneous projects and for his input on many of the subjects discussed on the Tuesday meetings with our supervisor, Felix.

As for the cooperation with other members of Leiden university, I thank the entire Quantum Matter and Optics group for all the interesting seminars and for the amicable atmosphere at the 9th floor of Huygens; and I want to thank Martin van Exter in particular for extending his support. I thank the members of the *Fijn Mechanische Dienst* for their correspondence on the engineering of the next TE_{102} experimental heating setup; although the delivery of its dimensions had been long due, this will hopefully makes up for in good faith that the cavity will be both matched and tuned.

Lastly, I would like to express my gratitude to all individuals who have unknowingly contributed to this thesis. The measurements by Tim Kortekaas [5] and Daan van Seeters [12] have been a cornerstone of this thesis; the characterization of the LI-plasma is only as accurate as the measurements on which it is based. I am also grateful for the rapid and helpful reactions by the Comsol Support Group. I thank all the giants of microwave theory on whose shoulders I have been able to stand: Collin [4], Markuvitz [2], and Montgomery&Purcell [7] have constructed accurate theory just after the war that nevertheless remains abstract to this day. Last but not least, I want to thank my parents and my brother, as well as all the people who I have remained in contact with during lockdown in Leiden. Their company has been consoling during dark times.

Bibliography

[1] W. Bongers, *Plasma-driven dissociation of CO2 for fuel synthesis*, Plasma processes and polymers (2016).

[2] N. Marcuvitz, *Waveguide handbook*, IEEE, 1965.

[3] Wikipedia, *Reflection phase change*, `https://en.wikipedia.org/wiki/Reflection_phase_change`.

[4] R. Collin, *Microwave engineering, second edition*, IEEE press, 1992.

[5] T. Kortekaas, *RF heating and characterisation of laser induced plasma*, (2019).

[6] T. Hirano, *Relationship between Q factor and complex resonant frequency: investigations using RLC series circuit*, IEICE Electronics Express (2017).

[7] E. M. Purcell and D. C. Montgomery, *Principles of microwave circuits*, IET, 1987.

[8] Wikipedia, *Relative permittivity*, `https://en.wikipedia.org/wiki/Relative_permittivity`.

[9] Wikipedia, *Fused quartz*, `https://en.wikipedia.org/wiki/Fused_quartz`.

[10] D. N. Peligrad, *Cavity Perturbation by Superconducting Films in Microwave Magnetic and Electric Fields*, Physical Review (1998).

[11] Simon, *Solid State Basics*, Oxford, 2016.

[12] D. van Seeters, *RF Transmission Measurements on a Toroidal Laser-Induced Plasma*, (2019).

[13] M. Leins, *Development and Spectroscopic Investigation of a Microwave Plasma Source for the Decomposition of Waste Gases*, (2010).

[14] J. R. Nagel, *Induced Eddy Currents in Simple Conductive Geometries Due to a Time-Varying Magnetic Field*, IEEE (2017).

[15] Wikipedia, *Q factor*, `https://en.wikipedia.org/wiki/Q_factor`.

[16] Wikipedia, *Magnetic energy*, `https://en.wikipedia.org/wiki/Magnetic_energy`.

[17] H. Young and R. Freedman, *University Physics, 14th ed*, Pearson, 2016.

[18] L. van Velzen, *Flow Confinement of a Laser Induced Atmospheric Helium Plasma*, (2020).

[19] V. Kooij, *Laser-generated toroidal helium plasmas*, Leiden University (**in preparation, 2021**).

[20] Wikipedia, *Levenberg-Marquardt algorithm*, `https://en.wikipedia.org/wiki/Levenberg%E2%80%93Marquardt_algorithm`.

[21] S. Zwaan, *Plasma rings in laser-induced plasma*, Leiden University (2016).

[22] S. Ma, *Relations between light emission and electron density and temperature fluctuations in a helium plasma*, Physics of Plasmas (2011).

[23] V. Gonzalez-Fernandez, *Spatially resolved determination of the electronic density and temperature by a visible spectro-tomography diagnostic in a linear magnetized plasma*, Scientific Reports (2020).

[24] N. Scheinowitz, *On the Thermodynamics of Laser-Induced Toroidal Helium*, (2018).

[25] Wikipedia, *Inductance*, `https://en.wikipedia.org/wiki/Inductance`.

[26] M. K. Joshi and R. Bhattacharjee, *Design of a rectangular waveguide to cylindrical cavity mode launcher for TE011 mode with maximum quality-factor*, Wiley (2019).

[27] H. S. Kwak, *Disintegration of Carbon Dioxide Molecules in a Microwave Plasma Torch*, Scientific reports (2015).

[28] A. J. Wolf, *Elucidating the role of gas dynamics in the vortex-confined microwave plasma on CO2 dissociation efficiency*, ISPC, 24th International Symposium on Plasma Chemistry (2019).

[29] F. Caspers, *RF engineering basic concepts: S-parameters*, (2012), `https://cds.cern.ch/record/1415639/files/p67.pdf`.

Chapter 8

Appendices

Appendix A: Toroidal coordinate system

This section of the appendix addresses the parametrization of the toroidal coordinate system (ρ, ϕ, θ) by a two-step conversion. First from *Cartesian* coordinates to a more intuitive *cross-sectional* coordinate system (R, h, L). Then from the *cross-sectional* coordinate system to the *toroidal* coordinate-system (ρ, ϕ, θ).

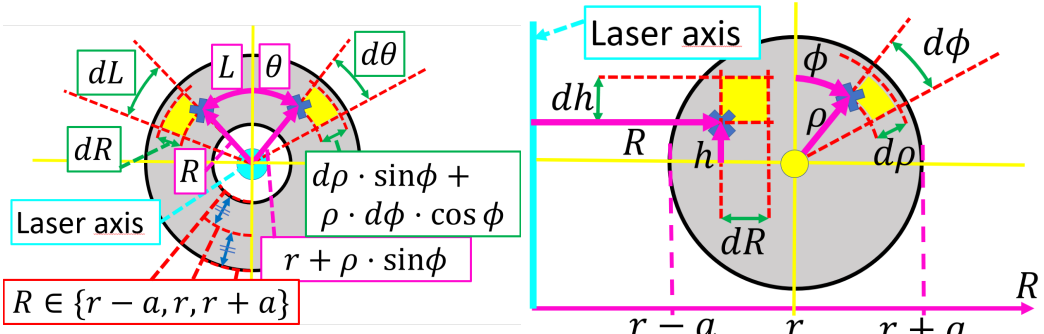

(a) *Top view of torus*

(b) *Cross-sectional view of torus*

Figure 8.1: *Top and cross-sectional view of the torus with definitions of both the cylindrical (left of the vertical) and toroidal coordinate system (right of the vertical).*

Consider the cross-section of the torus. In Cartesian coordinates, the center of the torus is at $(r, 0, 0)$. The radial distance R from the toroidal symmetric axis can reaches from $r - a$ to $r + a$. The height L on the cross-section reaches from $-a$ to a. Lastly, the cross-section is revolved around

the symmetric axis to form a torus, and the revolution length L of a surface-element of the cross-section is dependent on the axisymmetric distance R and the revolution angle θ by $L = \theta \cdot R$ with L ranging from $0 \cdot R$ to $2\pi \cdot R$. The next step is to rewrite the three parameters in terms of a cross-sectional radius from the center ρ ranging from 0 to a, and a cross-sectional angle ϕ ranging from 0 to $2 \cdot \pi$. Doing so, we can define the following coordinates:

$$R = r + \rho \cdot \cos\phi \tag{8.1a}$$

$$h = \rho \cdot \sin\phi \tag{8.1b}$$

$$L = \theta R \tag{8.1c}$$

By converting an integral from the more intuitive cross-sectional coordinate system to the toroidal coordinate system, we can use the Jacobian theorem on integrals:

$$\int_V f(x,y)dx \cdot dy = \int_{V'} f(x(\alpha,\beta), y(\alpha,\beta)) \cdot J(\alpha,\beta) \cdot d\alpha \cdot d\beta \tag{8.2}$$

Where the Jacobian is the determinant of a matrix of derivatives:

$$J(\rho,\phi,\theta) = \begin{bmatrix} \frac{\partial R}{\partial \rho} & \frac{\partial R}{\partial \phi} & \frac{\partial R}{\partial \theta} \\ \frac{\partial h}{\partial \rho} & \frac{\partial h}{\partial \phi} & \frac{\partial h}{\partial \theta} \\ \frac{\partial L}{\partial \rho} & \frac{\partial L}{\partial \phi} & \frac{\partial L}{\partial \theta} \end{bmatrix} = \begin{bmatrix} \cos\phi & -\rho\sin\phi & 0 \\ \sin\phi & \rho\cos\rho & 0 \\ \theta\cos\phi & -\theta\rho\sin\phi & r + \rho\cdot\cos\phi \end{bmatrix} = \rho r + \rho^2 \cdot \cos\phi$$

We can now implement this Jacobian in the integral theorem of (8.2) to find the volume of a torus with major/minor radius r/a:

$$V = \int_R \int_h \int_L dR \cdot dh \cdot dL = \int_{\theta=0}^{2\pi} \int_{\phi=0}^{2\pi} \int_{\rho=0}^{a} \rho r + \rho^2 \cos\phi d\rho \cdot d\phi \cdot d\theta = 2\pi^2 r a^2$$

We can also calculate the normalization factor required to maintain a constant amount of electrons for a homogeneous distribution $\eta(\rho,\phi,\theta) = 1$ of electron density and a non-homogeneous $\eta(\rho,\phi,\theta) = 1 \cdot \sin^4(\frac{\rho\pi}{a})$ distribution of electron density:

$$N = \int_{\theta=0}^{2\pi} \int_{\phi=0}^{2\pi} \int_{\rho=0}^{a} \sin^4(\frac{\rho\pi}{a}) \cdot [\rho r + \rho^2 \cos\phi] d\rho d\phi d\theta = r \cdot a \cdot \frac{3}{4} \cdot \pi^2$$

We thus require a normalization factor:

$$\frac{\iiint_V \sin^4(\frac{\rho\pi}{a}) d\tau}{\iiint_V 1 d\tau} = \frac{r \cdot a \cdot \frac{3}{4} \cdot \pi^2}{2\pi^2 r a^2} = \frac{3}{8} \approx (2.5)^{-1}$$

Version of July 8, 2021– Created July 8, 2021 - 13:14

Appendix B: Transmission and reflection of two consecutive dielectric slabs

As before mentioned, the dielectric slabs influence the electric field due to their high permittivity. What is not studied yet, however, is the possible effect that the perturbed distribution of the electric field has on the tunability of the cavity, and possibly on the matching of the cavity. The reason for this is that the combination of the two dielectric slabs may be regarded as a lumped element transformer with some power transmission coefficient $0 < T < 1$ and a power reflection coefficient $R = 1 - T$. The reason for this is the fact that the high ϵ' of a single slab may be converted to a real refraction index $n'\sqrt{\epsilon'} \approx 2$ by [13]. A signal travelling across a boundary to higher refractive index is partially reflected; not only does reflection occur at the front-most plane of both slabs, field reflected at the front-most plane of the second slab is incident at the back-most plane of the first slab, creating interference of the two signals.

The field in between the two slabs is thus a superposition of the net signal transmitted by the first slab and of the net signal reflected by the second slab. Depending on the phase and magnitude of the net signal, destructive or constructive interference may occur in between the two slabs some center-distance w apart. Additionally, a power reflection coefficient $R > 0$ would lead to a decrease in the tunability $\frac{\partial f_0}{\partial d}$ of the cavity, because of the reduced E-field energy density at the short. Simulations on the slabs are made without such a short, but will nevertheless indicate whether tunability is possible at all: if $R = 1$ then the insertion of a short would not make a difference.

A system with power- transmission- and reflection coefficient corresponds to the lumped element of the transformer, with scattering matrix $[S](m)$ in (8.3) from [29, Figure A.2.6]. Phase shift corresponding to the signal in between the two slabs can be represented by the scattering matrix $[S](\theta)$ from [29, Figure B.3.c].

$$[S](m) = \frac{1}{m^2+1}\begin{bmatrix} m^2-1 & 2m \\ 2m & 1-m^2 \end{bmatrix}, \; [S](\theta) = \begin{bmatrix} 0 & \exp i\theta \\ \exp i\theta & 0 \end{bmatrix} \tag{8.3}$$

A sequence of multiple scattering matrices can be represented by a single scattering matrix, but can only be computed after conversion to a wave-amplitude transmission matrix $[T]$, with the conversion relation $[T]([S])$ in (8.4). The total wave amplitude transmission matrix of a sequence of wave amplitude transmission matrices equals their matrix-product.

Version of July 8, 2021– Created July 8, 2021 - 13:14

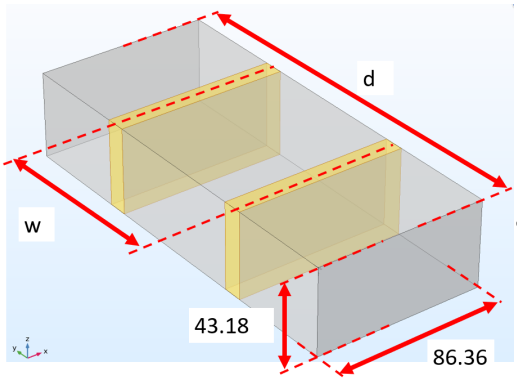

(a) *Simulation model of window setup in WR-340 waveguide, distances in [mm]. The yellow domains are assigned FQ-material with $\epsilon'_r = 3.78$ and the grey domains are assigned free space-material with $\epsilon'_r = 1$. In reflection- and transmission simulations, the boundary conditions encapsulating the object are IBC with $\sigma_{Al} = 10^7$ [S/m] parallel to $\hat{z}$, and input- (1) and output-port (2) at the front and back of the waveguide perpendicular to $\hat{z}$. In cavity tuning simulations, both ports are substituted with IBC, with variable full-model-depth d along $\hat{z}$.*

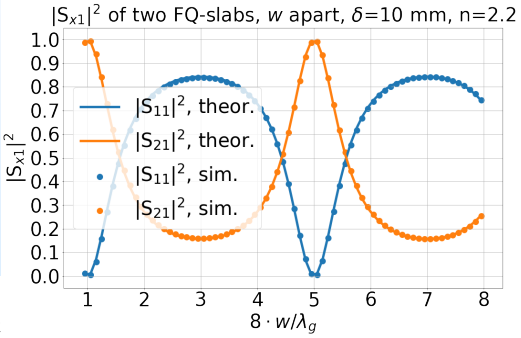

(b) *Comparison of theoretical and simulated total reflection- $R = |S_{11}|^2$ and transmission-coefficient $T = |S_{21}|^2$. Theoretical functions are given by equations (8.6a) and (8.6b). Simulation data are extracted from the system depicted in Figure 8.2a. The turn ratio giving the best accordance of theory with data is $m = 2.2$.*

Figure 8.2

Afterwards, the inverse relation to (8.4) can be used to derive the total scattering matrix $[S]_{tot}$ (8.5) of the system, for two consecutive transformers with equal turn ratio m, an angular phase distance $\theta = \frac{w}{\lambda_g}$ apart.

$$[T] = \frac{1}{S_{12}} \begin{bmatrix} 1 & -S_{22} \\ S_{11} & S_{12}^2 - S_{11}S_{22} \end{bmatrix} \tag{8.4}$$

$$[S]_{tot} = \frac{1}{\gamma} \begin{bmatrix} \gamma - 2(\cos\theta - im^2 \sin\theta) & 2m^2 \\ 2m^2 & -\gamma + 2(\cos\theta - in^2 \sin\theta) \end{bmatrix} \tag{8.5}$$

, where $\gamma = (1 + 2m^4)\cos\theta - i(2m^2)\sin\theta$

We thus come to a system of equations:

$$S_{11}(m,\theta) = \frac{1}{\gamma(m,\theta)} \cdot \Big(\gamma(m,\theta) - 2 \cdot (\cos\theta - im^2 \sin\theta)\Big) \tag{8.6a}$$

$$S_{21}(m,\theta) = \frac{2 \cdot m^2}{\gamma(m,\theta)}, \; \theta(w) = \frac{2\pi w}{\lambda_g} + \frac{\pi}{4} \tag{8.6b}$$

The value of the turn ratio $m = 2.2$ for which data optimally correspond with simulations can be derived theoretically by solving the Fresnel equation $S_{11} = \frac{n_1 \cdot \cos\theta_1 - n_2 \cdot \cos\theta_2}{n_1 \cdot \cos\theta_1 + n_2 \cdot \cos\theta_2}$ for the reflection of the E-field parallel with the Air-FQ interface with $n(\epsilon_r') \approx 2$. The angle of incidence on the FQ-slab is $\theta_1 = \arccos(\frac{\lambda_0}{\lambda_g}$, and the angle of refraction within the FQ-slab is $\theta_2 = \arcsin(\frac{n_2}{n_1}\sin\theta_1)$ by Lenz's law. However, the author's calculations did not provide accordance. Moreover, as visible in (8.6b), the angle θ associated with a distance w elapsed by the travelling-wave needs to be raised by a phase-offset $\pi/4$ in order to provide accordance with the simulation data. The likely cause of this is the phase variability ϕ of the travelling wave upon incidence with the slab. For each phase $\phi \in [0, 2\pi]$, the scattering matrix response is different, with plausibly the average effect corresponding to the $\pi/4$ phase shift, meaning $< [S]_{tot}(m, \theta) >_\phi = [S]_{tot}(m, \theta + \pi/4)$.

Regardless, we should draw the conclusion that the interference-effects of the slabs can be ignored in order of magnitude. Whatever value of w is chosen for the setup, the transmitted power to the short end of the waveguide is at least 20 percent, such that the cavity will remain tunable, although to a lesser degree.

Appendix C: Frequency shift from conductive torus under inductive heating

In the case of a torus placed in the electric field maximum, axisymmetric with the direction, the frequency shift caused by the plasma is constant for constant volume. This was derived theoretically from CPT on conductive samples, and calibrated with a shape factor $\frac{1}{x}$. However, this constant frequency shift over constant volume is not the case for a torus in the magnetic field maximum, axisymmetric with the magnetic field direction. For this reason, simulations are made on different major radii and some set of volumes of the torus in order to deduce what the resonant frequency shift is as a function of the torus geometry $\Delta f(r, a)$. The results for a standard TE_{102}-cavity with length $2 \cdot \lambda_g/2$, is shown in 8.3.*

Under capacitive heating, we saw that the frequency shift Δf from insertion of a sample at the electric field maximum is constant in case of

*This does not take into account the reduced cavity volume V_0 in the case of the presence of FQ-slabs. The predicted frequency shift from B-field placement is given by (1.33a) for the substitution $\chi_E \to -\chi_B$. Because $\Delta f \propto 1/V_0$, the data in 8.3 does not accurately reflect the frequency shift in the case of the new setup in Figure 5.4.

Version of July 8, 2021– Created July 8, 2021 - 13:14

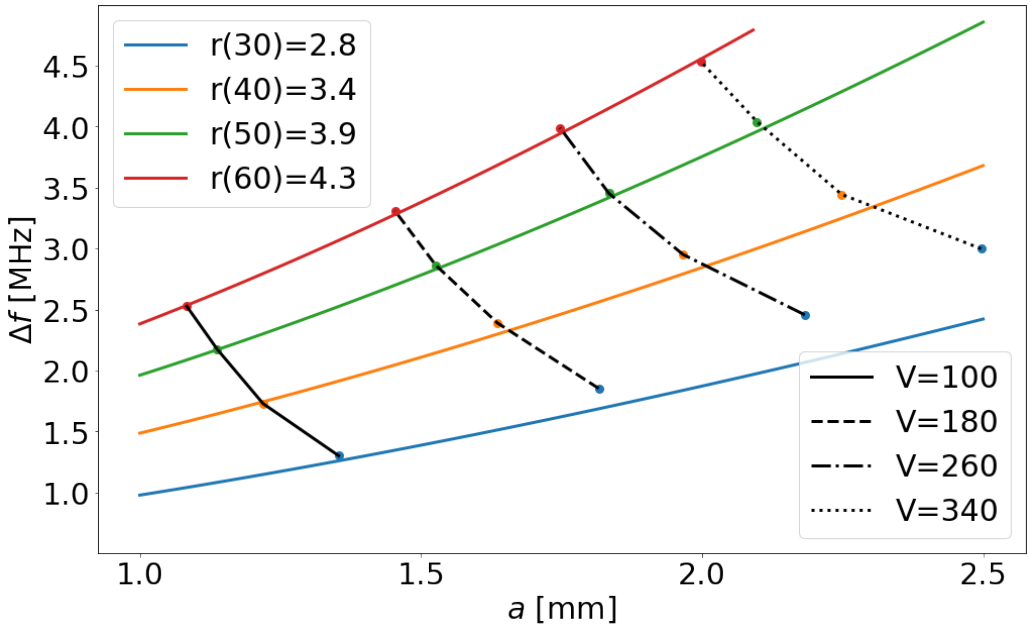

Figure 8.3: *Cavity resonant frequency shift Δf [MHz] containing a torus at its center, with $(r,a)(t)$ [mm,mm,μs], $\sigma \to \infty$, and volume V [mm^3]. The simulation model is an iris-matched WR-340 rectangular TE_{102} cavity of depth $d \approx \lambda_g$.*

constant volume V of the sample. Moreover, in that case Δf was independent of the specific geometry (r,a), but was simply multiplied determined by the torus shape factor $x = 1/2$. Because Δf was measured to remain constant, we deduced that the torus must remain at constant volume V. The constant value of Δf because of constant shape factor and constant volume meant that the cavity containing the plasma could be easily tuned over the lifetime of the LP, simply by tuning the cavity to a resonant frequency $f_{res} = f_0 - (\Delta f)_{LP} = f_0 + 5.7$MHz before starting the heating experiment.

However, from figure 8.3, we deduce that Δf is no longer constant for constant V. Moreover, we see that Δf is non-linearly dependent on both r and a. First, we would like to deduce a function that expresses this Δf accurately in terms of (r,a). Different functions have been fitted to the data through trial and error, and the most simple function that accurately followed the data was:

$$\Delta f(r,a)\ [\text{MHz}] \approx 0.064 \cdot r^2 \cdot (a^{\frac{3}{2}} + 1),\ (r,a)\ [\text{mm,mm}] \tag{8.7}$$

One can predict the resonant frequency over time by following the curve $V = 180\text{mm}^3$ for t from 30 us to 60 us, to find $\Delta f(t = 30us) = 1.9$

MHz and $\Delta f(t = 60us) = 3.3$ MHz. If we suppose we can only tune the cavity beforehand, then the cavity can never be tuned over the entire lifetime of the LP. We need to make a concession to tuning at some instances over the LP lifetime, while tuning the system during the time-period where this is most efficient. The LP has optimal conductivity around 45 us, in which case the function can be called to deduce $\Delta f(t = 45us) \approx \Delta f(3.7, 1.57) = 2.6$ MHz to be the frequency shift. This means that in order to tune the cavity with the plasma at 45 us, we need to tune the empty cavity resonant frequency to $f_0 = f_{mag} - 2.6$ [MHz]. This downward tuning will ensure that the power absorbed into the LP over its lifetime is maximized.

Version of July 8, 2021– Created July 8, 2021 - 13:14